

**STRUCTURE OF THE QUEEN CHARLOTTE BASIN AND
UNDERLYING CRUST FROM MODELLING AND INVERSION
OF THREE-DIMENSIONAL SEISMIC REFRACTION DATA**

by

JOHN ANDREW HOLE

B.Sc. (Geology and Physics), Carleton University, 1986

A THESIS SUBMITTED IN PARTIAL FULFILLMENT OF
THE REQUIREMENTS FOR THE DEGREE OF
DOCTOR OF PHILOSOPHY

in

THE FACULTY OF GRADUATE STUDIES
DEPARTMENT OF GEOPHYSICS AND ASTRONOMY

We accept this thesis as conforming

to the required standard

THE UNIVERSITY OF BRITISH COLUMBIA

January 1993

© John Andrew Hole, 1993

In presenting this thesis in partial fulfilment of the requirements for an advanced degree at the University of British Columbia, I agree that the Library shall make it freely available for reference and study. I further agree that permission for extensive copying of this thesis for scholarly purposes may be granted by the head of my department or by his or her representatives. It is understood that copying or publication of this thesis for financial gain shall not be allowed without my written permission.

(Signature)

Department of Geophysics and Astronomy

The University of British Columbia
Vancouver, Canada

Date 17/01/93

ABSTRACT

A combined seismic reflection and refraction survey was carried out in 1988 to investigate the structure and tectonic evolution of the Queen Charlotte (QC) Basin and underlying crust off the northern coast of British Columbia. While the marine multichannel reflection data were being collected, refracted and wide-angle reflected energy from the large airgun array were recorded at surrounding land sites in both inline (2d) and broadside (3d) geometries. The broadside refraction data recorded on the QC Islands provide good 3d coverage beneath western Hecate Strait. In this study, these data are interpreted to determine the 3d structure of the basin and underlying crust.

Modelling procedures are developed to interpret densely sampled 3d seismic travel time data. An inversion algorithm to determine the depth of a refracting interface and a tomographic inversion algorithm to determine velocity structure are described. Travel times for 3d models are computed using a rapid finite difference algorithm that is extended to allow large velocity contrasts, the determination of rays, variable sampling of the model, and the computation of reflection times. The inversion in both algorithms is parameterized in a simple manner that eliminates the need to store or solve large systems of linear equations. Iterative nonlinear procedures allow arbitrarily large 3d anomalous velocities and interface structures to be determined. The advantages in computational speed of the procedures allow dense spatial sampling of the models, providing spatially well-resolved 3d images.

Variations of the first arrival travel times from the broadside refraction data are inverted to determine the 3d basement depth structure of the QC Basin. The thickness of the basin varies rapidly between ~200 m and ~6 km in a complex sequence of 3d fault-bounded

subbasins. The orientation of, and topography across, several major faults and the overall complexity of the subbasins support a distributed strike-slip extension evolutionary model for the basin. The first arrival travel times are then inverted to determine the 3d velocity structure of the upper (<12 km depth) crust beneath western Hecate Strait. The average 1d velocity structure and the significant lateral variations are interpreted in terms of regional geology. Wide angle reflection travel times from the Moho constrain the thickness of the crust to be 29 km beneath the eastern coast of the QC Islands. The Moho is deeper under the QC Islands than under Hecate Strait or QC Sound, suggesting that crustal thinning during Tertiary extension was greatest beneath the surface expression of the QC Basin. In an alternate or additional explanation, compression at the plate margin during the last 4 Ma may have been taken up by thickening or underplating of the continental crust adjacent to the margin beneath the QC Islands.

CONTENTS

ABSTRACT	ii
LIST OF TABLES	viii
LIST OF FIGURES	ix
ACKNOWLEDGEMENTS	xii
1 INTRODUCTION	1
1.1 Background	1
1.2 Geology and Geophysics of the Queen Charlotte Region	3
1.3 The 1988 Queen Charlotte Seismic Survey	7
1.4 Finite Difference Travel Times	10
1.5 Thesis Outline	16
2 MODELLING THE QUEEN CHARLOTTE BASIN ..	18
2.1 Introduction	18
2.2 Interface Inversion	19
2.2.1 Introduction	19
2.2.2 Procedure	20
2.2.2.1 <i>Forward Modelling</i>	21
2.2.2.2 <i>Inversion for an Interface</i>	25
2.2.3 Synthetic Example	28
2.2.4 Discussion	32
2.2.5 Conclusions	34

2.3	Structure of the Queen Charlotte Basin	34
2.3.1	Introduction	34
2.3.2	Data	35
2.3.3	Interpretation Method	35
2.3.4	Results	39
2.3.5	Interpretation and Discussion	44
2.3.5.1	<i>Basement Depth Model</i>	44
2.3.5.2	<i>Tectonic model</i>	54
2.3.6	Conclusions	58
3	MODELLING THE CRUSTAL VELOCITY	
	STRUCTURE	59
3.1	Introduction	59
3.2	Three-Dimensional Travel Time Tomography	59
3.2.1	Introduction	59
3.2.2	Inversion	61
3.2.3	Resolution	66
3.2.4	Implementation	69
3.2.5	Backprojection Tomography	72
3.2.6	Synthetic Examples	74
3.2.7	Discussion	82
3.2.8	Conclusions	87

3.3	Crustal Velocity Model	88
3.3.1	Introduction	88
3.3.2	Data	89
3.3.3	Interpretation Method	90
3.3.4	Results	94
3.3.5	Discussion	97
3.3.6	Conclusions	100
4	MODELLING THE MOHO	102
4.1	Introduction	102
4.2	Finite Difference Reflection Travel Times	102
4.3	Moho Depth	103
4.3.1	Data	104
4.3.2	Interpretation Method	107
4.3.3	Results	107
4.3.4	Discussion	112
4.3.5	Conclusions	115
5	SUMMARY AND CONCLUSIONS	116
5.1	Three-Dimensional Seismology	116
5.1.1	Data Acquisition	116
5.1.2	Interpretation Techniques	119
5.1.2.1	<i>Future Work</i>	120
5.2	The Queen Charlotte Basin and Underlying Crust	122

5.3	Summary	126
6	REFERENCES	127
APPENDIX A	133

LIST OF TABLES

Table 2.1	Inversion and model fit statistics	42
Table 4.1	Moho modelling	110
Table A.1	Line 4 geometry	133
Table A.2	Line 1 geometry	137
Table A.3	Line 5 geometry	139
Table A.4	Line 6 geometry	141
Table A.5	Line 7 geometry	143

LIST OF FIGURES

Figure 1.1	Map of the 1988 Queen Charlotte Basin seismic survey	2
Figure 1.2	Map of the study area, showing the seismic survey and geology	4
Figure 1.3	Map of the study area, showing rays	9
Figure 1.4	Broadside refraction data sections	10
Figure 1.5	Travel time contours and operators	15
Figure 2.1	Map of the study area, showing submodel for synthetic data inversion . . .	23
Figure 2.2	Cross sections through receiver site 15	24
Figure 2.3	Maps of the submodel for synthetic data inversion	29
Figure 2.4	Travel time residuals for synthetic data inversion	32
Figure 2.5	Map of the study area, showing submodels	36
Figure 2.6	One-dimensional velocity profiles	37
Figure 2.7	Maps of the basement depth model	39
Figure 2.8	Travel time residuals	43
Figure 2.9	Map of the basement depth model in the region of Fault 4	45
Figure 2.10	Line 4 multichannel reflection data	47
Figure 2.11	Line 5 multichannel reflection data	49
Figure 2.12	Maps of gravity and magnetic intensity anomaly	51
Figure 2.13	Two-dimensional density models	53
Figure 2.14	Sketches showing dextral strike-slip faulting	56
Figure 3.1	Map of synthetic seismic refraction survey	75

Figure 3.2	Vertical velocity profile through synthetic model	76
Figure 3.3	2d slices through the 3d synthetic velocity model	77
Figure 3.4	First arrival travel times for the low velocity anomaly model	78
Figure 3.5	Tomography results for the low velocity anomaly model	79
Figure 3.6	The rms travel time residuals	80
Figure 3.7	First arrival travel times for the noise model	81
Figure 3.8	Tomography results for the noise model	82
Figure 3.9	First arrival travel times for the low velocity anomaly plus noise model . .	83
Figure 3.10	Tomography results for the low velocity anomaly plus noise model . . .	84
Figure 3.11	Number of rays intersecting each cell	85
Figure 3.12	Resolution kernel	86
Figure 3.13	Broadside refraction data sections after static time shifts	90
Figure 3.14	Selected 2d slices through the 3d velocity model	94
Figure 3.15	Travel time misfits	97
Figure 3.16	Map of magnetic intensity anomaly	101
Figure 4.1	Cross-sections through a 3d sampled travel time field	104
Figure 4.2	Broadside refraction data sections showing Moho reflections	105
Figure 4.3	Map of the study area, showing midpoints for the Moho picks	108
Figure 4.4	One-dimensional plot of the velocity models for Moho modelling	109
Figure 4.5	Travel time misfits for the Moho reflection data	111
Figure A.1	Broadside refraction data sections for shot line 4	133

Figure A.2	Broadside refraction data sections for shot line 1	137
Figure A.3	Broadside refraction data sections for shot line 5	139
Figure A.4	Broadside refraction data sections for shot line 6	141
Figure A.5	Broadside refraction data sections for shot line 7	143

ACKNOWLEDGEMENTS

I would like to sincerely thank Drs. Ron Clowes and Bob Ellis for their supervision and counselling during the course of this study in their capacity as research supervisors. I also wish to recognize the rest of the supervisory committee, Drs. Garry Clarke, and Dick Chase. The faculty, staff, and graduate students (past and present) in the Department of Geophysics and Astronomy have provided a great working and social environment. Thanks to these people, I have really enjoyed my stay at UBC and in Vancouver. Several of these people have aided this research by providing assistance ranging from inspirational discussions to technical advice. Special thanks go to David Aldridge, John Amor, John Cassidy, Sonya Dehler, Brad Isbell, Xingong Li, Yaoguo Li, Henry Lyatsky, Mike Perz, Barry Zelt, and probably one or two others I have unintentionally omitted.

The acquisition of the seismic data was funded by the Frontier Geoscience Program of the Geological Survey of Canada (GSC) and involved the participation of scientists from the GSC, the University of British Columbia, and the University of Victoria. I would like to particularly recognize the principal investigators, Drs. Kristin Rohr (reflection; GSC) and George Spence (refraction; University of Victoria), both for the data acquisition and for subsequent interpretations and discussions. I would also like to thank Dr. John Vidale (U.S. Geological Survey) for providing a copy of his 3d finite difference travel time algorithm. Financial support for this research was provided by Chevron Canada Resources Limited, Energy Mines and Resources Canada / Natural Sciences and Engineering Research Council (NSERC) Research Agreements 031-4-91 and 198-4-92, and NSERC research grant OGP07707 and infrastructure grant INF06958. I have been the recipient of NSERC Postgraduate Scholarships, an I. W. Killam Predoctoral Fellowship and a Science Council of British Columbia GREAT Scholarship.

On a more personal level, I would like to thank my parents, who have supported and encouraged me throughout my entire (24 years!) education. Last but not least, I'll thank Judy, who moved to Vancouver with me, allowed me to do field work during our anniversaries (and almost miss our wedding), and has been a wonderfully patient and supporting wife during my studies.

1 INTRODUCTION

1.1 Background

The Queen Charlotte (QC) Basin lies off the northwest coast of British Columbia and underlies QC Sound, Hecate Strait, and the northeastern QC Islands (Figure 1.1) with up to 6 km of sediments. Although the region and the sediments of the basin have been the target of petroleum exploration in the 1960's and early 1970's [*Shouldice* 1971] and of renewed intense study in recent years [*Woodsworth* 1991; *Lewis et al.* 1991], consensus has not yet been reached on a tectonic model for the formation of the basin. Recently proposed models include distributed strike-slip extension [*Rohr and Dietrich* 1992], oblique or en echelon rifting [*Hyndman and Hamilton* 1993; *Souther and Jessop* 1991], simple extension orthogonal to the plate margin [*Hyndman and Hamilton* 1991, 1993; *Thompson et al.* 1991], and block faulting and vertical tectonics [*Lyatsky* 1991]. Earlier models involved rifting in QC Sound and flexural subsidence in Hecate Strait [*Yorath and Chase* 1981; *Yorath and Hyndman* 1983].

As part of the multidisciplinary Frontier Geoscience Program of the Geological Survey of Canada (GSC), a combined seismic reflection and refraction data set was collected in the summer of 1988 [*Rohr and Dietrich* 1990, 1991; *Spence et al.* 1991, 1992]. The purpose of the survey was to investigate the geological structure and tectonic evolution of the QC Basin and underlying crust. Broadside crustal refraction data were recorded on the QC Islands from the large airgun array used for the multichannel reflection survey. These data provide dense three-dimensional (3d) ray coverage of the crust beneath western Hecate Strait. Analysis of

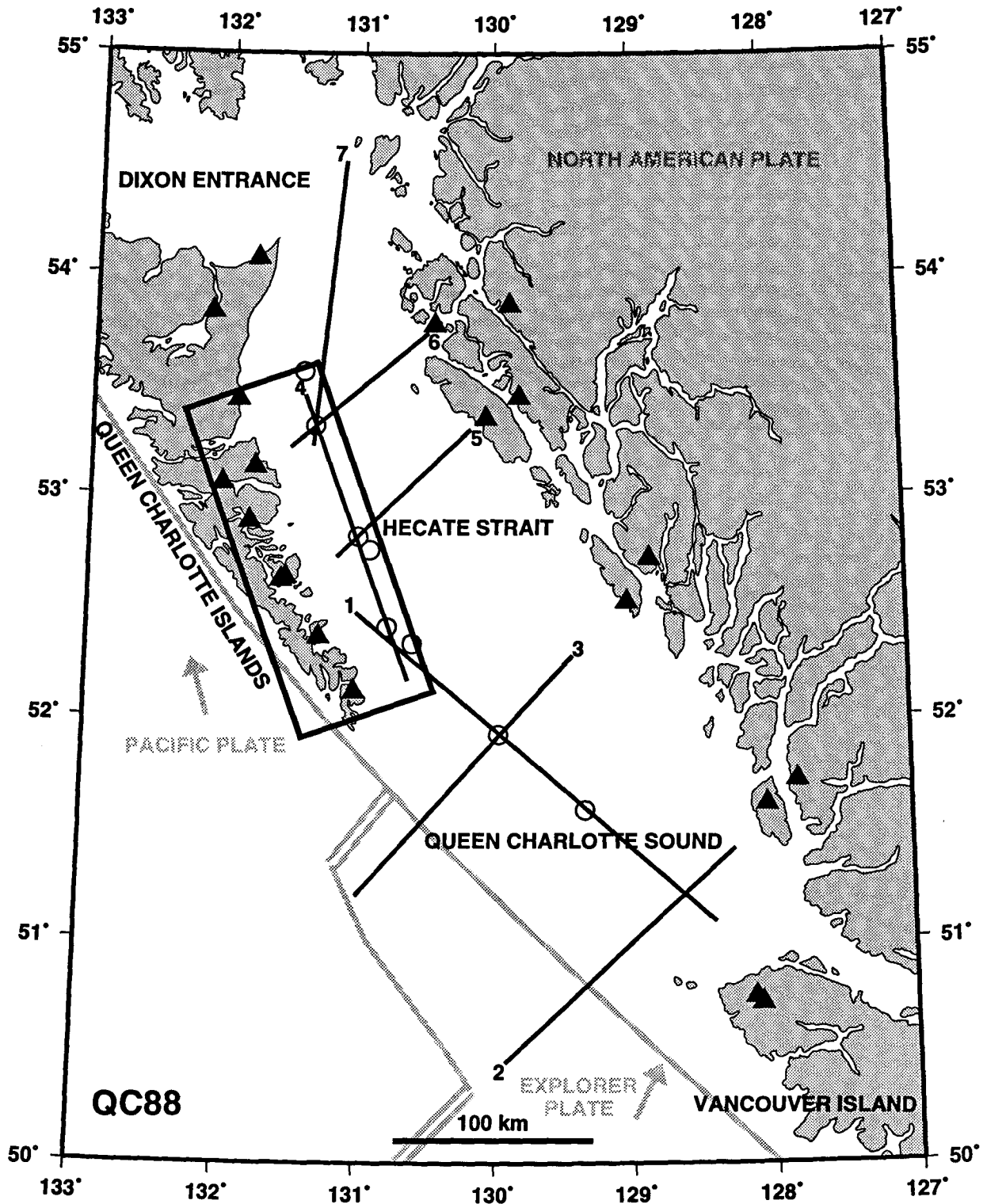


Figure 1.1 Map of the 1988 Queen Charlotte Basin seismic survey in northwestern British Columbia. Multichannel reflection data were recorded along the numbered solid lines. Refraction seismographs were deployed at sites indicated by triangles to simultaneously record the airgun shots. Circles indicate the offshore exploration well sites. The box encloses the study area, expanded in Figure 1.2, used in this study. Current plate boundaries and directions of relative motion with respect to North America are shown as grey lines and arrows, respectively.

the broadside refraction data set and the interpretation of the results in terms of constraints on geological and tectonic models of the region form the basis of this thesis.

This chapter describes the current state of knowledge of the geology and geophysics of the QC region, the seismic survey and data set, a travel time computation algorithm that is used in the analysis, and an outline of the remainder of the thesis.

1.2 Geology and Geophysics of the Queen Charlotte Region

Exploration of the QC Basin for petroleum in the 1960's and early 1970's included a grid of reflection data and eight offshore wells and provided the initial regional descriptions of the basin geology [*Shouldice* 1971]. The basin fill consists primarily of clastic sediments of the Tertiary Skonun Formation [*Sutherland Brown* 1968; *Higgs* 1991]. These sediments are predominantly non-marine in the north, and mixed marine and non-marine in the south. Associated Tertiary volcanism has been mapped on the QC Islands as the Masset Formation (Figure 1.2) [*Hickson* 1991], and fills the deepest part of several of the offshore subbasins [*Shouldice* 1971; *Rohr and Dietrich* 1992]. Contemporaneous and probably associated with the Tertiary volcanism are dyke swarms [*Souther and Jessop* 1991] and the Kano plutonic suite [*Anderson and Reichenbach* 1991].

Cretaceous sediments have been mapped on the central QC Islands (Figure 1.2) [*Sutherland Brown* 1968], but recent stratigraphic analyses [*Haggart* 1991] suggest that only thin non-marine Cretaceous sedimentation is likely north and east of the central QC Islands. The QC Basin in Hecate Strait is underlain by the Wrangellia accreted terrane, which makes up the crust in this region [*Lewis et al.* 1991]. Permian to Jurassic volcanics and sediments of this terrane outcrop on the QC Islands (Figure 1.2) [*Sutherland Brown* 1968; *Lewis et*

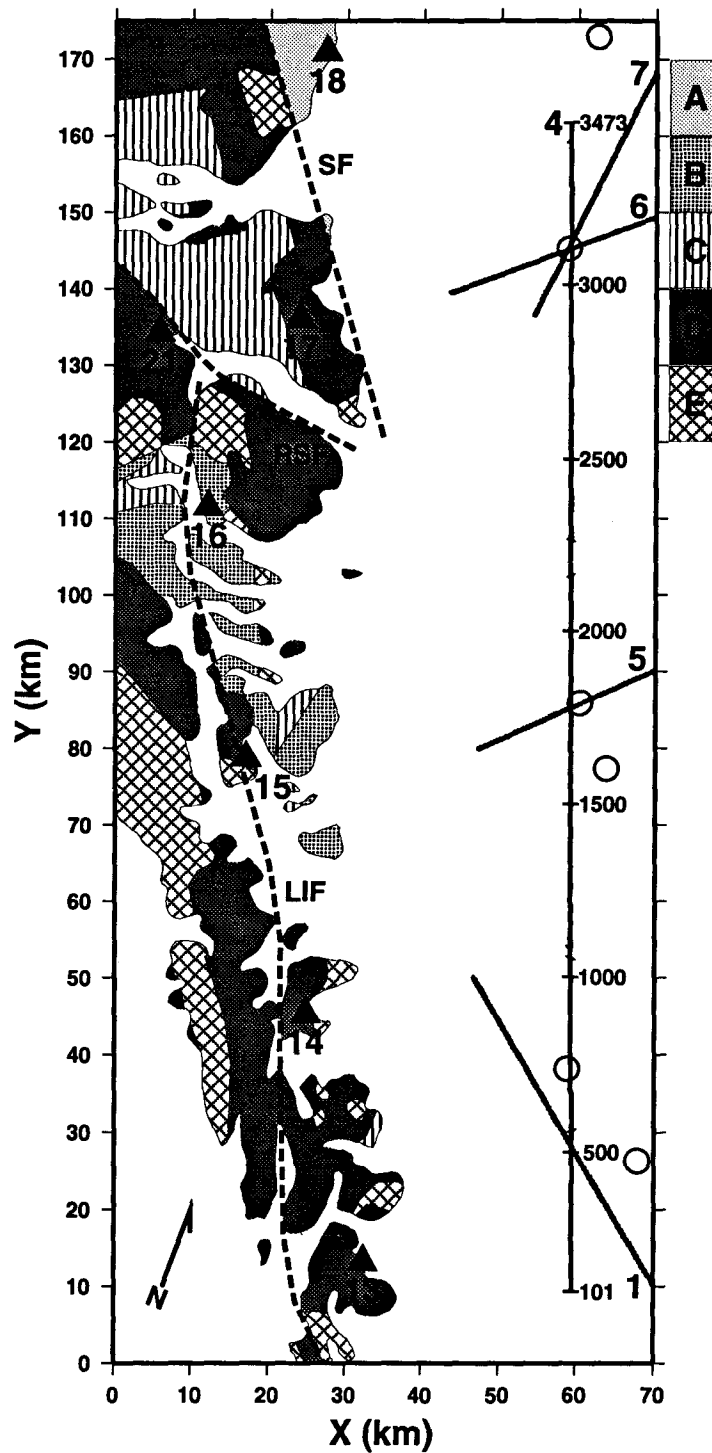


Figure 1.2 Map of the study area, showing the QC Basin seismic survey shot lines and refraction seismograph sites. The symbols used are the same as for Figure 1.1. The Y axis here and in subsequent figures is oriented 20° west of north. Simplified geology is shown on land from Lewis *et al.* [1991]. Geological units: A, Tertiary sediments; B, Tertiary volcanic rocks; C, Cretaceous sediments; D, Jurassic and Triassic volcanic and sedimentary rocks; E, Tertiary and Jurassic intrusive rocks; SF, Sandspit Fault; RSF, Rennell Sound Fault; LIF, Louscoone Inlet Fault. Tertiary QC Basin sediments underlie Hecate Strait. Shotpoint numbers are indicated along line 4.

al. 1991]. The current tectonics of the area are dominated by the plate boundary, the QC Fault, off the west coast of the QC Islands between the North American and Pacific plates (Figure 1.1). The relative motion across the boundary is predominantly dextral strike-slip at a rate of 50 mm/a, with a small component of about 20 mm/a of compression [*Yorath and Hyndman* 1983; *Hyndman and Hamilton* 1993].

Based on the earlier exploration of the basin, *Yorath and Chase* [1981] and *Yorath and Hyndman* [1983] describe a tectonic model for the formation of the QC Basin. This model involves rifting in QC Sound accommodated by major strike-slip displacements cutting the QC Islands and followed by flexural subsidence in Hecate Strait. Recent extensive studies of the basin as part of the Frontier Geoscience Program of the Geological Survey of Canada [*Woodsworth* 1991] have provided evidence against this model. Neither major strike-slip faulting nor flexural tilting were observed on the QC Islands [*Thompson et al.* 1991; *Lewis et al.* 1991], and structures mapped by multichannel reflection studies offshore indicate a complex extensional origin for the entire basin [*Rohr and Dietrich* 1992].

Higgs [1991] analyses the stratigraphy of the Queen Charlotte Basin and describes two stages of basin fill, a period of extension in fault-bound subbasins followed by a period of regional subsidence, generally consistent with the new seismic reflection data [*Rohr and Dietrich* 1992]. Based on the more recent studies, *Thompson et al.* [1991] suggest that the QC Basin formed through simple block fault extension related to the Eocene crustal thinning that affected much of the Canadian Cordillera. *Lyatsky* [1991] suggests that the basin formed by vertical block faulting and reactivation of older structures in response to a younger stress regime. Based on plate tectonic reconstructions applied to the adjacent

plate margin, *Hyndman and Hamilton* [1991, 1993] show that the QC Basin formed during a period of predominantly transcurrent motion along the plate margin with varying amounts of oblique compression and extension. They suggest that the extensional phase of basin formation probably occurred during middle Tertiary and resulted from orthogonal extension in the basin plus transcurrent motion along the margin or alternatively from an echelon rift-transform extension analogous to the Gulf of California. The period of extension was followed by subsidence and minor compression during phases of pure transcurrent motion and then oblique convergence at the plate margin. Using a different model for plate motions and based mainly on dyke orientation and chemistry, *Souther and Jessop* [1991] suggest that the basin formed by an eastwards shift into the basin of the Pacific-Farallon spreading ridge. *Rohr and Dietrich* [1992], who analyse a large data set of deep multichannel reflection data collected as part of the recent studies, propose a basin formation model incorporating distributed strike-slip extension analogous to the California continental borderland. They propose that the basin formed in a complex braided system of fault-bounded subbasins during Miocene transtension followed by thermal subsidence and then minor compression during Pliocene transcurrent and transpressional motions.

Only a few previous seismic refraction studies resolve any information about the offshore Tertiary basin. *Shor* [1962] maps two half-grabens in Dixon Entrance. *Clowes and Gens-Lenartowicz* [1985] interpret data from a sonobuoy refraction experiment in QC Sound and show that the sedimentary thickness varies rapidly. They infer that in some regions low velocity sediments underlie volcanic rocks that were interpreted to form the base of the Tertiary sediments. Similarly in eastern Hecate Strait, *Pike* [1986] interprets low velocities

to represent sediments beneath higher velocity volcanic rocks. He also shows that the basin thickness is greater in western Hecate Strait, and interprets some complex structures at the base of the sediments as an erosional unconformity above Tertiary volcanics. Based on the recent reflection data [*Rohr and Dietrich* 1992], these structures are now known to have been active during basin formation.

Previous crustal seismic experiments in the region provide estimates of crustal thickness but little information about the velocity structure of the crust. *Shor* [1962], *Johnson et al.* [1972] and *Forsyth et al.* [1974] determine Moho depths of about 26 km beneath Dixon Entrance and about 30 km beneath the mainland east of Hecate Strait. *Dehler and Clowes* [1988] and *Mackie et al.* [1989] provide good constraints on the Moho beneath the west coast of the QC Islands at a depth of 21 km and determine, based on much poorer constraints, that the Moho dips steadily to 27 km beneath western Hecate Strait and to 30 km at the eastern margin of Hecate Strait.

1.3 The 1988 Queen Charlotte Seismic Survey

In 1988, as part of the Frontier Geoscience Program, over 1100 km of deep (14 s) marine multichannel reflection data were acquired in Hecate Strait and QC Sound (Figure 1.1) [*Rohr and Dietrich* 1990, 1991]. The data were collected by a contract vessel and initially processed by a contractor under the supervision of the GSC. The purpose of the survey was to investigate the structure and tectonic evolution of the QC Basin and underlying crust. *Rohr and Dietrich* [1992] interpret these data in terms of the evolution of the Tertiary QC Basin, and describe a tectonic model incorporating distributed strike-slip extension. They present a map of the thickness of the QC Basin based on the 1988 reflection data and a grid

of industry reflection data from the 1960's. Although the industry data do not consistently penetrate to the sedimentary basement, their map shows that the geometry of the basin is complex and three-dimensional.

While the contract seismic vessel was collecting these data, refraction seismographs were deployed at surrounding land sites in order to record shots from the airgun array at offsets appropriate for crustal refraction and wide angle reflection data (Figure 1.1). Digital and analogue seismographs were deployed by GSC, University of British Columbia (UBC) and University of Victoria scientists. The digital data were prepared for interpretation at the GSC and the analogue data were digitized and prepared at UBC. *Spence et al.* [1991, 1992] provide details of the data acquisition and archiving. *Yuan et al.* [1992] and *Spence and Asudeh* [1993] interpret the refraction data that were recorded at the ends of reflection lines 1 and 2 and lines 5 and 6, respectively, to obtain traditional two-dimensional (2d) crustal velocity models. *Yuan et al.* [1992] determine that the Moho is at 27 km depth in northern QC Sound and only 23 km in southern QC Sound. *Spence and Asudeh* [1993] obtain Moho depths of 26–28 km in Hecate Strait. These depths for the Moho, shallower than under surrounding regions, coupled with the thickness of the QC Basin sediments imply substantial crustal thinning beneath the basin.

Refraction data were also recorded at offline sites to obtain broadside coverage; in particular shots along lines 1, 4 and 7 were recorded at sites along the QC Islands (Figure 1.1). The 3d coverage is best in western Hecate Strait. This thesis analyses the refraction data within the study area indicated in Figure 1.1 and expanded in Figure 1.2. Figure 1.3 illustrates the ray coverage, assuming no lateral velocity variations, that results from the

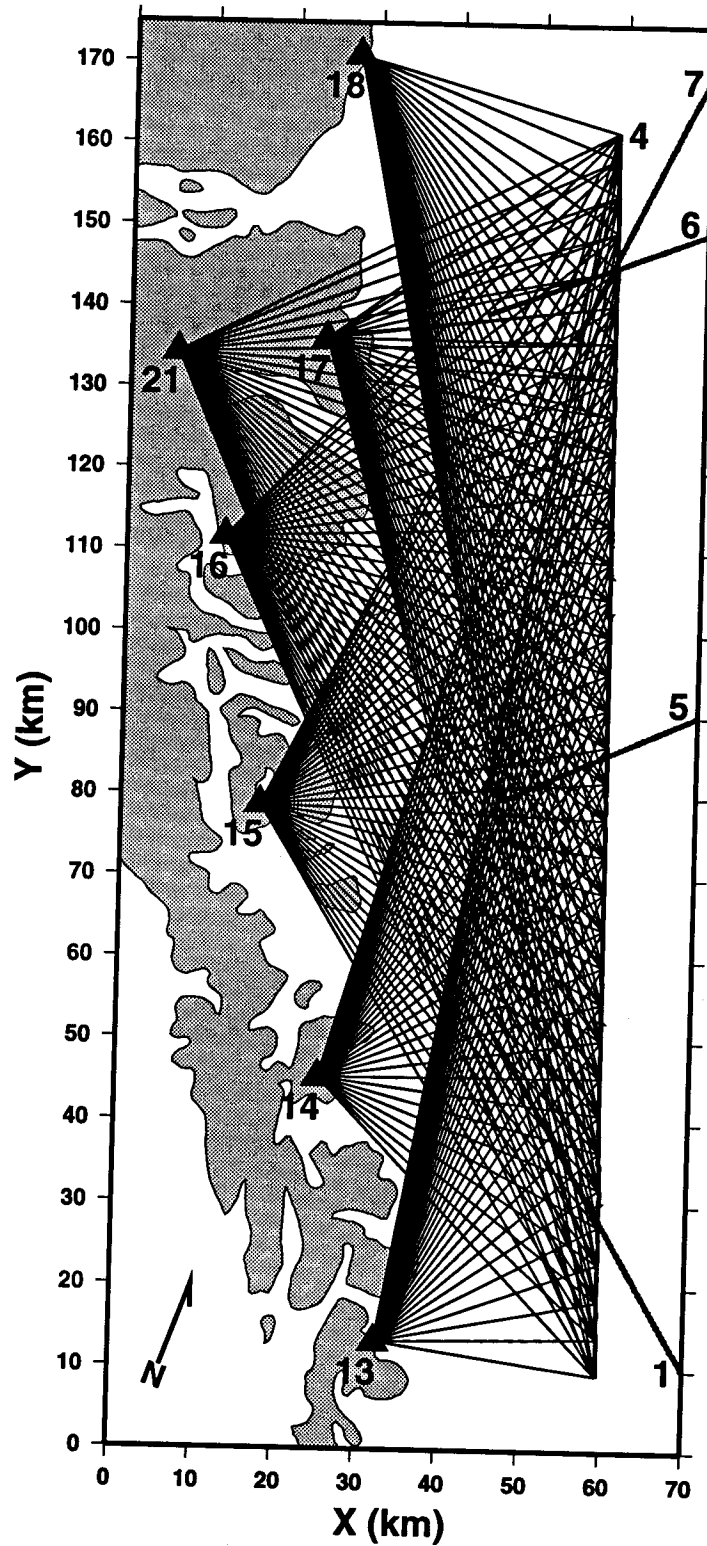


Figure 1.3 Map of the study area, showing surface projections (assuming a 1d velocity model) of rays at a 4500 m shot spacing along line 4 and indicating very dense coverage. The actual shot spacing is 45 m. Every three traces are stacked, so that the data, including shots along the other lines within the study area, are modelled at a shot spacing of 135 m.

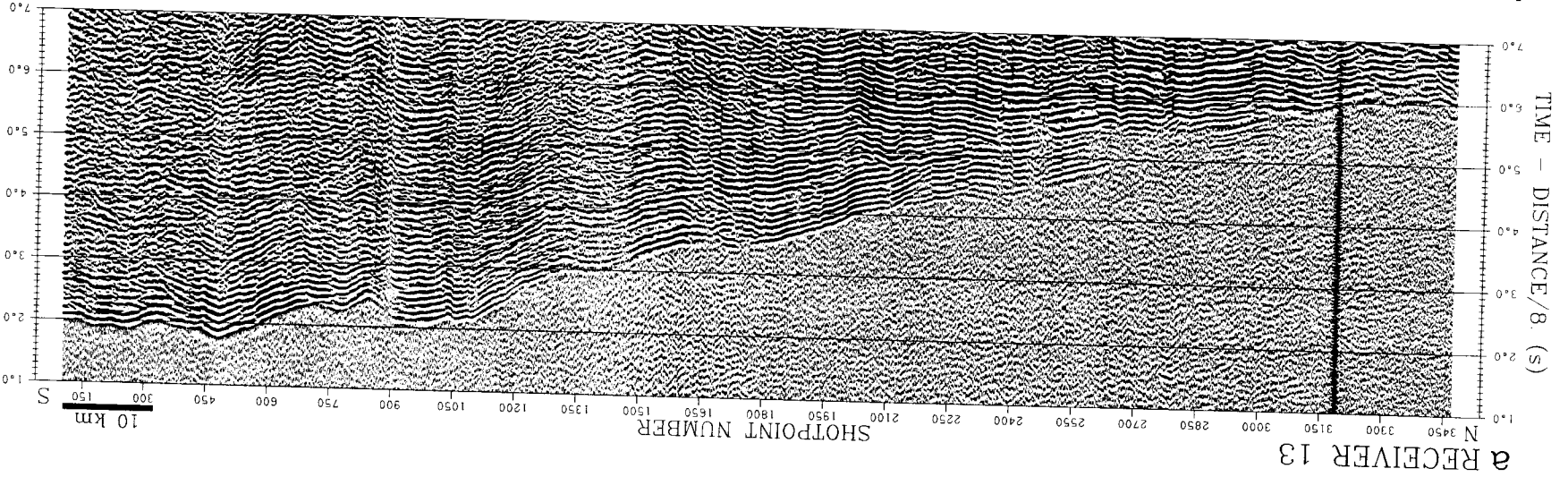
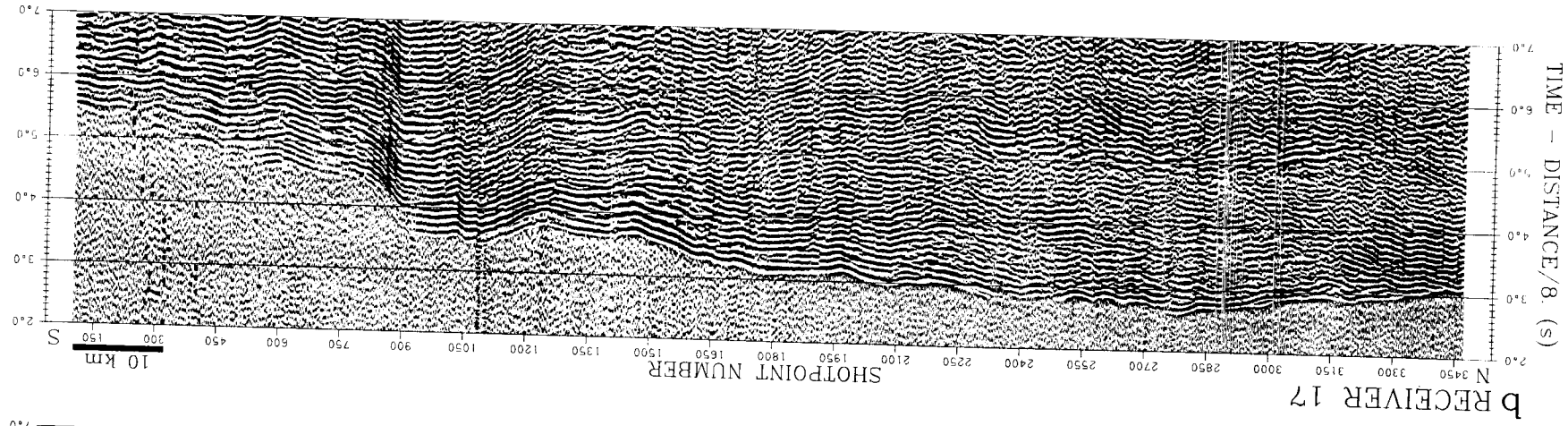
survey geometry. The apparent coverage is excellent in map view, recording energy at seven widely spaced receivers from shots spaced only 45 m apart. Each of the fans of rays shown in Figure 1.3 penetrates to some depth within the crust, so that the overlapping coverage shown in map view is actually seven intersecting sheets of rays in three dimensions.

Figure 1.4 shows the refraction data for shots along line 4 recorded at receiver sites 13 and 17. Clear first arrivals are visible over most of each section and correspond to rays that have turned within the upper (less than 12 km depth) crust. The first arrival times do not form a smooth apparent velocity curve but vary rapidly over short distances. These variations correlate between receiver sections when plotted against shotpoint number and are due to rapid variations in the thickness of the low velocity QC Basin sediments near the shots. Wide angle reflections from the Moho are seen at distances greater than about 70 km (at about 6 s for shotpoints 1800–3200 of Figure 1.4a). Appendix A contains plots of the remainder of the refraction data recorded within the study area.

1.4 Finite Difference Travel Times

In order to model the refraction data, rapid 3d travel time computations are performed using the finite difference algorithm described by *Vidale* [1988, 1990]. This algorithm uses finite difference operators based on the eikonal equation to propagate first arrival travel times through a grid of uniformly sampled velocity nodes. The finite difference operators

Figure 1.4 (next page) Broadside refraction data sections for line 4 recorded at (a) receiver 13 and (b) receiver 17. The traces are plotted against shotpoint number (distance along line 4) using a reducing velocity of 8.0 km/s. For receiver 13, shotpoint 101 is at a shot-receiver offset of 27 km and an azimuth of 258°, and shotpoint 3473 is at 151 km and 170°. For receiver 17, shotpoint 101 is at an offset of 132 km and an azimuth of 325°, and shotpoint 3473 is at 43 km and 214°. Traces are stacked at every third shotpoint (135 m along line 4) using a linear moveout of 8 km/s, bandpass filtered from 5 to 20 Hz, and true amplitude scaled proportional to the shot-receiver offset.



are equivalent to the plane wave approximation at the grid cell level. The source can be placed anywhere within the model. First arrival travel times are properly computed for direct, refracted, diffracted or head waves. The first arrival travel time is found at each grid node within the model, eliminating the need to find the correct ray connecting two points. The algorithm is much faster than 3d two-point ray tracing. The computation time is nearly independent of the velocity model, and is approximately linear in the number of grid points. The speed and flexibility of the algorithm make it ideally suited for the interpretation of large 3d data sets and for the forward modelling step in iterative inversion algorithms.

If needed, rays can be found by tracing backward from the receivers through the computed travel time field [Vidale 1988]. The ray within each grid cell is assumed to be straight and is directed along the average travel time gradient across the cell. This is consistent with the plane wave approximation within the grid cell used by the finite difference travel time algorithm. The travel time field for a single source can be used to trace rays from any number of receivers located anywhere within the model. The process of finding rays is very rapid, and the computation time for each shotpoint depends approximately linearly on the number of receivers and the length of each ray. Taking advantage of the reciprocity of travel times, surveys with a large number of shots and few receivers can be modelled by shooting at the receivers and calculating travel times to the shots.

The disadvantages of the finite difference algorithm are that travel times for secondary arrivals are not computed, the velocity model must be uniformly sampled, and the algorithm is inaccurate in the presence of large sharp velocity contrasts. The first two disadvantages are partially overcome by developments presented later in this thesis. The problems with large

velocity contrasts are noted by several authors [e.g., *Podvin and Lecomte 1991; Qin et al. 1992*], and several alternate operators and propagation schemes are presented. Rather than using these newer schemes, *Vidale's [1990]* algorithm is modified to eliminate the problem.

The problem with large velocity contrasts occurs when the wavefront is critically refracted. Figure 1.5 shows the first arrival wavefronts of a model with critical refraction and the principal 2d and 3d operators of *Vidale [1988, 1990]*. The travel time at the corner of the operator is calculated from the known times by

$$t_0 = t_3 + \sqrt{2h^2s^2 - (t_2 - t_1)^2} \quad (1.1)$$

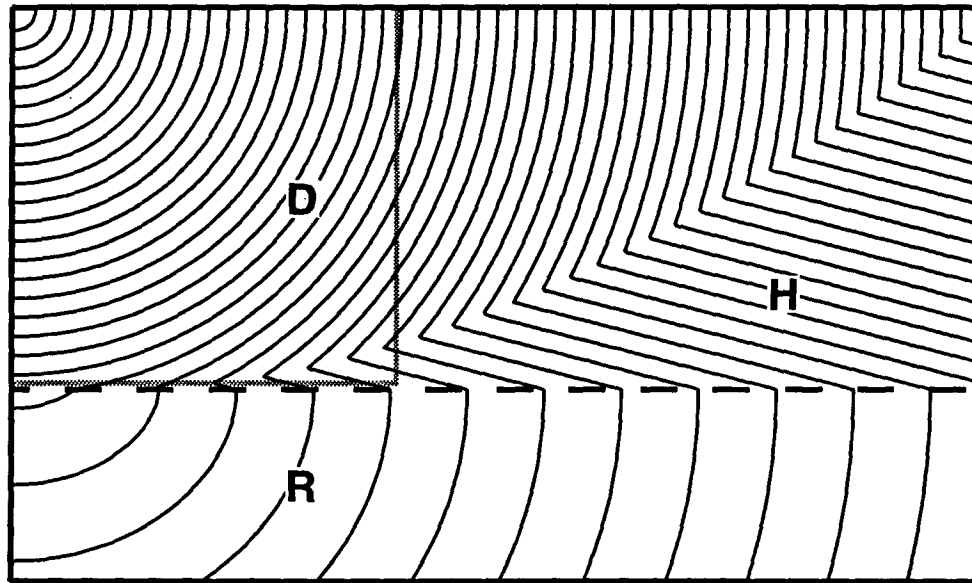
for the 2d operator (Figure 1.5b) [*Vidale 1988*] and

$$t_0 = t_7 + \frac{1}{\sqrt{2}} \sqrt{6h^2s^2 - (t_3 - t_2)^2 - (t_2 - t_1)^2 - (t_1 - t_3)^2 - (t_6 - t_5)^2 - (t_5 - t_4)^2 - (t_4 - t_6)^2} \quad (1.2)$$

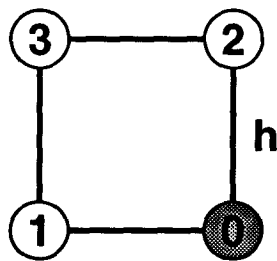
for the 3d operator (Figure 1.5c) [*Vidale 1990*], where t_n is the travel time at the n 'th node in Figure 1.5, h is the grid spacing, and s is the average slowness (inverse velocity) across the grid cell. Consider the 2d case, where the operator in Figure 1.5b is situated across a refracting interface, with nodes 0 and 1 in the higher velocity medium. Beyond the point where critical refraction occurs, t_1 becomes equal to or greater than t_3 , and the correct raypath to node 0 travels along the cell boundary directly from node 1 at the velocity of the faster medium. The operator in equation 1.1 will either fail by producing a negative number under the square root or violate causality by producing a time at node 0 that is less than one of the nodes (node 2) used to calculate it. *Vidale [1988, 1990]* uses an *ad hoc* fix when these error conditions occur. A better solution is to compute the travel time by using a 1d operator that represents a straight ray from node 1 to node 0. This 1d operator represents

a head wave that propagates along the boundary between the two media at the velocity of the faster medium. Similar problems occur in the 3d case when nodes 0, 1, 2, and 4 (Figure 1.5c) are in the high velocity medium beyond the critical point. In this case, head waves along the boundary are computed by applying the 2d operator in Figure 1.5b to nodes 0, 1, 2, and 4 in Figure 1.5c. If this operator also fails, then 1d operators are used directly from nodes 1 and 2 to node 0, taking the lesser travel time.

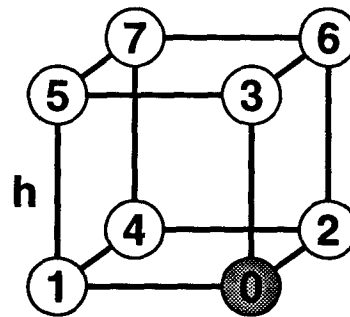
These additional head wave operators will correctly compute the travel time at node 0. The finite difference algorithm computes travel times outwards from the source in expanding squares (2d) or cubes (3d) [Vidale 1988, 1990]. Given the travel times in a cube centred on the source, the times are then systematically computed at the grid points adjacent to each face of the cube, the cube is expanded by one grid cell, and the process is repeated. This means that the travel time at any point on the face of a cube is computed only from times at grid points within the cube. The head wave shown in Figure 1.5a illustrates one example where the first arrival wave actually propagates backwards into the expanding 2d squares. In this example, times in the bottom corner of the grey box, or at node 2 in Figure 1.5b, are calculated using the direct wave, although the critically refracted head wave is the true first arrival. This mistake needs to be corrected whenever head waves are observed travelling parallel to the faces of the expanding square or cube (whenever the head wave operators are used). After travel times have been computed throughout the entire model, the travel time field is used as a starting point and times are computed starting at the appropriate face of the model (in this example, the bottom), and computed perpendicular to that face (upward) one grid cell at a time. Travel times from the new calculations only replace the previously



a



b



c

Figure 1.5 (a) First arrival travel time contours, equivalent to wavefronts, through a simple two layer velocity model. The velocity contrast is 4:1 across the dashed line. The source is in the upper left corner. Regions where the first arrivals are the direct (D), refracted (R) and critically refracted head (H) waves are clearly seen in the contours. The grey square indicates the region of travel times that are computed before the higher velocity medium is encountered. The computation of the next larger square will properly compute the refracted wave, but the head wave will be missed within the lower right corner of the box, affecting later head wave arrivals. Times are recomputed starting at the bottom of the model to find the head wave. (b) Two-dimensional and (c) three-dimensional operators used to compute the travel times at the shaded grid node from the times at neighbouring nodes.

computed times if they are smaller. The true first arrival is guaranteed by Fermat's principle.

These two improvements to Vidale's [1988, 1990] algorithm, the incorporation of head wave operators and the reverse propagation of travel times, completely solve the problems with large velocity contrasts. They incorporate ideas similar to those presented by Podvin

and *Lecomte* [1991], who used a different set of operators. These authors replace the 2d operator in Figure 1.5b with 3 separate operators and the 3d operator (Figure 1.5c) with 16 operators. The smaller number of operators used in the improved version of *Vidale's* algorithm developed in this study make this algorithm computationally faster. Tests using simple velocity models (constant velocity; layer over a half-space with a velocity contrast as large as 10:1; linear velocity gradients as large as 10 km/s/km) have shown that the improved *Vidale's* algorithm is also more accurate than *Podvin and Lecomte's* algorithm. This is probably because the centred finite difference operators of equations 1.1 and 1.2 provide a better planar wavefront approximation when the true wavefronts are non-planar. Tests also show that the improved *Vidale's* algorithm is faster and more accurate than those of *Van Trier and Symes* [1991] (D.F. Aldridge, personal communication, 1991), *Schneider et al.* [1992], and *Qin et al.* [1992].

1.5 Thesis Outline

This research project involves the interpretation of the seismic refraction data recorded within the study area of Figure 1.2. The density and 3d geometry of the data set require the development of new interpretation techniques. Each of the next three chapters presents the development of an interpretation method and its application to the QC data. The derived structural and velocity models are interpreted in terms of the geology and tectonics of the QC Basin and underlying crust.

Chapter 2 presents an inversion procedure to determine the 3d structure on an interface. The algorithm is used to determine the thickness of the QC Basin beneath the shot lines in Hecate Strait. The resulting map of depth to the sedimentary basement is used to constrain

models of the tectonic evolution of the basin.

A 3d travel time tomographic inversion algorithm is presented in Chapter 3. The refraction data are inverted to determine the 3d velocity structure of the upper (<12 km depth) crust beneath western Hecate Strait. The velocity model is interpreted in terms of regional geology.

In Chapter 4, the finite difference travel time algorithm is extended to compute reflection travel times. The depth of the Moho beneath the east coast of the QC Islands is determined, and implications to crustal tectonics are discussed.

Chapter 5 discusses the procedures developed for the interpretation of 3d seismic data and summarizes the structural and seismic velocity models of the QC region and the resulting geological and tectonic interpretations.

2 MODELLING THE QUEEN CHARLOTTE BASIN

2.1 Introduction

Figure 1.4 shows the refraction data for shots along line 4 recorded at receiver sites 13 and 17. Clear first arrivals are visible over most of each section and correspond to rays that have turned within the upper (less than 12 km depth) crust. The first arrival times do not form a smooth apparent velocity curve but vary rapidly over short distances. These variations correlate between receiver sections when plotted against shotpoint number and are due to rapid variations in the thickness of the low velocity QC Basin sediments near the shots. The map of the thickness of the QC Basin based on the reflection data [*Rohr and Dietrich 1992*] indicates that the basin consists of a complex 3d sequence of fault-bounded subbasins.

Refracted arrivals from within the basin or from the basement interface were not recorded as part of the refraction data set due to the large shot-receiver offsets and the position of the receivers outside the basin. To model the subbasement velocity structure, variations in the basin structure near the shots must be either removed from the data or included in the model. For 2d inline refraction data, static corrections for such a low velocity layer at the surface can readily be performed [e.g., *Purdy 1982*]. *Yuan et al. [1992]* perform statics corrections for the inline refraction data based on the basement picked in the reflection sections, and interpret the crustal refraction data based on these corrections. *Spence and Asudeh [1993]* incorporate directly into their 2d refraction models a basin model derived from picks of the reflection data. Such corrections are not so simple for the broadside refraction data because the basin must be known in three dimensions. The 2d basement structure is generally well defined by the 1988 reflection data [*Rohr and Dietrich 1992*], but raypaths from the shots

to the offline receivers sample the basin offline from the reflection sections. The offline interpretation of *Rohr and Dietrich* [1992] based on the earlier industry reflection data is not well resolved due to the poor quality of the industry data and the 3d nature of the structures.

In order to determine the structure of the QC Basin out of the planes of the reflection sections, an interface inversion algorithm is developed and applied to the broadside refraction data. The relative variations on the first arrival travel times are inverted to find the depth of the basement interface. The results provide information about the 3d structure of the basin and will allow the subbasin velocity structure to be modelled in the next chapter.

2.2 Interface Inversion

2.2.1 Introduction

Broadside seismic refraction data were used in the earliest days of petroleum exploration to map lateral velocity variations associated with salt domes and dipping sedimentary horizons [*Weatherby* 1940; *Gardner* 1939]. In the 1950s and 1960s the time-term analysis method was developed, primarily for crustal seismology, to exploit the information obtained from an areal coverage of refraction data [*Scheidegger and Willmore* 1957; *Berry and West* 1966]. Interpretations were limited by the assumptions of a layer with undefined internal structure over a single refracting interface such as the Moho. Subsequent improvements to the method [e.g., *Raitt et al.* 1969; *Bamford* 1976; *Bird* 1982] increased the flexibility by allowing varying refractor velocities and different optimization norms but remained limited to a single refracting interface. A more recent advance has been the development of 3d tomographic techniques applied to earthquake as well as artificial source data [e.g., *Thurber* 1983; *Kanasewich and Chiu* 1985]. These techniques allow for different modelling assumptions,

but limitations in both computer resources and data coverage have restricted crustal-scale models to resolution on the order of a few kilometres.

In recent years, extremely dense seismic refraction data have been recorded using large airgun source arrays [e.g., *NAT Study Group* 1985; *Reid and Keen* 1990], frequently as an addition to a multichannel reflection survey [e.g., *GLIMPCE Seismic Refraction Working Group* 1989; *BABEL Working Group* 1990]. Most of the analysis of such data has concentrated on 2d profiles. Often, however, recording stations broadside to the reflection lines provide data for travel paths that vary both in offset and azimuth. The efficient and effective interpretation of such data is not straightforward.

This section presents the development of a new method of interpretation for broadside seismic refraction data recorded at a number of stations from the source of a multichannel reflection survey. First arrival travel times are inverted to find topography on an interface beneath the shot line. The necessary forward modelling calculations build on the computationally efficient finite difference procedure for the calculation of travel times in 3d media [*Vidale* 1990] described in Section 1.4.

2.2.2 Procedure

As with any inversion technique, there are two basic steps associated with the implementation of the new procedure described here. First, an effective method of carrying out the forward modelling with appropriate parameterization must be available. Second, a computationally efficient and robust inversion procedure must be applied.

2.2.2.1 Forward Modelling

Because a 45 m shot spacing was used in the QC seismic survey, the broadside refraction data provide a much better sampling of the velocity structure near the shot line than near the receivers. In addition, the sedimentary basin beneath the shots consists of a complex sequence of subbasins with steep dips on bounding faults [Rohr and Dietrich 1992]. These characteristics indicate that the velocity model should be parameterized at a finer grid spacing near the shots than throughout the rest of the crustal model. The use of a coarse grid spacing away from the shots provides significant savings in both computation time and memory requirements.

The finite difference algorithm (Section 1.4) has been modified to allow the use of a variable grid spacing. Taking advantage of the reciprocity of travel times, the receiver sites are treated as source locations and times are computed to the shotpoints. Travel times are initially propagated from a receiver position through the 3d velocity model sampled at a coarse grid spacing. A 3d rectangular submodel volume is defined near the shot line where a finer resolution is desired. The coarsely sampled 3d travel time field is inspected to determine the face (or faces) of the submodel that the wave field is entering. Travel times are sampled along these faces and interpolated to a finer grid spacing. Starting with the resampled travel times along these faces, travel times are found within the submodel by using the finite difference algorithm to propagate times from the face with the minimum travel time values. Arrival times at the shotpoints are found by interpolation within the appropriate grid cells. The travel time field is calculated once for each receiver, using the receiver as the source point and computing the times to the shotpoints. Errors introduced by this regridding scheme

are minimal if the travel times at the submodel are sufficiently smooth that the interpolation on the faces is accurate.

For the geometry shown in Figure 2.1, this procedure is illustrated by taking a cross section along fixed Y through the 3d model and submodel at receiver 15 (Figure 2.2). The model is 70 by 175 km in area and extends from -2 to 20 km below sea level. A simple crustal velocity structure (Figure 2.2c), coarsely sampled at a 1 km grid spacing, was determined from a 1d analysis of the broadside refraction data and the in-line refraction interpretations of *Spence et al.* [1991] and *Yuan et al.* [1992]. There are $71 \times 176 \times 23$ nodes at which the velocity and travel time fields are defined. Contouring the travel time field shows the locations of the wavefront at fixed times from a source located at receiver 15 (Figure 2.2a). The submodel region, shown in plan view in Figure 2.1 and cross-sectional view in Figure 2.2a, is 10×40 km in area and extends from 0 to 20 km depth. It consists of $51 \times 201 \times 101$ nodes sampled at 0.2 km. The wave field from a source at receiver site 15 enters the submodel volume only along the western face, so travel times along this face are used as a spatially planar time-varying source to calculate travel times through the submodel (Figure 2.2b). The sedimentary QC Basin is included in the submodel using the velocities in Figure 2.2c, obtained from logs of the six wells shown in Figure 2.1. The wave field in Figure 2.2b is refracted sharply upward by the contrast in velocity across the basement. Remember that the wavefronts in Figure 2.2 do not propagate entirely within the plane of the cross section, as the velocity field is actually 3d.

A ray is found in Figure 2.2b by tracing back from a point along shot line 4 (Section 1.4). Since the velocity model is 3d, the ray is actually slightly out of the plane of the cross

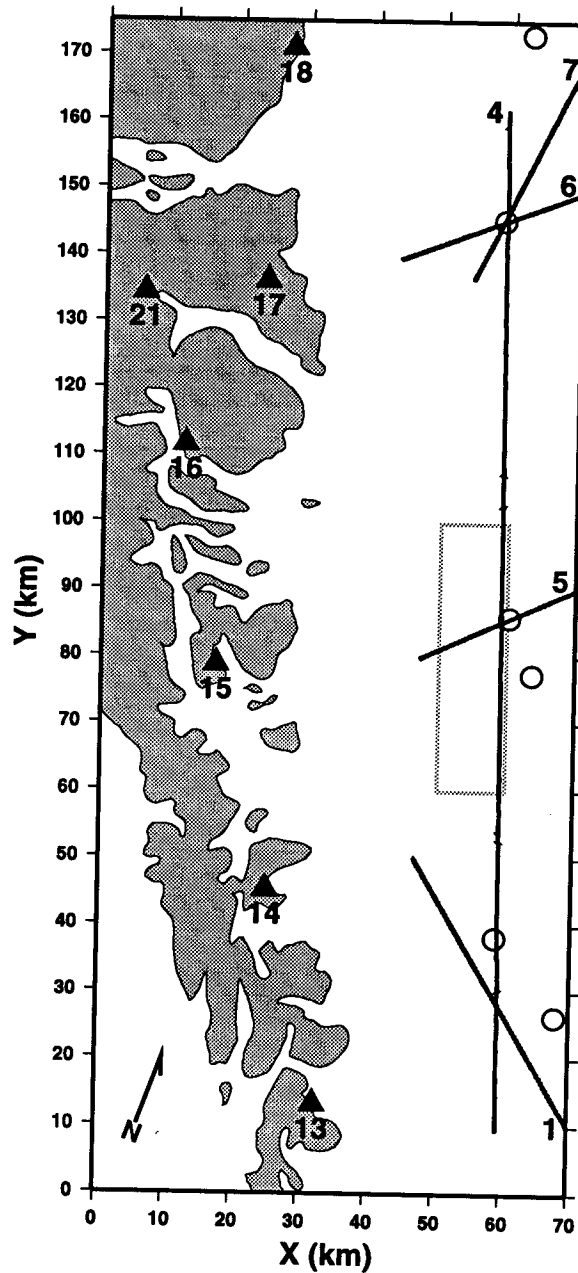


Figure 2.1 Map of the study area, showing the QC Basin seismic survey. Symbols used are the same as for Figure 1.2. The box at the intersection of lines 4 and 5 indicates the submodel area, modelled at a higher spatial resolution, that is used to illustrate the interface inversion procedure. section. The location at which it samples the basement is at 4.3 km depth and 3.4 km west of the shot line and the reflection section. The existence of many such rays provides a means of mapping the structure of the basement out of the plane of the reflection section.

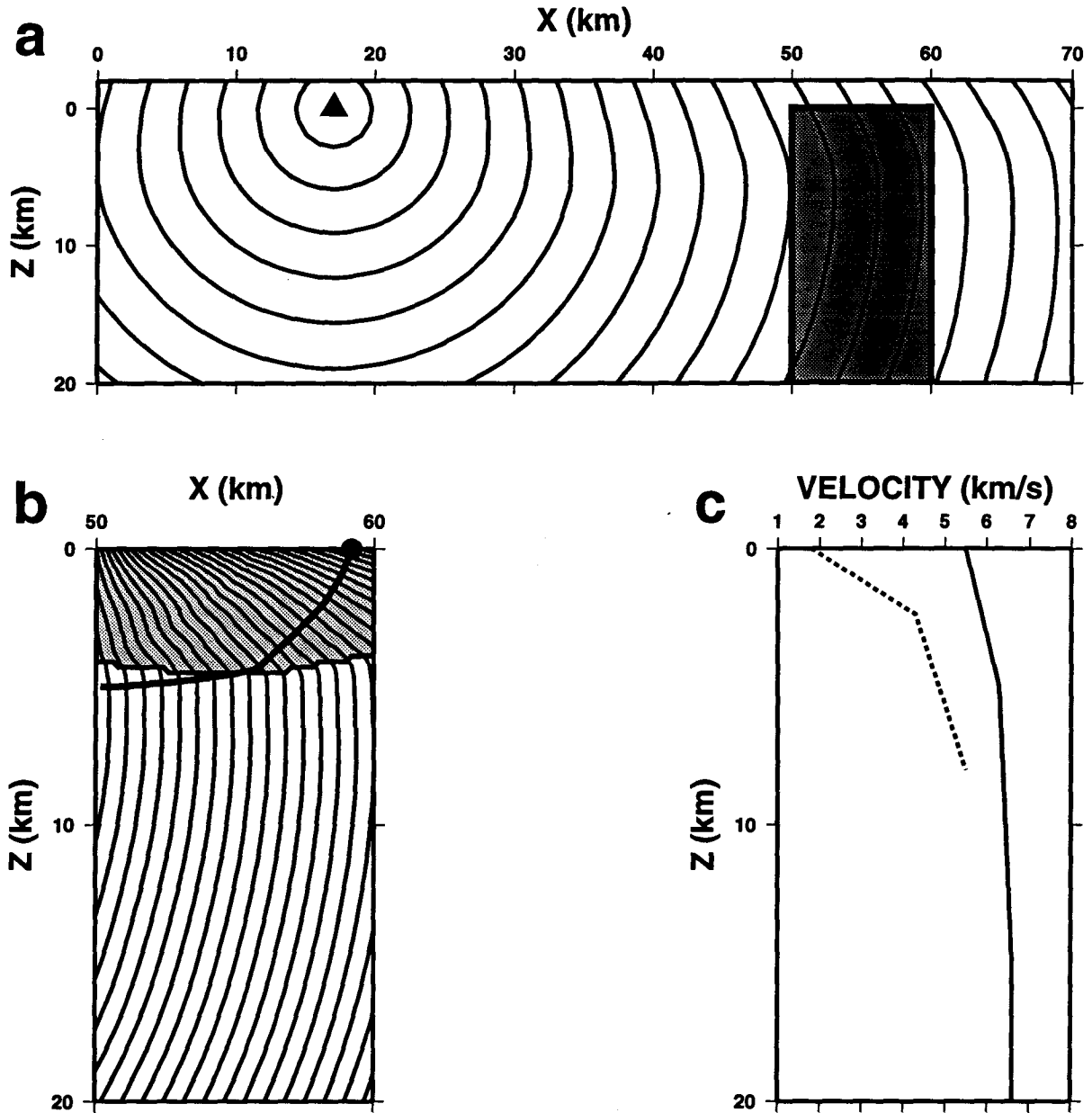


Figure 2.2 X-Z cross sections through receiver site 15 of the 3d velocity model and submodel (Figure 2.1). (a) Travel times calculated at a 1 km grid spacing from receiver 15 (triangle) are contoured at 0.5 s intervals. The location of the submodel volume is indicated by the shaded box. Travel times along the left face are resampled and input as a planar source for the submodel. (b) Times are then calculated at a 0.2 km grid spacing through the submodel and contoured at 0.1 s intervals. A low velocity sedimentary basin (shaded) is included in the submodel above a 3d depth-varying basement interface. A ray is drawn, traced backward from a shotpoint on line 4. The wavefronts and the ray shown in these figures do not propagate entirely within the plane of the cross sections, as the travel times are actually calculated from a 3d velocity model. (c) One-dimensional velocity structure used in the 3d models. The solid line is the crustal velocity profile used in the model (in a) and below the depth-varying basement interface in the submodel (in b). The sedimentary basin velocity profile (dashed line) is used above the basement.

2.2.2.2 Inversion for an Interface

White [1989a] used in-line refraction data to invert for a shallow interface using 2d ray tracing. He derived an estimate for the partial derivative relating the depth of the interface to the travel time, but the published equation contained an error (D.J. White, personal communication, 1990). Using slightly different nomenclature, the corrected equation is given by

$$\frac{\delta t}{\delta z} = \left[\frac{\cos \theta_1}{v_1} - \frac{\cos \theta_2}{v_2} \right] \cos \alpha \quad , \quad (2.1)$$

where δt is the change in travel time, δz is the change in depth of the interface, θ_1 and θ_2 are the angles between the refracted ray and the interface normal measured above and below the interface, respectively, v_1 and v_2 are the velocities immediately above and below the interface, and α is the true local dip of the interface. Although derived for 2d refraction, the formula is valid in three dimensions if α is identified as the true dip of the interface and not the dip within the plane of the ray where θ_1 and θ_2 are measured. Since the variables on the right can be found from the model and the ray, the equation can be used to invert modelled travel time residuals Δt for a change in the depth to basement model Δz using

$$\Delta z = \frac{\Delta t}{\frac{\delta t}{\delta z}} \quad . \quad (2.2)$$

The calculated value of Δz applies only to the point at which the ray intersects the basement. A set of corrections to the basement depth model $\Delta z_k(x,y)$ is thus obtained, where the subscript denotes the correction due to the k 'th measured travel time residual Δt_k .

The basement depth model is discretized, taking on values only at the grid nodes of the 3d velocity model. The ray intersection with the basement and the variables used in equation

(2.1) are found by linear interpolation of the basement depth between grid points. The set of depth correction terms must be gridded in order to apply a correction Δz_{ij} to the sampled basement depth model z_{ij} . A 2d Laplacian surface is chosen to grid the correction terms, fitting the corrections $\Delta z_k(x,y)$ with a function satisfying

$$\nabla^2 [\Delta z(x, y)] = 0 \quad . \quad (2.3)$$

This type of gridding is chosen over other functions, such as splines, for two reasons. A Laplacian surface will extrapolate smoothly toward some average value outside the region sampled by the data, a desired property of the model perturbation. Sharp spikes will be produced at the locations of any data points which are not in general agreement with neighbouring data, but the effect of such points will be restricted to a small region, an effect that can be removed by filtering.

The linearized inversion scheme thus consists of two steps: a data inversion operation involving the simple division in equation (2.2), followed by an interpolation or gridding operation. This scheme may be formalized using standard linearized inversion terminology as follows. The interface depth model has been parameterized using

$$z(x, y) = \sum_{i=1}^{\infty} a_i f_i(x, y) \quad , \quad (2.4)$$

where the basis functions $f_i(x,y)$ have been chosen to be local deltalike functions (whose derivatives are chosen to define the local dip α) and the a_i terms are the depths at the appropriate locations. In order to invert the travel time residuals for interface depth a linear relationship is found between a small model perturbation Δa_i and a data perturbation Δt_k

given by

$$\Delta t_k = \sum_{i=1}^{\infty} \frac{\delta t_k}{\delta a_i} \Delta a_i \quad . \quad (2.5)$$

Because of the choice of basis functions, each Δt_k travel time residual depends only on the model parameter a_i at the location at which the k 'th ray samples the interface. Thus the partial derivative matrix is diagonal, and the k 'th term of equation (2.5) is identical to equation (2.2). The choice of any other set of basis functions would have resulted in a nondiagonal matrix in equation (2.5) and, since this matrix is usually large, its inversion would have been computationally time consuming. The gridding step in our scheme is required to interpolate and smooth the model perturbation so that it can be added to the sampled model used for forward modelling.

The gridded basement depth model correction Δz_{ij} is smoothed using a 3×3 -point moving average filter. The correction is then added to the depth model z_{ij} . Since the 3d velocity model is sampled, the basement is represented as a velocity gradient over one sample interval between two grid points in depth. Any basement depth z_{ij} that lies within a particular sample interval will be represented by the same velocity model. For this reason, all depth values within a particular sample interval are reset to be in the middle of that interval. The basement depth model is then consistent with travel times produced using the model.

The entire process is repeated iteratively. Iterations are stopped when the root-mean-square (rms) travel time residual stops decreasing.

Several factors affect the resolution of the interface depth model. Primarily, the model is dependent upon the assumption that the travel time residuals are entirely due to variations on the depth to the interface. This assumes that the velocities used are accurate and that

the change in velocity can be represented as a discrete interface. Incorrect velocities or a laminated or gradual transition from low to high velocities will cause systematic errors in the interface model.

Assuming a correct velocity model, the factors limiting resolution are the density of data coverage and the errors in the data. If linearity between the travel times and the basement model is assumed, equation (2.2) can be used to relate errors in the travel time data directly to errors in the model perturbations $\Delta z_k(x,y)$. Resolution of the depth value at a grid point z_{ij} depends on the coverage of rays intersecting the interface near the grid point and on the gridding and smoothing operations. If the horizontal sampling interval is chosen to be similar to the shot spacing, there will be approximately one ray for each grid cell and the resolution of z_{ij} prior to smoothing will be similar to that of $\Delta z_k(x,y)$. Horizontal smoothing over many nearby rays will improve the depth resolution but will decrease the horizontal resolution. The sampling interval used in the velocity and basement models should be chosen to be smaller than the resolution expected from the data. This ensures that any features that can be constrained by the data can be properly imaged in the model.

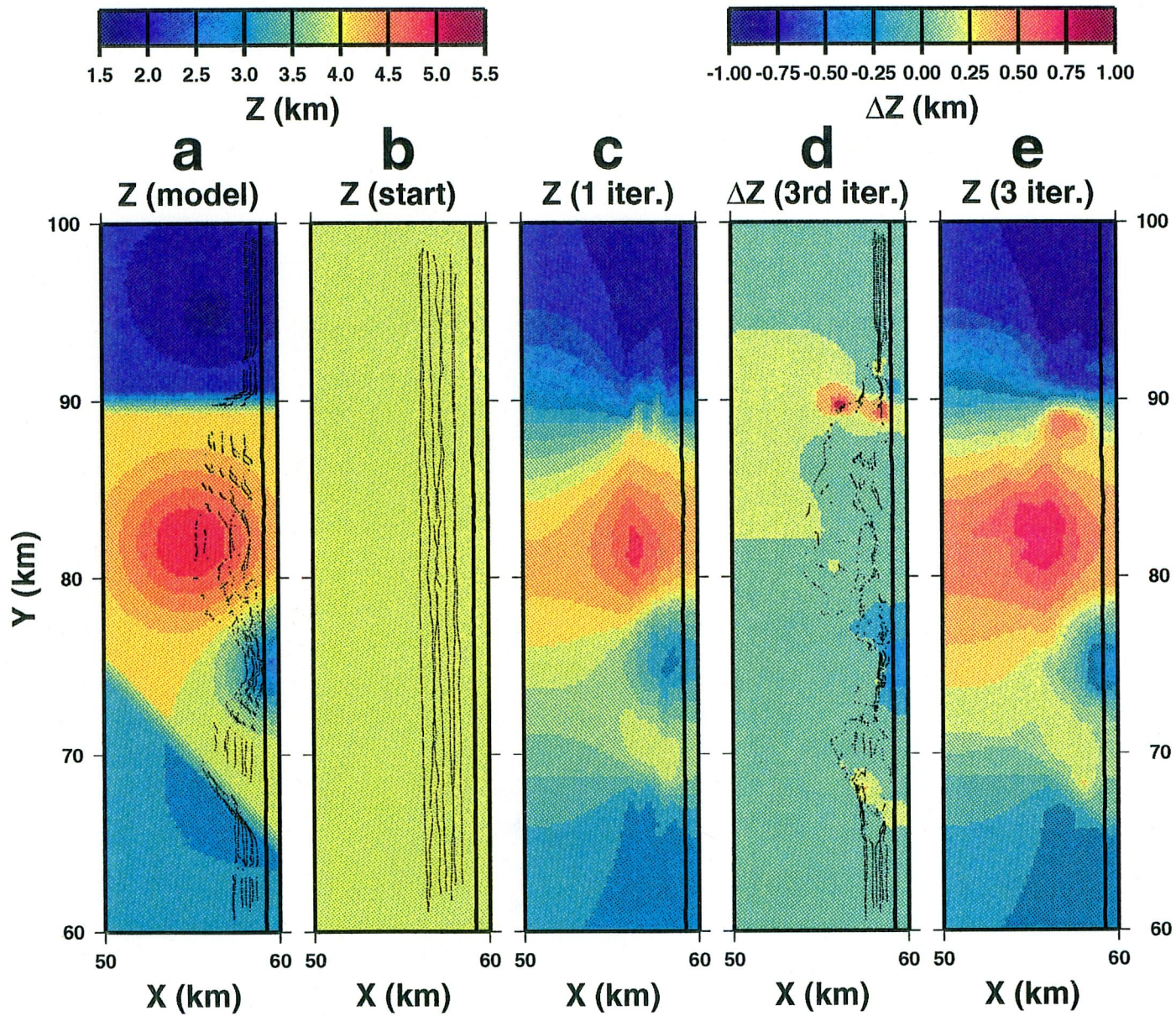
2.2.3 Synthetic Example

Using the survey geometry of Figure 2.1, a synthetic model of depth to the basement is created for the submodel area (Figure 2.3a). Included are highs and lows that are not centred on the reflection line and two faults, one of which strikes oblique to the reflection line. Basement depth varies from 1.5 to 4.9 km. Using the simple crustal velocity structure and the well log sediment velocities as discussed previously (Figure 2.2c), travel times are calculated from all of the seven receiver sites in the model area. Rays are traced back

from every third shotpoint along line 4, and their intersection with the basement interface is indicated by the series of dots in Figure 2.3a. The basement is well sampled in a swath 1–4 km wide to the west of the shot line. This coverage suggests that the broadside refraction data can be used to obtain a map of the depth to the basement and thus provide information about the offline structure of the sedimentary basin. The travel times are used as synthetic data to test the interface inversion procedure.

The starting basement model (Figure 2.3b) is flat at 3.9 km depth. Note that this is halfway between the velocity model grid points at 3.8 and 4.0 km. The true velocity model (Figure 2.2c) is used, consistent with the assumptions of the technique. The results of forward modelling indicate that the basement is apparently sampled at the points indicated in Figure 2.3b. Since these sampling points are model dependent, they differ from the true sampling points indicated in Figure 2.3a. The corrections to the model will be made at the incorrect points, and the apparent sampling points should migrate toward the real points in further iterations of the model.

Figure 2.3 (next page) Maps of the submodel area of Figure 2.1 used for the synthetic data inversion. (a) Synthetic model of depth to the basement interface. The colour scale bar is shown above. Travel time picks are taken along line 4 (the solid line at $X = 59$ km) from each receiver and used as data for inversion. Rays traced backward from the shots (at a 135 m shot interval) toward the receivers intersect the basement at the points indicated by the black dots, indicating where the model will be constrained by the data. (b) Starting basement depth model for the synthetic data inversion, showing a constant depth of 3.9 km. Rays for this model sample the basement at the black dots, showing an apparent coverage different from the real coverage in Figure 2.3a. The seven subparallel series of dots represent data points from the seven receiver stations. The lines of dots are not straight because the shot line is not straight and because of small errors in the locations of the rays due to the spatial sampling. (c) Basement depth model after one iteration. Note the similarity to the model in Figure 2.3a. (d) The change in the basement depth model added during iteration 3 and the ray coverage from the previous model that is used to create this model change. (e) The basement depth model after three iterations, derived by adding Figure 2.3d to the previous model. The final result matches Figure 2.3a very well in the region sampled by the data. Highs and lows and the strikes of both faults are well imaged.



The travel time residuals determined for the starting model are shown in Figure 2.4a. They are plotted against the Y coordinate of the point at which the ray samples the basement. The rms residual is 117 ms. The correlation of the residuals, despite the fact that they are coming from receivers at very different distances and azimuths (Figure 1.3), indicates that they are due to near-shot structure. This is obvious for the synthetic data, where the true subbasement velocity model is known, but is an important test of the modelling assumptions with real data.

The updated model after one iteration, shown in Figure 2.3c, is similar to the synthetic model that created the data. This indicates that equations (2.1) and (2.2) are a good linearization of the nonlinear inverse problem, although this may be a fortuitous result dependent on the velocity model. The highs and lows are closely approximated both in amplitude and shape under the points apparently constrained. Other parts of the model must be considered as unconstrained.

On the third iteration the apparent coverage of basement structure (Figure 2.3d) is quite similar to the true coverage (Figure 2.3a). The travel time residuals (Figure 2.4b) and the gridded change in the basement model (Figure 2.3d) are small. The rms residual is 9 ms, and the gridded depth changes are between -0.6 and 0.8 km. The changes are mainly concentrated at points where the apparent coverage had to move significantly and at steep basement slopes or faults. The basement depth model after three iterations (Figure 2.3e) is in good agreement with the synthetic model at the points in Figure 2.3d at which the survey geometry samples the basement. The portions of the basement model that are not sampled by the survey are unconstrained and are not expected to match the synthetic model. The

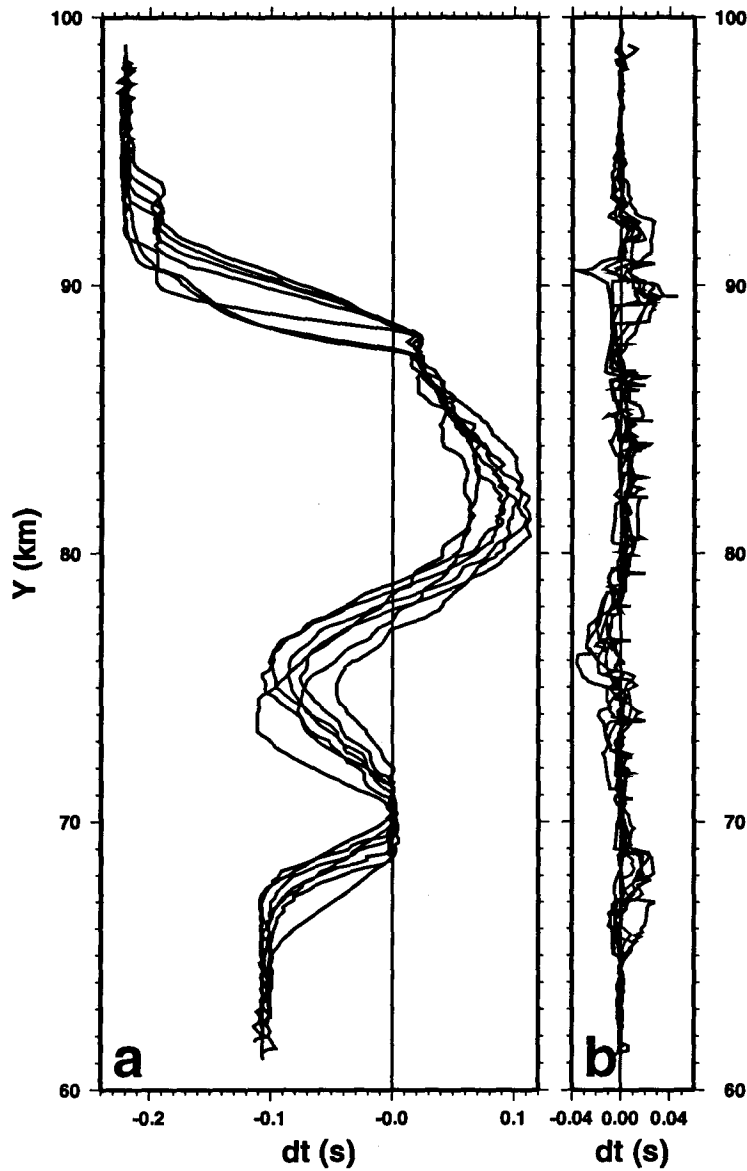


Figure 2.4 Travel time residuals for the synthetic data inversion, plotted against the Y coordinate of the location at which the ray intersects the basement. Each line represents the residuals for one receiver. (a) The residuals calculated using the flat starting model (Figure 2.3b) used in the first iteration. (b) The residuals used in the third iteration, plotted at the same scale, responsible for the model changes shown in Figure 2.3d.

strikes of both faults are well defined within the sampled region. This final basement model produces an rms travel time residual of 8 ms.

2.2.4 Discussion

The inversion procedure as described assumes a knowledge of the velocity structure and

applies all of the travel time residual to topography on the basement interface. The data do not allow differentiation between this type of solution and one which involves lateral velocity variations immediately above or below the basement. In the QC Basin the sediment velocity function is well defined, with little variation between the wells. Since many of the rays travel horizontally at depths not much below the basement, it would be difficult to fit the residuals with lateral velocity variations in the crust beneath the basement.

Further iterations in the synthetic data example have difficulties at the location of the fault at $Y = 90$ km (Figure 2.3). The first arrivals from receiver 13 measured immediately to the north side of the fault are waves that are diffracted from the bottom of the fault. The adjacent lower side of the fault is unconstrained by the data, derived only from extrapolation, and is incorrect in Figure 2.3e. This causes a travel time residual that the algorithm tries to apply to the point where the ray penetrated the basement. The assumption that the residual is due to a basement refraction is incorrect, and the algorithm arrives at an incorrect answer. If the lower side of the fault were sampled adjacent to the upper side, the problem would not occur. It is thus a problem with data coverage, resulting in one of the modelling assumptions being invalidated.

The interface inversion scheme is computationally efficient, as indicated by CPU times on a Sun 4/280 workstation. To perform the modelling for a single receiver took about 110 s in the coarsely sampled model, 450 s in the submodel, and 100 s to find the rays and derivatives of equation (2.1). Only the third step is dependent on the number of rays recorded in the data. All three steps are independent of the velocity structure, depending only on the number of grid points in the model. Subsequent iterations do not need to repeat

the coarse modelling step. The three steps are repeated for each common receiver gather; then the data are inverted using equation (2.2), taking 30 s for the 2000 data. The final step of gridding the model perturbation took about 60 s.

2.2.5 Conclusions

The recent collection of high-density broadside seismic refraction data sets recorded from large airgun source arrays has required the development of a new interpretation tool. An efficient procedure has been described to invert first arrival travel times from such data for the position of an interface beneath the shot line. The basis of the forward modelling is a finite difference algorithm which allows the rapid calculation of travel times in 3d media. This algorithm has been modified so that a variable grid spacing can be used and rays can be found. A model parameterization that eliminates the need to invert a large matrix was chosen for the inversion. The entire procedure is computationally rapid. A synthetic data example has been used to demonstrate that the procedure is capable of determining the structure of an interface offline from the shots.

2.3 Structure of the Queen Charlotte Basin

2.3.1 Introduction

Because of the complex structure of the QC Basin beneath the shot lines, the refraction data exhibit rapid lateral variations of the travel times (Figure 1.4, Appendix A). These variations provide information about the structure of the basin beneath the shot lines. The information from the broadside refraction data includes structure out of the planes of the reflection sections. This section presents results from the inversion of the refraction data in

western Hecate Strait (Figure 1.1) using the interface inversion algorithm described in the previous section. The resulting model of the thickness of the QC Basin is discussed in terms of other geophysical data sets and tectonic models.

In this section, “basement” will generally be defined as the base of the pure sedimentary Tertiary section, as identified by a sharp seismic velocity contrast of at least 1 km/s. In regions where the deeper part of the Tertiary basin includes a high proportion of volcanics, the seismic refraction basement and Tertiary basement will not coincide.

2.3.2 Data

The first arrival travel times for all shot lines and receivers within the study area of Figure 2.5 were picked on an interactive graphics display terminal. The procedure was facilitated by the small trace spacing (135 m after binning) which provided excellent correlation between traces. Beyond about 110 km offset (e.g., shotpoints 2600 to 3473 on Figure 1.4a, 101 to 600 on Figure 1.4b) the first arrivals become very weak and often were not picked. Noisy data (e.g., site 18), emergent first arrivals, and the difficulty of picking the true first arrival across an entire section reduced the accuracy of some of the picks. The overall accuracy, however, is excellent, typically within a quarter wavelength or about 25 ms. A total of 10081 travel times are inverted to determine the structure of the QC Basin.

2.3.3 Interpretation Method

The travel time data are inverted using the procedure described in the previous section. The procedure assumes a knowledge of the sedimentary and subbasement velocity structure, but the latter can be modelled only after removing the basin structure. In practice, the

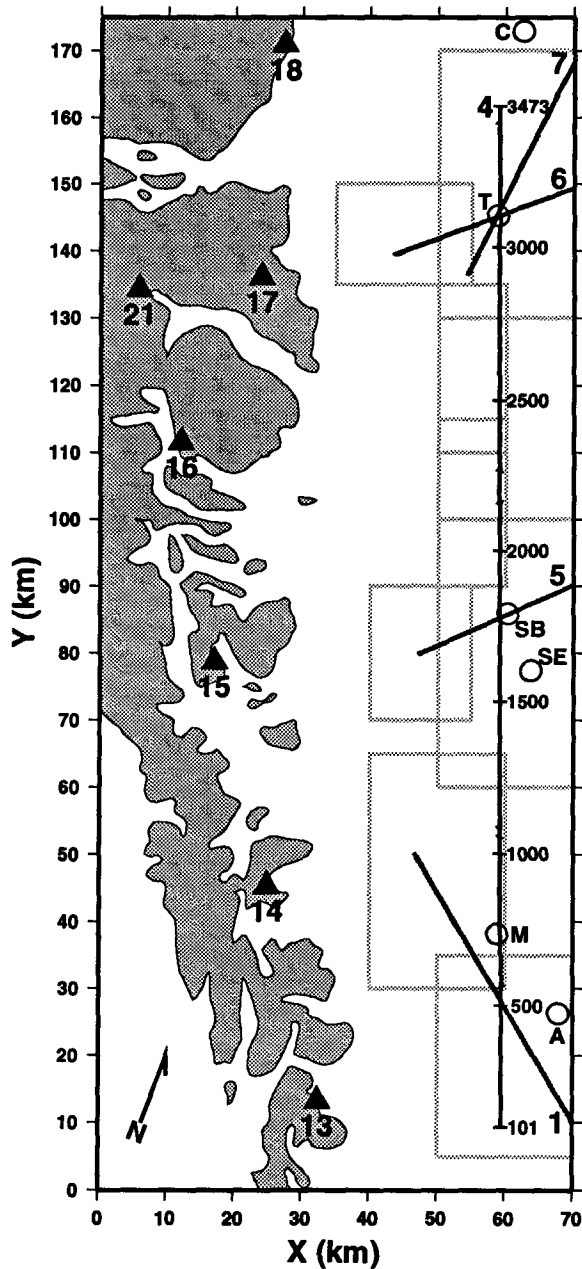


Figure 2.5 Map of the study area, showing the QC Basin seismic survey shot lines and refraction seismograph sites. The symbols used are the same as for Figure 1.2. Eight submodel areas are outlined in light grey. The wells are labelled: C, Coho; T, Tye; SB, Sockeye B-10; SE, Sockeye E-66; M, Murrelet; A, Auklet.

subbasement velocity and the basin structure near the reflection line must be modelled together, iterating from one to the other until a satisfactory match is obtained.

The data were initially corrected for basin statics using picks from the 2d reflection data, and a preliminary 1d crustal velocity profile was determined from the corrected data.

The basin was modelled in three dimensions using this 1d crustal profile, the data were re-corrected for 3d basin statics, and then a better 1d average crustal model was determined. This final 1d average of the crustal structure (Figure 2.6) is used to invert the relative travel time residuals to obtain the 3d basin model presented here. A 1d sedimentary basin velocity structure (Figure 2.6), based on sonic logs from the 6 wells shown in Figure 2.5, is used above the basement interface. The inversion procedure can use any 3d velocity models above and below the basement interface, but 1d models are used due to the similarities of the 6 Hecate Strait well logs and the preference to accurately model shot statics before crustal structure.

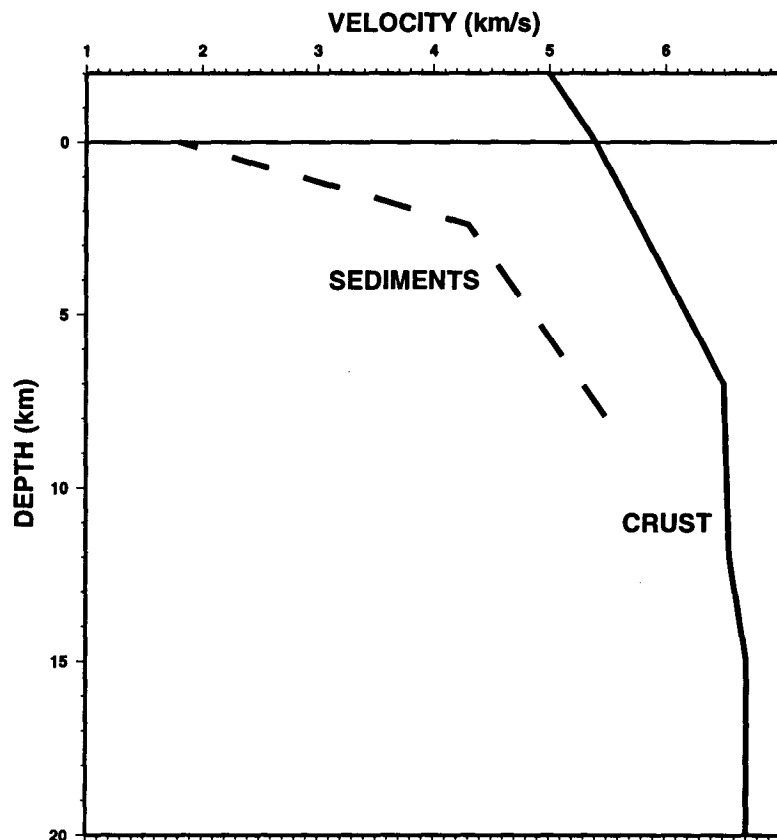


Figure 2.6 One-dimensional velocity profiles used in the inversion. The solid line is the crustal velocity profile used below the 3d depth-varying basement interface, and the dashed line is the sedimentary basin profile used above the basement. Zero depth is sea level.

Travel times through the crustal model are calculated using a 1 km grid spacing.

However, near the reflection lines where the shot spacing is small and the velocity variations associated with the sedimentary basement are large and complex, the model is sampled at a 200 m grid spacing. Because of the large number of grid cells when using a 200 m spacing, the finely sampled portion of the model is split into eight overlapping submodel regions (Figure 2.5) and inversions are performed to find the basement depth separately within each region. For each submodel, the starting basement depth model is a horizontal flat surface. Testing indicates that the resulting models are independent of the starting model.

The travel time residuals within a submodel are not entirely due to variations in the basement depth. Errors in the simple crustal model affect the residuals for the different receivers differently. In addition, receiver statics may exist due to near-receiver structure or due to picks of different cycles on data from different receivers. For these reasons, a constant static time shift is applied to each receiver in order to set the average residual for that receiver to zero. The small size of the submodel restricts the range in offset and azimuth for each receiver, helping to ensure that a constant static shift is adequate to remove effects due to errors in the crustal velocity model. An additional global constant static time shift is added to all of the receivers so that the inversion results within the submodel match the basement depth in a well or in a part of the reflection data where the basement is shallow and well defined. The global static for each submodel is also adjusted to match depths with overlapping submodels. For further iterations, the receiver statics are recalculated to ensure that the average residual is the same for all receivers. Because the assumption of a constant static shift is probably insufficient to account for errors in the velocity model, the overall accuracy estimate for the corrected picks is increased to 40 ms. These errors

produce high spatial frequency noise in the gridded basement depth model, a characteristic which is removed by nine applications of a 3×3–point moving average filter. This smooths the effects of any single travel time data point over a 2 km radius so that the depth at each location is based on many rays.

Models derived for the different submodel regions are merged and smoothed to provide a final model of gridded basement depths. The small submodel sizes and the large overlaps between submodels ensure that the mismatches in the overlap zones are within the depth error estimates based on the travel time data.

2.3.4 Results

A map of the final model of depth to the sedimentary basement is shown in Figure 2.7. The series of dots in Figure 2.7*a* indicate the locations where the rays from each shot-receiver pair intersect the basement. The basement model is constrained only at the locations of these points. The points define a swath of information a few kilometres wide and offline from the reflection lines. Portions of the model outside this region of ray intersections are simply extrapolations and are unconstrained. Mismatches in the overlap zones between submodels are restricted to unconstrained portions of the model. The basement depth map in Figure 2.7*b* shows that the basin thickness varies between ~200 m and ~6 km in a series of complex structures.

Figure 2.7 (next page) Maps of the basement depth model, corresponding to the submodel regions of Figure 2.5. (a) The solid lines indicate the shot profiles. The dots mark the locations at which the rays to the offline receivers intersect the basement model, showing where the model is constrained by the data. Four major faults which displace the basement are interpreted from the depth model and are indicated in red (labelled F1 to F4). (b) Colour contoured map of the basement depth model. The colour scale is shown above. The contour interval is 1 km. The depth to basement varies between near zero and more than 6 km.

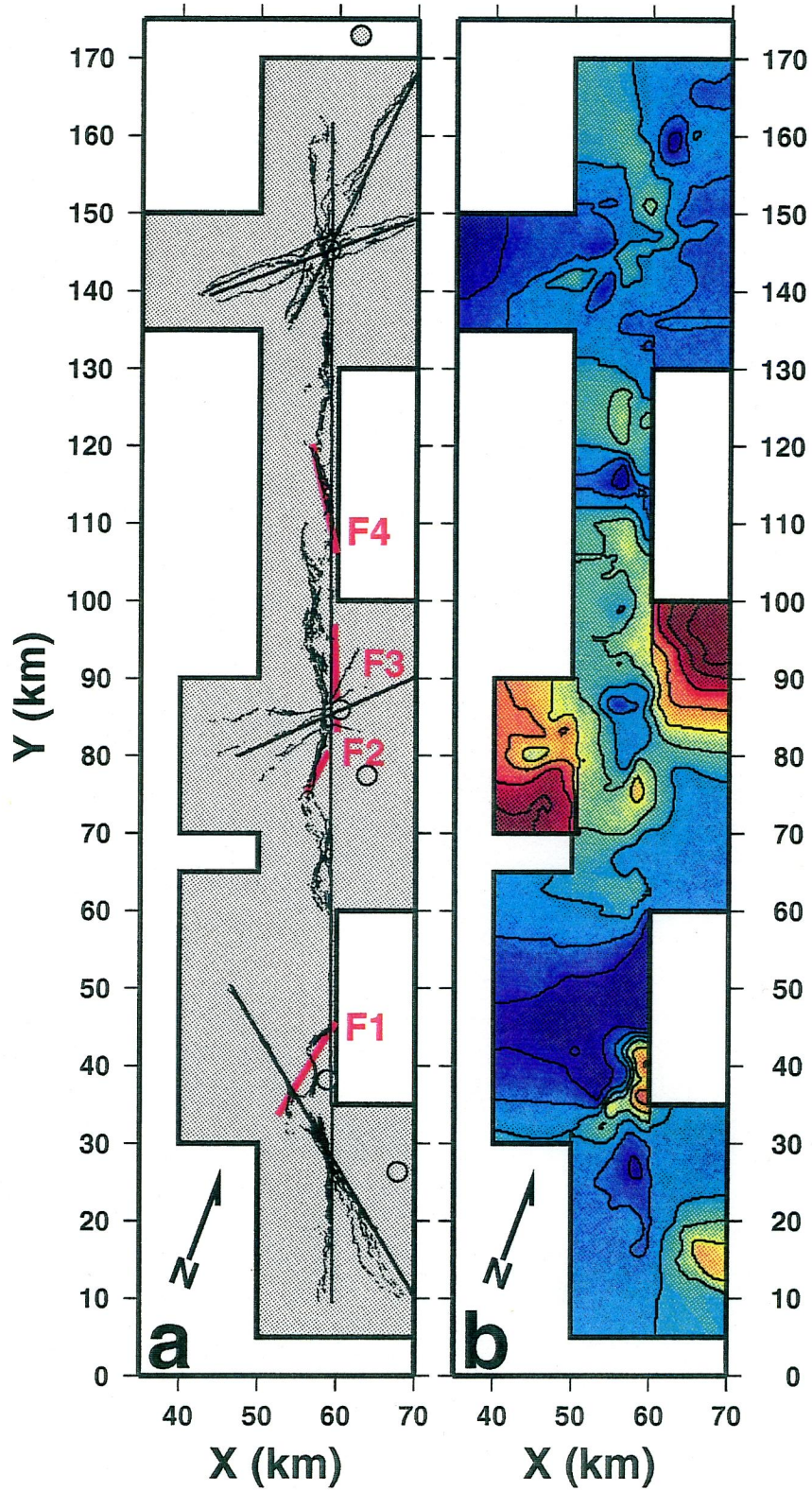
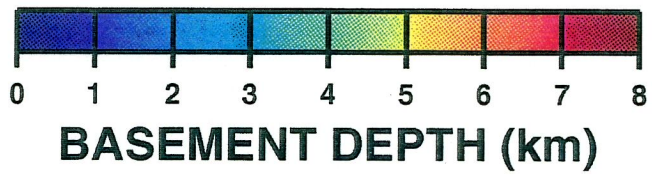


Table 2.1 summarizes the inversion parameters and model fit within each of the eight submodels. The average travel time residual (average dt) is related to the average misfit between the model and the actual basement depths and should be zero for the final model. The root-mean-square residual (rms dt) is a measure of misfit of the data and, for the final model, should be similar to the error estimate of 40 ms for the travel time data. Figure 2.8 illustrates the data fit for shots along line 4 within the submodel between $Y = 60$ and 100 km. The travel time residuals for the starting model (Figure 2.8a) average 35 ms, indicating that the true basement structure averages deeper than the starting depth of 3.9 km. The curves for the seven receivers cross-correlate very well, confirming that the residuals are due to structure near the shot line. The residuals after three iterations (Figure 2.8b) average zero, and are random. The rms misfit is 35 ms, similar to the estimated data errors. As summarized in Table 2.1, the data fit within the other submodels is also very good. The receiver statics vary over several hundred milliseconds. Differences in these statics between submodels are caused by errors in the crustal velocity model and are averages of the data used to invert for 3d crustal velocity structure (Chapter 3).

The inversion procedure assumes a knowledge of the velocities above and below the basement interface and applies all of the travel time residual to topography on the interface. Based on these data, this type of model cannot be distinguished from one that involves lateral velocity variations immediately above or below the basement. As there are only small velocity variations among the six well logs, it is inferred that the sedimentary velocity model is very good. Since many of the rays travel horizontally at shallow depths below the basement and at a wide range of azimuths, it would be very difficult to fit the rapid travel time

Table 2.1 Inversion and model fit statistics.

Y range (km)	X range (km)	Number of receivers	Number of travel times	Depth (km) for starting submodel	Average dt (s) for starting submodel	rms dt (s) for starting submodel	Number of iterations	Average dt (s) for final submodel	rms dt (s) for final submodel	Statics (s) for receivers 13, 14, 15, 16, 17, 18, 21
5 - 35	50 - 70	6	1565	1.9	.042	.122	3	.003	.021	.183, .078, -.133, -.010, .022, na, -.123
30 - 65	40 - 60	6	2223	1.9	-.067	.238	3	-.002	.059	.273, .074, .001, -.023, .117, na, -.039
60 - 100	50 - 70	7	2153	3.9	.035	.109	3	.000	.035	.162, .025, -.013, .105, .138, -.262, -.080
70 - 90	40 - 55	4	230	3.9	.104	.142	3	.000	.041	.167, na, -.021, na, na, -.260, -.085
90 - 115	50 - 60	7	1128	3.9	-.023	.067	3	-.002	.033	.078, -.040, .020, .176, .040, -.207, .004
110 - 135	50 - 60	7	1060	3.9	-.088	.117	3	-.001	.036	.026, .012, -.012, -.015, -.115, -.304, -.083
130 - 170	50 - 70	6	2465	3.9	-.097	.122	3	-.001	.028	na, -.048, -.067, -.146, -.302, -.546, -.115
135 - 150	35 - 55	4	386	0.9	.270	.283	3	.007	.056	na, na, -.064, na, -.304, -.543, -.112

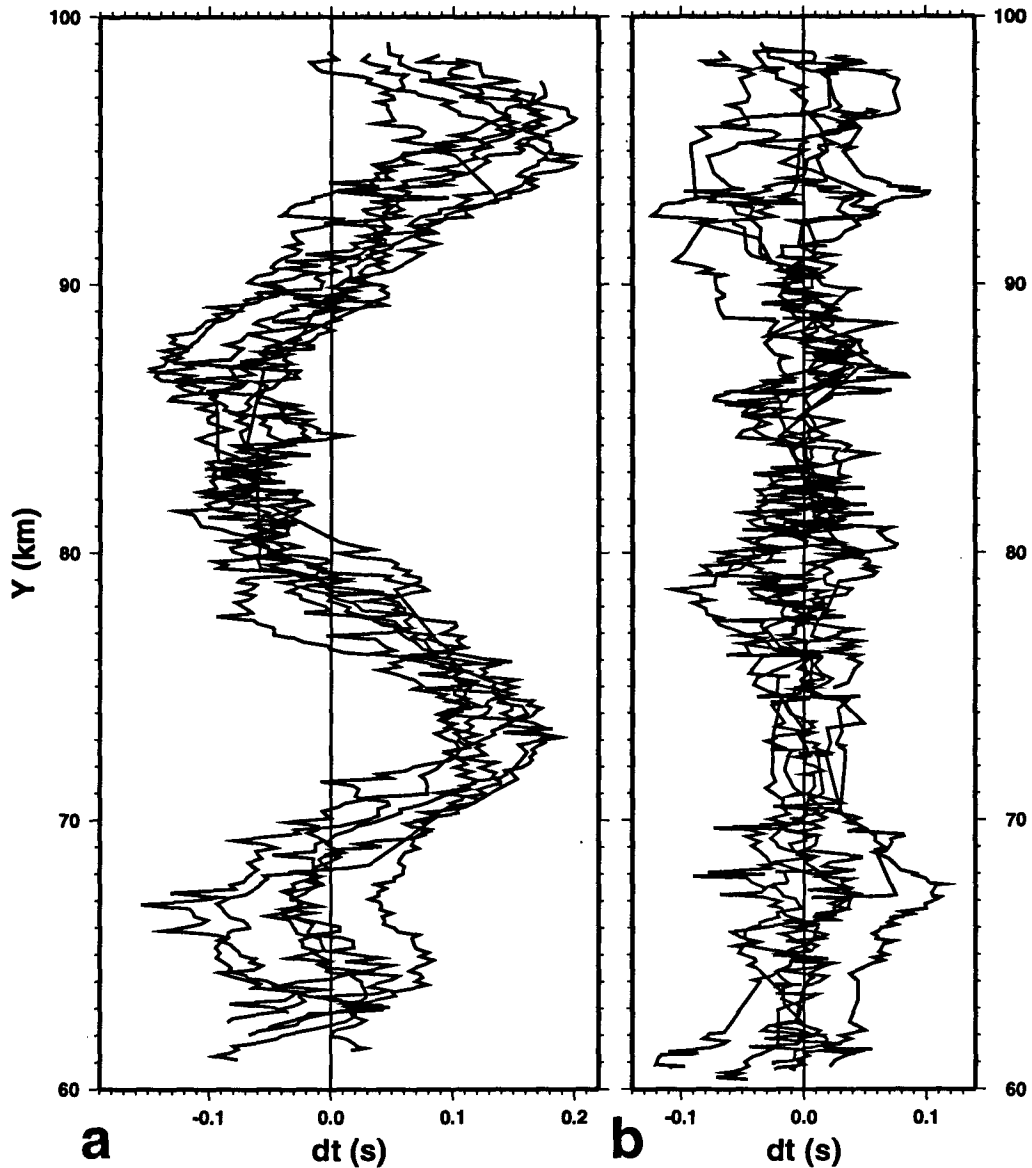


Figure 2.8 Travel time residuals for a portion of the line 4 refraction data. Each line represents the residuals (dt) for one receiver, plotted against the Y coordinate of the location at which the ray intersects the basement. (a) The residuals calculated using the horizontal basement starting model. (b) The residuals computed using the final basement model of Figure 2.7.

undulations with reasonable lateral velocity variations within the crust immediately beneath the basement. Thus, the detailed structure of the basin (at a horizontal scale of less than 10 km) is probably well resolved. The larger scale structure (tens of kilometres) is subject to errors in the crustal velocity model. Within each submodel, the large scale structure is tied to the basement depth as measured in wells or by selected high quality picks of the

reflection data. This ensures that the largest scale basin structure (larger than a submodel) is accurately mapped.

Applying the preceding assumptions, an estimate of the depth resolution of the model is possible. Using the 40 ms estimate of accuracy for the travel time picks after receiver statics and typical values for the linearized relation between travel time and basement depth (equation 2.1), the accuracy of the depth due to a single ray is about 0.4 km. The smoothing of the gridded model ensures that the model at each grid point is determined from many rays, and therefore the depth resolution of the basement model is expected to be better than 0.4 km. Accordingly, the model depths are estimated to be accurate to about 0.3 km within the swath of data constraints shown in Figure 2.7a. Depths outside of this region are unconstrained, within the limit that changes to the model outside the constrained region cannot allow new rays to arrive as first arrivals.

2.3.5 Interpretation and Discussion

2.3.5.1 Basement Depth Model

Four major basement faults, each of which is recognized as a steep scarp with more than two kilometres of vertical relief on the basement interface, are interpreted from the basement depth model. These faults are indicated in red in Figure 2.7a and can be seen in Figure 2.7b as closely spaced contours. A larger scale plot of the structure in the region of Fault 4 is shown in Figure 2.9. Faults 2 and 3 and the basement high west of Fault 3 were not recognized in an initial interpretation of the reflection data (K.M.M. Rohr and J.R. Dietrich, personal communication, 1990), even though both faults exhibit over 2 km of vertical relief.

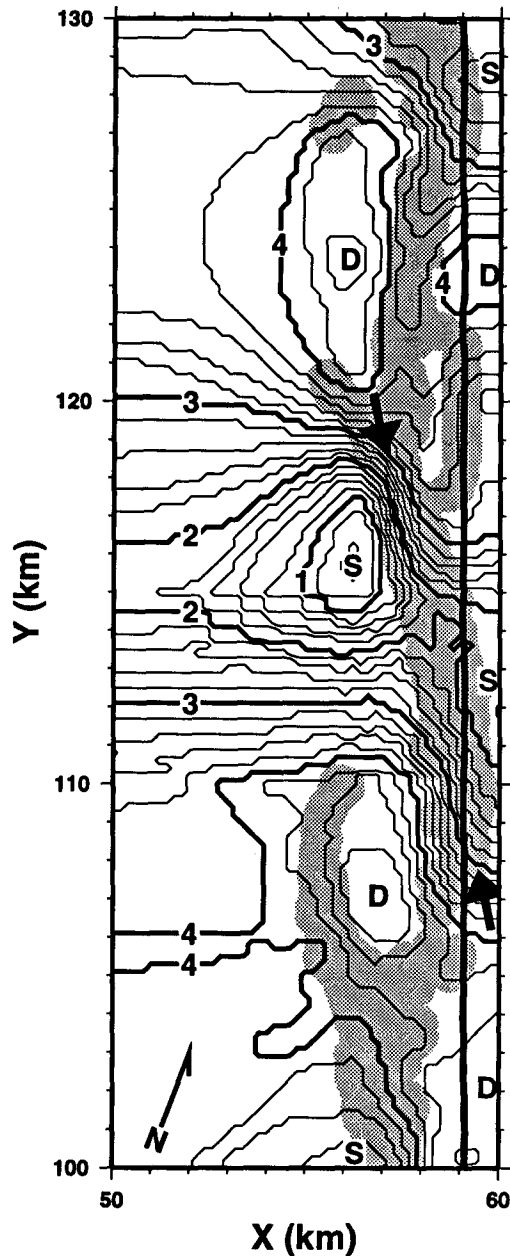


Figure 2.9 Map of the basement depth model in the region of Fault 4. The thick line at $X = 59$ km is shot line 4. The grey shading indicates the locations where the rays intersect the basement model, showing the region constrained by the data. The model is gridded horizontally and vertically at a 0.2 km interval. The basement depth contour interval is 0.2 km; thicker contours are labelled at 1 km intervals. Basement peaks and troughs are marked S(hallow) and D(eep). Fault 4 is interpreted to extend between the two arrows.

The reflection data were difficult to interpret due to the complex pattern of reflectivity in this region and the fact that line 4 lies along the major scarp of Fault 3 (Figure 2.7). Faults 2, 3 and 4 are all shown in the basin thickness map of *Rohr and Dietrich* [1992], who

used the preliminary results from this work to reassess the reflection data, but all strike in directions slightly different than in this model. The 3d nature of the refraction information provides stronger constraints on the fault orientations. Fault 1 bounds the southeast side of the Moresby Ridge, a known basement high extending from the QC Islands and crossing line 4 at $Y = 45$ to 55 km. This fault has at least 4 km of vertical relief and bounds a half-graben that is well expressed in the reflection data [Rohr and Dietrich 1992]. Only those faults with significant scarps on the basement (at least 1 km of vertical relief) are recognizable in the model of Figure 2.7, and thus one or more major faults through the constrained region may be missing in the refraction interpretation.

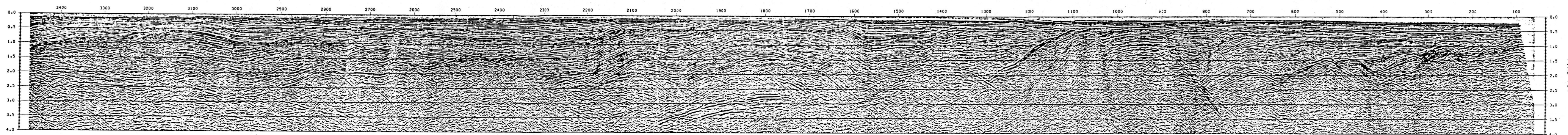
The basement depth model of Figure 2.7 is derived solely from the refraction data. The model can be compared to the reflection data as a check on the modelling assumptions and to better interpret the basement structure. The unmigrated multichannel reflection data along lines 4 and 5 are shown in Figures 2.10a and 2.11a. The basin structure along line 4 is complex, even though it is nominally a strike line for the basin. The sedimentary basement picked from the reflection data and converted to depth compares well with cross sections through the basement depth model of Figure 2.7 (Figures 2.10b and 2.11b). Some of the differences between the profiles are due to the fact that the refraction constraints for line 4 lie a few kilometres west of the line and therefore map offline structure. In general, the structures of specific basement highs and lows are in excellent agreement between the refraction and reflection interpretations.

Fault 1 is clear in the line 4 reflection data between shotpoints 800 and 900 (and shotpoints 4950–5000 on line 1, not shown), bounding the northern edge of a large half-graben. Fault 2 is observed at shotpoints 1600–1650. Line 4 lies along the top of Fault 3 from $Y = 84$

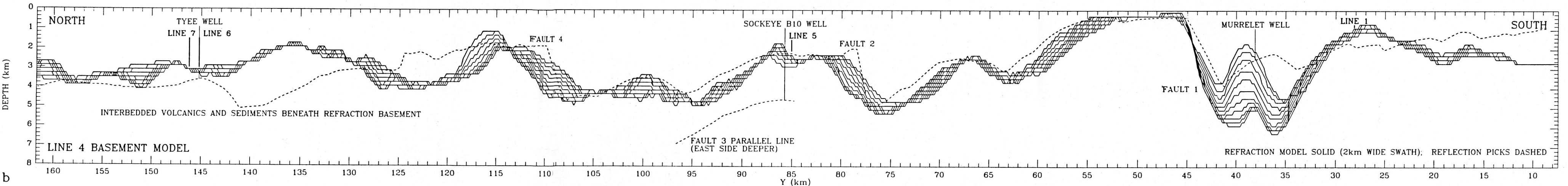
to 96 km (shotpoints 1750–2000). The basement on both sides of this fault is imaged on the reflection data: the shallower western side is imaged as a change in reflectivity (at about 1.6 s at shotpoint 1800), while the deeper eastern side is responsible for a large amplitude reflection (at about 2.7 s). The Sockeye B-10 well penetrates the basement on the deeper side of the fault at 2.6 s only 1.2 km east of line 4 along line 5. Fault 3 is also imaged in the reflection section for line 5 at shotpoint 400 (Figure 2.11), beneath the intersection with line 4. Fault 4 is imaged in reflection line 4 at shotpoint 2300.

Interbedded Tertiary sediments and volcanics are interpreted in several parts of the basin based on reflection structures [Rohr and Dietrich 1992], wells [Shouldice 1971], and geological mapping on land [Higgs 1991; White 1990]. The Tertiary volcanism, and hence the interbedding, is restricted to the earlier, deeper stages of basin deposition. One example of such interbedding is the structure mapped in the line 4 reflection data near shotpoint 700 and sampled near the base of the Murrelet well (Figure 2.10). Strong reflectivity from 1.7 to 2.5 s at shotpoint 700 is caused by the interbedded rocks. In the northern part of the study area near the intersection of lines 4, 6 and 7 (Figure 2.5), the sedimentary basement is difficult to pick in the reflection data [Rohr and Dietrich 1992]. The Tyee well in this region bottoms

Figure 2.10 (next page) (a) The upper 4 s of line 4 unmigrated stacked multichannel reflection data, annotated by shotpoint number. The two-way travel time to the sedimentary basement is picked from these data and converted to depth using the sedimentary velocity-depth curve of Figure 2.6. (b) Depth-distance profile along line 4 at a vertical exaggeration of 2:1. The basement depth picked from the reflection data is shown as a dashed line. The solid lines represent 11 parallel profiles through the refraction basement model of Figure 2.7 from a 2 km wide swath parallel to and immediately west of the shot line. The reflection and refraction basement models are in good agreement, but were obtained independently. The locations of wells (vertical lines show depth of penetration), intersections with other lines, and interpreted faults are indicated. In the region where Fault 3 runs parallel to line 4 (Y = 84 to 96 km), reflections from both sides of the fault are imaged in the reflection data and are shown in the depth profile.



a



b

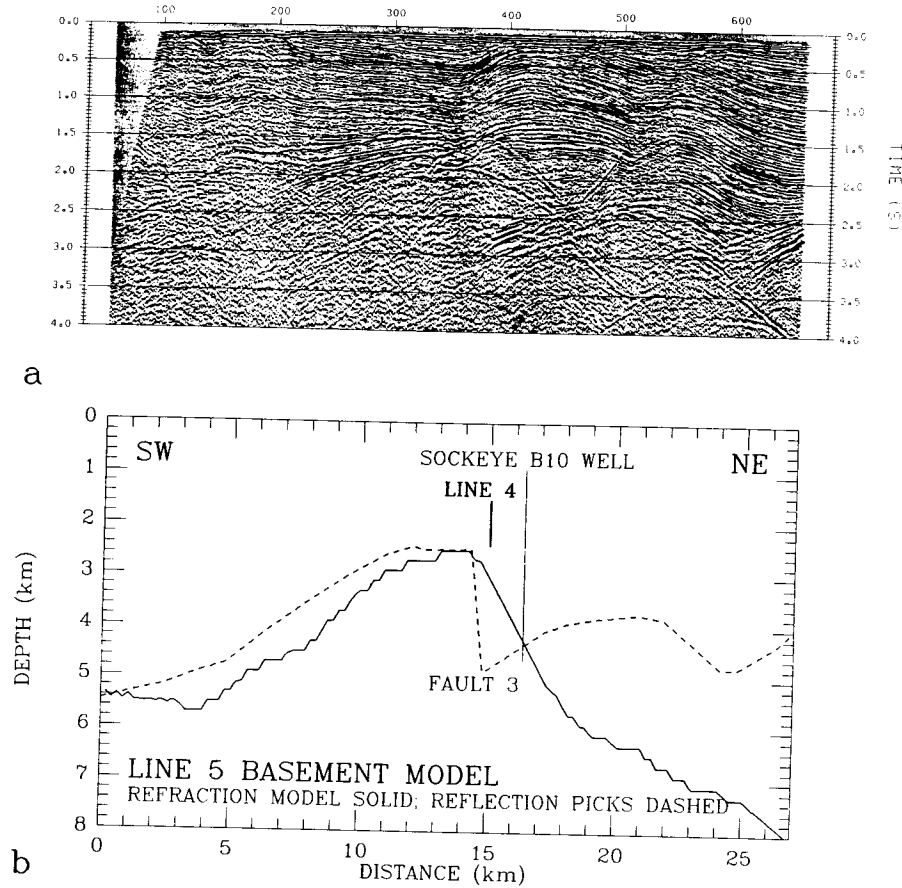


Figure 2.11 Similar to Figure 2.10 for the portion of reflection line 5 that lies within the study area. In (b), only a single profile through the refraction model along the reflection line is shown. The refraction model is unconstrained northeast of 19 km distance due to a lack of ray coverage in the inversion (Figure 2.7a).

in Cretaceous sediments and older plutonic rock [Haggart 1991]. A thick sequence of high amplitude, relatively low frequency reflectivity extends beneath the base of the well (Figure 2.10a). A thick sequence of interbedded sedimentary and volcanic rocks is interpreted to lie within the deepest part of the Tertiary basin, corresponding to the high amplitude reflectivity. The sequence is interpreted to extend beneath the plutonic rocks drilled in the Tye well; Rohr and Dietrich [1992] suggest that these rocks may have been thrust up into the Tertiary sequence. The absolute depth of the refraction basement model in this region is tied to the base of the Tye well. The interpreted interbedded sequence lies beneath the basement model

north of $Y = 125$ km (Figure 2.10b). Since the velocities of this sequence are expected to be laterally variable and intermediate between the sedimentary and crustal velocity models used in the inversion (Figure 2.6), the basement structure shown in this portion of Figures 2.7 and 2.10 represents the results from some average of the true velocity structure. Thus, the basement structure modelled using the refraction data lies above the true Tertiary basement and has a topography that represents neither the true basement nor the top of the interbedded sequence. Subsequent inversion of the refraction data for 3d subbasement crustal structure (Chapter 3) indicates that the velocities below the basement of Figure 2.7 are 0.3 to 0.7 km/s lower than the average 1d crustal model (Figure 2.6) in the northern portion of the study area down to a depth of 6 or 7 km, in agreement with the interbedding interpretation.

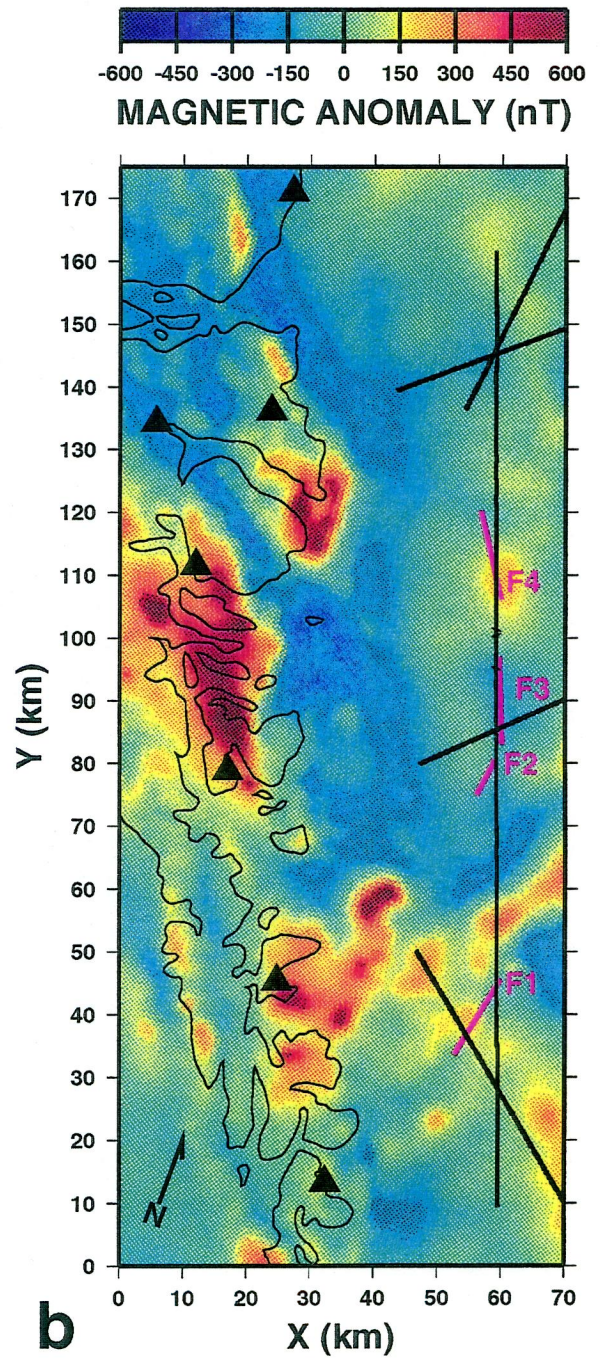
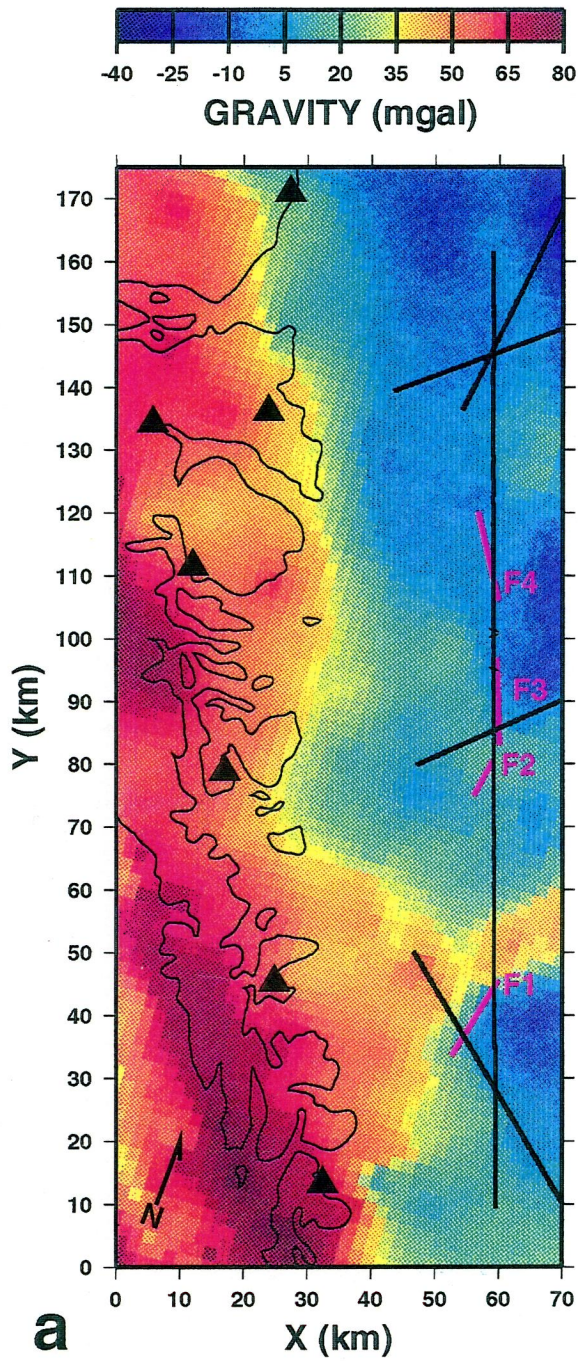
In the southernmost part of the study area, south of $Y = 25$ km, the shape of the basement model matches the reflection picks for lines 4 and 1, but the model slopes too steeply to the south (Figure 2.10). This can be caused by true velocities in this region that decrease southwards from the assumed velocities of Figure 2.6. The water deepens gradually (from less than 100 m to over 200 m) at the southern end of the study area and can only be poorly modelled by the 200 m vertical grid spacing. In addition, *Yuan et al.* [1992] present evidence that the sedimentary velocities and densities decrease toward central QC Sound due to an increasing proportion of high porosity marine sediments. Both of these factors probably contribute to the mismatch because they cause the true velocities in this region to be lower than the velocities used in the inversion.

Comparisons can also be made between the basement model and potential field data sets. Due to the large density contrast between the Tertiary sediments and the underlying crustal

rocks, the gravity data should show relatively negative anomalies that outline the subbasins and correspond to increased basin thickness [Stacey 1975; Sweeney and Seemann 1991]. In map view, the gravity data (Figure 2.12a) outline the subbasins in a general sense, correlating well with the basement map of Figure 2.7. The deepest subbasins at $Y = 40$ km and 95 km are visible as pronounced negative anomalies. Similarly, the large basement high at $Y = 50$ km and the smaller high west of Fault 3 are clearly seen in the gravity map. Faults 1 and 3 both correlate with rapid changes in the gravity field, and the side of each fault with thicker sediments produces the more negative gravity anomaly. Faults 2 and 4 have smaller vertical relief and may be near the spatial and anomaly resolution of the gravity data. Two-dimensional density models along lines 4 and 5 incorporating only horizontal sedimentary layers and the basin thickness as determined from Figure 2.7 produce an excellent match with the observed gravity anomaly (Figure 2.13). Considering the 3d nature of the basin, the lack of constraints off the ends of the lines, and the possibility of density variations in the underlying crust, the correspondence supports the basement model of Figure 2.7. Note that the computed gravity field is more positive than the observed in the northern part of the line 4 profile. This is consistent with the interpretation of interbedded sediments and volcanics, and therefore lower densities, beneath the refraction-derived basement.

The sediments affect the anomalous magnetic field only as a non-magnetic blanket weakening the effects of the underlying rocks due to increased depth. The magnitude

Figure 2.12 (next page) (a) Map of gravity within the study area, plotting Bouguer onshore and Free Air offshore (data from the Geological Survey of Canada Geophysical Data Centre). Although gridded at a 2 km spacing, most of the map region is poorly sampled at a data spacing of 5 to 10 km. (b) Map of magnetic intensity anomaly within the study area gridded at 812.8 m (same data source). On both maps, the four interpreted major basement faults are shown in magenta. The shot lines and receiver locations are shown as in Figure 2.5.



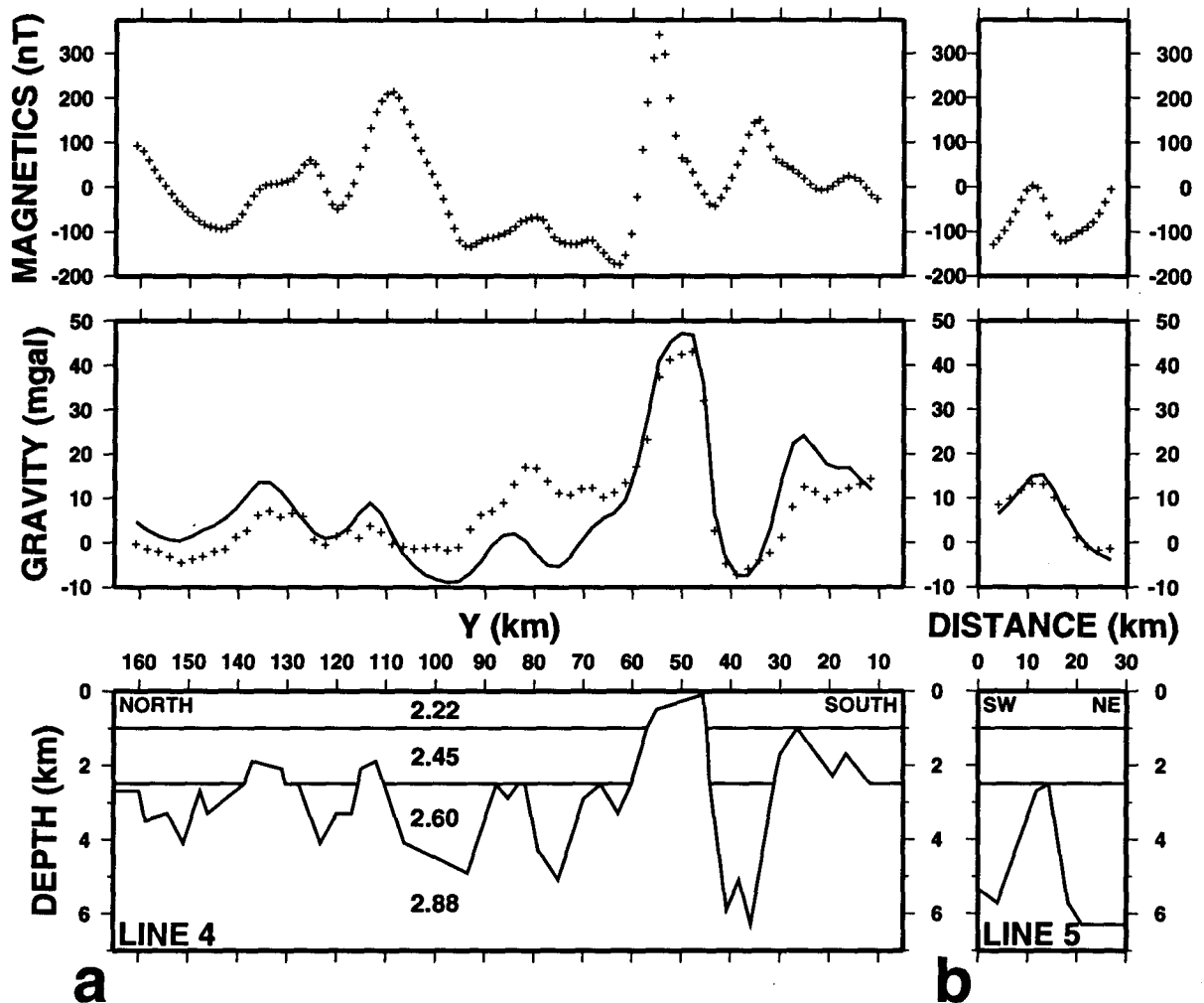


Figure 2.13 Two-dimensional density models along (a) line 4 and (b) line 5, incorporating only simplified variations in basin thickness determined from Figure 2.7. Density values for both lines are shown in (a) in g/cm^3 . The sedimentary density values are from *Sweeney and Seemann* [1991]. Above each model is the resulting gravity profile (solid line) compared to the observed data (symbols). The calculated and observed gravity are in excellent agreement, considering that the offline and subbasement density structures have not been modelled. The observed magnetic intensity anomaly is also shown and exhibits correlations with basement topography.

of magnetic anomalies should therefore be damped by thicker sediments. The magnetic intensity anomaly map (Figure 2.12b) shows strong magnetic anomalies over portions of the QC Islands and the thinly sedimented Moresby Ridge (basement high at $Y = 50$ km), but relatively muted anomalies over most of the QC Basin. Contrasts in the magnetic field can be correlated with all four of the interpreted major basement faults, and the side of each fault with thicker sediments produces a more negative magnetic anomaly. This observation

is interpreted by assuming that the underlying rocks create a positive magnetic signature which is damped by the varying thickness of sediments. The basement high west of Fault 3 is visible in both the magnetic and gravity maps, supporting the complex features interpreted in this region. A strong positive magnetic anomaly is present over the shallower eastern side of Fault 4 where it crosses line 4. Profiles along lines 4 and 5 (Figure 2.13) demonstrate that contrasts in the magnetic data correlate well with the basement structure.

2.3.5.2 *Tectonic model*

The model of the sedimentary basement depth determined from the 3d refraction data (Figure 2.7) is consistent with the other geophysical data sets, lending support to the features mapped. These features can be used to constrain the tectonic models of the formation of the QC Basin. *Rohr and Dietrich* [1992] use a regional strike-slip stress field to predict the orientation and motion of major faulting for comparison with fault patterns observed throughout the basin. They use the resulting correspondence as one of their arguments for a tectonic model incorporating distributed strike-slip extension. Faults that strike northwest, parallel to the plate margin off the west coast of the QC Islands (Figure 1.1), should exhibit dextral strike-slip motion. Faults 3 and 4 both strike approximately northwest, and therefore should exhibit dextral strike-slip motion based on their model.

The structure across Fault 4 has not been well sampled by the broadside refraction data because the strike is in a similar direction to line 4 and there is no cross line in this region (Figure 2.9). In the portion of the fault near line 4, however, the structure is well determined because the pattern of the basement, deep further away from and high nearer the shot line, is easier to resolve than the structure further north, and a major fault is clearly imaged in

the reflection data in this region (Figure 2.10). The northwestern portion of the fault is less well constrained because the fault is further from the line, the basement high is further away from the shots than the basement deep (Figure 2.9), and the match with the reflection data in this region is poorer (Figure 2.10, shotpoints 2500–2550). Supporting the interpretation of the northwestern portion of the fault is its excellent match with the strike of the southeastern portion (Figure 2.9) and the quality and character of the refraction first arrival from this region at several receivers. The vertical relief on the fault's southeastern mapped portion (where it crosses line 4) is about 2 km with the westward side deeper (Figure 2.9). A short distance along the fault towards the northwest, the vertical relief is of about the same magnitude but with the deep and shallow sides reversed. In order to interpret this fault using only vertical motions, the movement on the fault must reverse directions along strike. A simpler interpretation involves lateral motions. The observed pattern can be explained by dextral strike-slip motion cutting a pre-existing basement high (Figure 2.14a). Based on the topography observed in Figure 2.9, the basement high on the eastern side where the fault crosses line 4 seems to have been displaced northwestwards on the western side of the fault by ~5 km.

The vertical relief across Fault 3 is also consistent with dextral strike-slip. This fault is well determined from the refraction data for lines 5 and 4, the Sockeye B-10 well, and the reflection and potential field data. The basement on both sides of the fault dips towards the north. If a pre-existing smooth surface that dips to the north is cut by a northwest striking fault and is displaced in a dextral strike-slip sense, the west side of the fault would be shallower (Figure 2.14b), consistent with the vertical relief across Fault 3. Faults 3 and

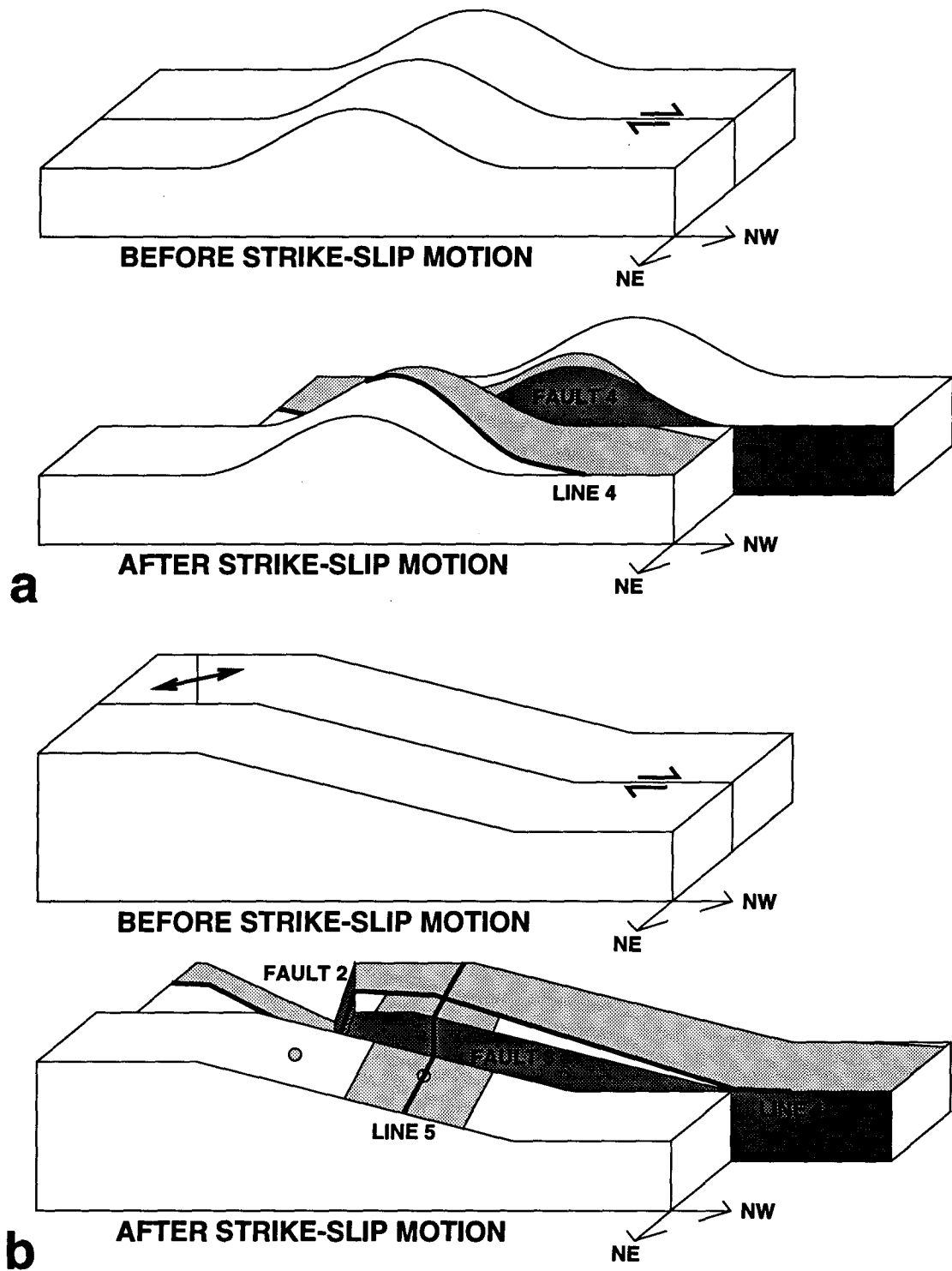


Figure 2.14 Sketches showing how dextral strike-slip faulting can be used to explain portions of the basement topography. The thick lines indicate the shot lines and the light grey shading is the region of coverage of the 3d refraction data. The dark grey shading indicates the faces of the faults. (a) The structure at Fault 4 is readily explained as a dextral strike-slip fault offsetting a pre-existing basement high. (b) Faults 3 and 2 may correspond to a dextral strike-slip fault and a pull-apart normal fault, respectively, north of the Moresby Ridge. The locations of the Sockeye wells are indicated by circles.

4 are therefore both consistent with dextral strike-slip faults, although other motions cannot be ruled out based solely on the basement topography. These faults could be portions of the same fault or splays of the same fault system.

Fault 2, also well determined, strikes between north and north-northeast (Figure 2.7) and is in a direction consistent with extensional normal faults in the model of *Rohr and Dietrich* [1992]. If the basement high northwest of Fault 2 has been displaced to the northwest away from the Moresby Ridge by strike-slip motion along Fault 3, then Fault 2 may bound the resulting pull-apart basin (Figure 2.14b). The continuation of Fault 3 to the east of Fault 2 is unconstrained by the refraction data, but the pull-apart model is supported by the depth of basement in the Sockeye E-10 well. Relating Fault 2 to extension is supported by both the half-graben structure in the reflection data and the northwards strike of the features to the southeast of the fault. In any case, Fault 2 is clearly related to Fault 3. Fault 1 strikes north-northeast and bounds the southeastern side of the stable Moresby Ridge (Figure 2.7). It is imaged clearly in the reflection data (Figure 2.10a) and has been interpreted by *Rohr and Dietrich* [1992] as a simple extensional fault bounding a large half-graben.

All of the interpreted faults are consistent with the distributed strike-slip model of *Rohr and Dietrich* [1992]. The complex topography across Fault 4 and in the system of Faults 2 and 3, the small size of the subbasins, and the large vertical relief throughout the basin are difficult to explain using large scale flexural models [e.g., *Yorath and Hyndman* 1983], simple extensional models [e.g., *Thompson et al.* 1991], vertical block faulting models [e.g., *Lyatsky* 1991], or oblique rifting models [e.g., *Hyndman and Hamilton* 1991, 1993; *Souther and Jessop* 1991].

2.3.6 Conclusions

The 3d structure of a portion of the Queen Charlotte Basin beneath western Hecate Strait has been mapped using densely sampled broadside seismic refraction data. The resulting map of depth to the sedimentary basement shows that the thickness of the basin varies rapidly between ~ 200 m and ~ 6 km in a series of fault-bound subbasins. The true strike and dip of features are mapped out of the planes of the 2d seismic reflection sections, aiding in the interpretation of these data. The model is consistent with the seismic reflection and potential field data sets.

In the region offshore of the central QC Islands, a thick sequence of interbedded sediments and volcanics is interpreted to underlie the purely sedimentary section of the Tertiary basin. Four major fault scarps on the basement are also mapped in the model, each with a vertical relief of at least 2 km. Two of these faults are constrained to strike approximately northwest. This direction is consistent with the predicted orientation of strike-slip faults in a tectonic model for basin formation that involves distributed strike-slip shear [*Rohr and Dietrich 1992*]. The topography across both of the faults is consistent with dextral strike-slip motion and, for at least one of them, would be difficult to explain with other motions. The other two faults strike north-northeast and are interpreted as extensional faults. The topography across the faults and the general complexity of the basement topography provide additional evidence in support of the distributed strike-slip model for basin formation [*Rohr and Dietrich 1992*], but are difficult to interpret using other proposed models which would result in simpler dip-slip structures.

3 MODELLING THE CRUSTAL VELOCITY STRUCTURE

3.1 Introduction

The derivation in Chapter 2 of the velocity structure of the basin near the shots allows the interpretation of the 3d refraction data to determine crustal velocity structure. The data set is large, 3d, and densely sampled (Figure 1.3), and would be extremely difficult to model using trial-and-error forward modelling techniques. A 3d tomographic inversion algorithm is developed with the goal of minimizing the computational costs while allowing the velocity model to be densely sampled and to contain arbitrarily large velocity variations. Because the geometry of the QC survey is not ideal for tomographic inversion, a synthetic data set that is designed to be similar to a recently published marine survey is used to demonstrate the procedure. The tomography algorithm is then applied to the QC broadside refraction data to determine the 3d velocity structure of the crust beneath western Hecate Strait.

3.2 Three-Dimensional Travel Time Tomography

3.2.1 Introduction

Information about the 3d seismic velocity structure of the earth can be obtained through the inversion of seismic travel times. Although the word tomograph means “slice picture” and was adopted by the medical community to describe 2d image reconstruction from line integrals, geophysicists use “seismic tomography” to describe two- and three-dimensional imaging. *Aki et al.* [1977] divides the earth into a number of constant velocity blocks to invert teleseismic travel times. *Thurber* [1983] uses velocities interpolated between regularly spaced grid points to invert local earthquake and explosion source travel times. Other 3d

model parameterizations include those of *Hawley et al.* [1981], *Thomson and Gubbins* [1982], and *Tarantola and Nercessian* [1984]. The development of 2d tomography applied to cross-borehole seismic data has paralleled that of 3d tomography, and the formulation of the problem is very similar [e.g., *Dines and Lytle* 1979; *Wong et al.* 1983; *McMechan* 1983; *Peterson et al.* 1985; *Scales* 1987; *Bregman et al.* 1989].

Most of the 3d tomographic interpretations published to date are limited because of two factors. The first limitation lies in the nonlinearity of the seismic travel time problem. Many tomographic inversion techniques avoid the fact that the raypaths depend on the unknown velocity structure by assuming that the velocity variations are small enough that the raypaths are not significantly affected. This limits the types of real earth structures that can be imaged. Some tomographic techniques account for the nonlinearity by iteratively ray tracing and performing linearized inversions. Unfortunately, both accurate forward modelling (3d two-point ray tracing) and linear inversions are very slow computational processes.

The second limitation is that the computational expenses of tomography limit the spatial resolution of the model. The inversion requires the solution of a system of linear equations that relate the travel times to the model parameters. In order to obtain a model parameterization that is capable of resolving structure illuminated by the data, the matrix inversion becomes computationally very time consuming. Even for the relatively rapid iterative techniques used to solve the system of equations without directly inverting the matrix, this step has proven to be the limiting factor in the resolution of the model. The result is that interpretations of the data are limited by the inversion technique [e.g., *Toomey et al.* 1990].

This section describes a nonlinear tomographic inversion procedure that minimizes the computational costs associated with both forward and inverse modelling, allowing the model to be densely sampled. Data from a synthetic 3d seismic refraction survey are inverted to demonstrate that tomography is capable of providing high-resolution images of structures with large velocity contrasts.

3.2.2 Inversion

The travel time t of a seismic arrival can be written as

$$t = \int_{l[u(\mathbf{r})]} u(\mathbf{r}) dl \quad , \quad (3.1)$$

where $u(\mathbf{r})$ is the slowness, or reciprocal velocity, defined as a function of the 3d position vector \mathbf{r} . The relationship between t and u is nonlinear, as the integral is performed over the raypath $l[u(\mathbf{r})]$, which is dependent upon the slowness. This relationship can be linearized by considering a small perturbation of the slowness about a reference slowness $u_0(\mathbf{r})$. This produces a travel time given by

$$t = \int_{l[u_0(\mathbf{r})+\delta u(\mathbf{r})]} u_0(\mathbf{r}) dl + \int_{l[u_0(\mathbf{r})+\delta u(\mathbf{r})]} \delta u(\mathbf{r}) dl \quad , \quad (3.2)$$

where $\delta u(\mathbf{r})$ is the slowness perturbation. Fermat's principle states that the raypath is stationary with respect to slowness, and therefore the integral over the ray $l[u_0(\mathbf{r})+\delta u(\mathbf{r})]$ can be replaced by the ray $l[u_0(\mathbf{r})]$ in the reference slowness field. The first integral in equation (3.2) becomes t_0 , the travel time in the reference slowness field, and the travel time perturbation can be written as

$$\delta t = t - t_0 = \int_{l[u_0(\mathbf{r})]} \delta u(\mathbf{r}) dl \quad . \quad (3.3)$$

Since the raypath $l[u_0(\mathbf{r})]$ and travel time t_0 can be calculated for the reference slowness model, equation (3.3) is a linear relationship between the travel time residual and slowness perturbation that can be used for inversion.

Since equation (3.3) is a linearization of the nonlinear problem, iterations are required to find a final slowness model. In practice, if the true model is sufficiently close to the starting model that the rays in the starting model are an accurate representation of the true rays, then iterations are unnecessary. This is the case if the true model consists only of small slowness variations from the reference model, but iterations are required to invert for many geological models where arbitrary slowness perturbations can be expected. The magnitude of allowable perturbations decreases as the spatial resolution of the model improves, and the true locations of the rays become more important.

In a linear problem, the data d_i are related to the model $m(\mathbf{r})$ through an integration of the form

$$d_i = \iiint m(\mathbf{r}) g_i(\mathbf{r}) d\mathbf{r} \quad , \quad i = 1 \text{ to } M \quad , \quad (3.4)$$

where the functions $g_i(\mathbf{r})$ are called the data kernels and the integration covers all of the 3d space spanned by the model. In order to perform a linear inversion, the model is parameterized as a series of basis functions $h_j(\mathbf{r})$ by

$$m(\mathbf{r}) = \sum_{j=1}^N \alpha_j h_j(\mathbf{r}) \quad . \quad (3.5)$$

The data are then given by

$$d_i = \sum_{j=1}^N \alpha_j \Gamma_{ij} \quad , \quad (3.6)$$

where

$$\Gamma_{ij} = \iiint h_j(\mathbf{r}) g_i(\mathbf{r}) d\mathbf{r} \quad . \quad (3.7)$$

The problem involves the solution of the system of equations (3.6) to find the unknown parameters α_j .

In tomography, the model is usually defined by a 2d or 3d set of boxes or pixels, and the basis functions are defined to be unity within the boxes and zero outside. In this parameterization, the Γ_{ij} terms are the lengths of the i 'th ray in the j 'th box. This Γ matrix is very large, but sparse. The computational expense of the matrix inversion has been a limiting factor in previous work and has required that the model be coarsely sampled [e.g., *Toomey et al.* 1990; *Thurber* 1983; *Aki et al.* 1977]. Other workers have utilized rapid iterative routines such as the algebraic reconstruction technique (ART), simultaneous iterative reconstruction technique (SIRT), and conjugate gradient methods to solve the system of equations without inverting the matrix [e.g., *Dines and Lytle* 1979; *McMechan* 1983; *Humphreys et al.* 1984; *Nakanishi* 1985; *Ivansson* 1985; *Peterson et al.* 1985; *Scales* 1987], but published models are still limited to a few thousand parameters.

Ivansson [1985] and *Toomey and Foulger* [1989] provide examples which show that an insufficiently dense parameterization can lead to artifacts in the model. *Toomey and Foulger* [1989] conclude that a parameterization with good fidelity, defined as the ability to represent expected structure, is preferable to one that provides high resolution of individual model parameters. The densely parameterized model has a poorer resolution of individual model parameters, but has better spatial resolution and can better outline detailed structure. The optimum parameterization maximizes the number of parameters while minimizing the

number that are poorly sampled. This will be called a well-parameterized model; a coarsely parameterized poor fidelity model will be called underparameterized. If a smooth solution is desired, it is better to explicitly smooth a well-parameterized model than to smooth by underparameterizing. There is therefore motivation for the development of a technique to invert for densely sampled structure while minimizing the computational costs.

Menke [1984] and *Michelena and Harris [1991]* introduce the concept of beams for the parameterization of the travel time tomography problem. They redefine a ray (in two dimensions) as a beam centred on the raypath with amplitude $1/w$ and width w . These beams are used as the data kernels $g_i(\mathbf{r})$ and also as the basis functions $h_j(\mathbf{r})$. The gamma matrix becomes symmetric and very sparse. These beam functions can be extended to three dimensions by defining them to have a cross-sectional area of A and an amplitude of $1/A$. The gamma matrix coefficients then become $1/A^2$ times the volume of overlap of the i 'th and j 'th beams.

Harris et al. [1990] further refine the idea by proposing that the beams be shrunk to zero width. The basis and kernel functions are then linear delta-like functions located along the rays. This can be formalized by defining the kernel and basis functions as

$$g_j(\mathbf{r}) = h_j(\mathbf{r}) = \lim_{A \rightarrow 0} \frac{1}{A} \quad (3.8)$$

within a cross-sectional area A centred on the j 'th ray and equal to zero outside this area. For a linear inversion, setting the basis functions to be the same as the kernel functions produces the smallest model, minimizing the norm of the model. Since the linear model in this case is the slowness perturbation, minimizing the size of the model helps to ensure the validity of the linearization assumption. Since the amplitude of the basis functions approaches infinity

and the model should be finite, the α_j terms should go to zero proportional to A . As A approaches zero, then

$$\begin{aligned} A\Gamma_{ij} &\rightarrow l_j & i = j \\ A\Gamma_{ij} &\propto \sqrt{A} \rightarrow 0 & i \neq j \end{aligned} \quad , \quad (3.9)$$

where l_j is the total length of the j 'th ray. Thus the choice of basis functions diagonalizes the gamma matrix. This has the advantage that the solution of the system of equations (3.6) is trivial. The parameters are found using

$$\alpha_j = \frac{A\delta t_j}{l_j} \quad , \quad (3.10)$$

where δt_j is the travel time residual for the j 'th ray. The value of α_j/A can be found while the ray is being traced. The slowness perturbation model is given by

$$\delta u(\mathbf{r}) = \sum_{j=1}^M \frac{\delta t_j}{l_j} Ag_j(\mathbf{r}) \quad . \quad (3.11)$$

Since the kernel functions have amplitude $1/A$, the model is finite.

The product $Ag_j(\mathbf{r})$ equals unity along the j 'th ray and is equal to zero elsewhere. The model $\delta u(\mathbf{r})$ is thus defined only on the infinitesimally thin rays and is unconstrained between rays. If \mathbf{r} lies exactly on a ray, the model takes on a value; otherwise it is entirely unconstrained by the data and takes on a value of zero. A discontinuous, infinitesimally thin solution of this type is difficult to display or interpret and cannot be used for forward modelling. Since the model is strictly unconstrained between the rays, the solution may be extrapolated freely to fill this space. This space may be viewed as an annihilator Hilbert space in the linear inversion problem because the value of the model between the rays has no effect on the measured data. In reality, however, the inversion problem has been linearized and assumes a stability of the rays' positions. In order to maintain the validity of this assumption,

the best way to define the unconstrained part of the model is to smoothly interpolate between the rays. The interpolated model still matches the data but is no longer the smallest model. In regions where rays nearly intersect, the model can also be spatially smoothed. The smoothed model is only an approximate solution, but the smoothing helps to ensure the validity of the linearization assumption. The interpolation can be performed by attempting to match any continuous or discretized function to $\delta u(\mathbf{r})$ as defined by equation (3.11), but ultimately the function should be in a form that can be used in a forward modelling routine.

The slowness perturbation model of equation (3.11) solves the linear inversion problem of equation (3.3). Since equation (3.3) is a linearized version of the true nonlinear travel time tomography problem, iterations are required. The slowness model is updated by the addition of the model perturbation and is then used as the new reference model for another linearized inversion. Iterations are stopped when some criterion indicates that the data have been satisfied.

3.2.3 Resolution

In any inversion problem, a measure of the resolution of the model is desired. *Chou and Booker [1979]* and *Tarantola and Nercessian [1984]* use and extend generalized inversion techniques to invert travel time data, determining a velocity model in the form of a continuous function. For each point in the model, their analyses provide a resolving kernel that represents the averaging window over which the model value at that point has been determined. In this study, only the resolution of the linearized problem will be considered. The resolution of the nonlinear problem must be inferred from these results.

Menke [1984] uses generalized linear inversion appraisal techniques to find the best estimate of the model at a point \mathbf{r}_0 as a weighted average of the true model given by

$$\langle m(\mathbf{r}_0) \rangle = \iiint R(\mathbf{r}, \mathbf{r}_0) m(\mathbf{r}) d\mathbf{r} \quad . \quad (3.12)$$

The function $R(\mathbf{r}, \mathbf{r}_0)$ is a resolving kernel that is desired to be large only near the point \mathbf{r}_0 . The resolving kernel is defined to be a linear combination of the data kernel functions so that the model estimate is determined from a linear combination of the data. The continuous function defined by evaluating the model estimate at all positions \mathbf{r}_0 does not necessarily match the data. *Menke* [1984] determines the resolving kernel by minimizing a spread criterion

$$\iiint |\mathbf{r} - \mathbf{r}_0|^2 R^2(\mathbf{r}, \mathbf{r}_0) d\mathbf{r} \quad , \quad (3.13)$$

subject to a unimodular constraint. This leads to

$$R(\mathbf{r}, \mathbf{r}_0) = \frac{1}{\sum_i \sum_j [S^{-1}]_{ij} f_i f_j} \sum_i \sum_j [S^{-1}]_{ij} f_i g_j(\mathbf{r}) \quad , \quad (3.14)$$

where

$$S_{ij}(\mathbf{r}_0) = \iiint |\mathbf{r} - \mathbf{r}_0|^2 g_i(\mathbf{r}) g_j(\mathbf{r}) d\mathbf{r} \quad , \quad (3.15)$$

and

$$f_i = \iiint g_i(\mathbf{r}) d\mathbf{r} \quad . \quad (3.16)$$

The resolution kernel is independent of the data values, and depends only on the basis functions $g_i(\mathbf{r})$. The resolution of the survey is thus dependent only on the ray coverage.

Using the definition of basis functions as infinitesimally thin rays, equation (3.14) becomes

$$R(\mathbf{r}, \mathbf{r}_0) = \frac{1}{\sum_i \frac{l_i^2}{D_i}} \sum_i \frac{l_i}{D_i} g_i(\mathbf{r}) \quad , \quad (3.17)$$

where

$$D_i(\mathbf{r}_0) = \int_{l_i} |\mathbf{r} - \mathbf{r}_0|^2 dl \quad . \quad (3.18)$$

The resolution kernel depends upon all rays, with a weighting inversely proportional to a measurement of the distance of the ray from the point \mathbf{r}_0 . The model estimate given by equation (3.12) is affected by all rays, even those that do not travel close to the point of interest. This solution is mathematically valid but gives an average of the model that is smoothed over the entire model volume. A solution that may be more appropriate can be found by replacing equation (3.13) with some other criterion.

An alternate criterion is one which minimizes the difference between the resolution kernel and a delta function. The spread criterion in equation (3.13) works well for continuous basis functions that are linearly interdependent, but a “deltaness” criterion will be superior when the basis functions are highly independent, such as in the case when they span significantly different portions of \mathbf{r} . Since the rays leave considerable portions of \mathbf{r} untouched by the kernel functions, it is preferable to minimize the difference between the resolution kernel and a box function, $H(\mathbf{r}, \mathbf{r}_0)$ [Chou and Booker 1979]. H is defined to be equal to $1/V$ within a small box of volume V centred at \mathbf{r}_0 and equal to zero elsewhere. Minimizing

$$\iiint [R - H]^2 d\mathbf{r} \quad (3.19)$$

subject to a unimodular constraint leads to

$$R(\mathbf{r}, \mathbf{r}_0) = \frac{1}{\sum_i w_i(\mathbf{r}_0)} \sum_i \frac{w_i(\mathbf{r}_0)}{l_i} g_i(\mathbf{r}) \quad , \quad (3.20)$$

where $w_i(\mathbf{r}_0)$ is the length of the portion of the i 'th ray inside the box defined by H . Only those rays which penetrate the box contribute a nonzero term to the resolution kernel and model estimate. This solution is physically realistic for the linear problem.

An alternate way to approach the resolution problem is to determine the point spread function [e.g., *Humphreys and Clayton* 1988] by perturbing the model at \mathbf{r}_0 , computing synthetic data for this model, and performing an inversion. By perturbing the model in a box defined by H , the linear inversion theory described in the previous section leads directly to a result for δu that is equivalent to R in equation (3.20), but with a different overall amplitude.

The interpretation of equation (3.20) is straightforward. The best estimate of the model at a point \mathbf{r}_0 is derived from an average of the true model along the rays that penetrate a small box centred at \mathbf{r}_0 . The image of an anomaly will thus be smeared along the rays that penetrate the anomaly. This produces the familiar streaking effects common in tomography when the angular ray coverage is nonuniform. Isotropic ray coverage will produce an image that is smeared equally in all directions. Homogeneous ray coverage provides a similar resolution at different locations. Dense ray coverage allows the resolution of spatially smaller anomalies. The ideal survey design is one that combines all three characteristics.

3.2.4 Implementation

The parameterization used for the inversion of a data set does not need to be the same as that used for forward modelling. The linearized travel time inversion described above is independent of the method used to find rays and travel times in the reference media. The model in equation (3.11), the result of the linearized inversion, needs to be transformed into the parameterization that is to be used in subsequent forward modelling steps. This transformation involves fitting $\delta u(\mathbf{r})$ in equation (3.11) to the set of continuous or discretized functions used to define the velocity model. These functions can be layers, large blocks,

small pixels, polygons, splines, spatial Fourier functions, or even specific geological models such as dipping slabs.

The 3d finite difference travel time algorithm described in Section 1.4 is used to compute first arrival travel times. The inversion results of equation (3.11) need to be gridded to transform them into the parameterization used in the forward modelling algorithm. One or more rays (basis functions $g_i(\mathbf{r})$) may pass through a given grid cell, each with a model value

$$\delta u_i = \frac{\delta t_i}{l_i} \quad (3.21)$$

that could be applied to the cell. The volume of intersection of these rays is zero, so the individual δu_i values should not be added. In order to obtain a single slowness perturbation value for the cell, some sort of average of the values should be used. An arithmetic mean was chosen for computational simplicity, although an average weighted by w_i , the length of the ray in the cell, may be more appropriate. Since the forward modelling routine parameterizes the model at grid points, the value of the model at each grid point is found by taking the average of all the δu_i terms in each of the eight grid cells surrounding the grid point. This gridding process not only interpolates the model between the rays but also performs a smoothing operation. Additional smoothing is optionally applied using a 3d moving average filter. The linearization in the inversion process assumes a stability of the ray locations and assumes that the slowness perturbation model is small. The smoothing operations decrease the magnitude of the slowness perturbation and spread it over a wider area and thus assist in assuring that the linearization assumptions are valid. The smoothing also decreases spatial resolution, but an appropriate choice of the grid sampling interval and moving average filter can ensure that the inversion remains well parameterized.

As each ray is found, a record is kept of the cells through which it travels and its length is computed. The value of δu_i is then added to the elements of an array that correspond to the cells through which the ray travelled, and a count is kept in another array of how many rays penetrate each cell. These two arrays are accumulated for rays for all shot to receiver pairs. Once all rays have been traced, the two arrays are used to find the slowness perturbation at the grid points. The moving average filter is applied if desired, and the slowness perturbation model is added to the velocity model.

The updated velocity model is optionally inspected and is then used to start the next iteration. During the forward modelling step, the travel time residuals are computed. The root-mean-square (rms) travel time residual from the previous model is used as a criterion to determine when to stop iterating. A better, but computationally expensive, method of determining the optimum number of iterations is described by *Peterson and Davey* [1991].

Since the model is parameterized at the grid points, the resolution of the linear problem at a grid point is desired. The slowness within each neighbouring grid cell is affected by 1/8 of the value at the grid point. The resolution at the grid point is therefore found using equation (3.20) by defining H over a volume V defined by the eight neighbouring grid cells. The resolution term due to a single ray,

$$R_i = \frac{w_i}{l_i} \quad , \quad (3.22)$$

is added to the total resolution in the same manner as δu_i . Rays that do not touch H must be traced as they provide constraints of $R_i = 0$. The resulting resolution function has been averaged over a cell and is thus not an exact representation of equation (3.20). It is, however,

a useful representation, as it turns out to be equivalent to the point spread function for the grid point of interest when imaged using the above tomography procedure.

3.2.5 Backprojection Tomography

The linearized inversion procedure described in the previous sections results in a model defined at each grid point by

$$\delta u(\text{grid point}) = \frac{1}{K} \sum_{k=1}^K \frac{\delta t_k}{l_k} \quad , \quad (3.23)$$

where the sum is over those rays that penetrate any of the neighbouring grid cells. This formula is equivalent to simple backprojection tomography [e.g., *Dines and Lytle 1979; Humphreys and Clayton 1988*]. The solution is known to produce an image with significant smearing along the rays.

Equation (3.23) has been derived by gridding the linearized inversion solution in equation (3.11). Equation (3.11) is a continuous (zero pixel size) version of backprojection that exactly solves the linearized inversion problem. An alternate forward modelling algorithm could have been used, parameterizing the velocity model in some manner other than rectangular cells. The transformation of equation (3.11) to the forward modelling parameterization could have resulted in a solution that was significantly different in form from equation (3.23). This alternate solution would also be a form of backprojection.

When pixels are used as the basis functions $h_j(\mathbf{r})$ in equation (3.5), the large sparse system of equations (3.6) can be solved using the algebraic reconstruction technique (ART) or simultaneous iterative reconstruction technique (SIRT). These techniques are considerably faster than matrix inversion. For pixel tomography, both of these techniques

use backprojection in an iterative manner to solve the system of equations. This requires storing the nonzero coefficients of Γ_{ij} and performing many iterations, each equivalent to a single backprojection. Equation (3.23) is most similar to SIRT in the sense that it updates the model simultaneously for all rays. The simple ray weighting of $1/l_k$ minimizes the minimax norm of δu for each backprojection [Dines and Lytle 1979].

The analysis leading to equation (3.11) suggests that for nonlinear tomography, where the locations of the rays in the reference model are different from their actual locations, a single backprojection is sufficient to approximately solve the linearized inversion problem. This is particularly true when the grid cells are small. The rays can then be found by forward modelling between each backprojection. This eliminates the need to store Γ_{ij} , reducing the computer memory requirements from those of ART and SIRT. Forward modelling between each backprojection requires more computations than linear tomography but allows the procedure to solve the full nonlinear problem for arbitrary velocity variations.

As stated earlier, the model estimate in equation (3.12) does not necessarily match the data when distributed as a continuous function. Substituting R from equation (3.20) and calculating at all positions yields

$$\langle \delta u(\mathbf{r}) \rangle = \frac{1}{\sum_k w_k(\mathbf{r})} \sum_k w_k(\mathbf{r}) \frac{\delta t_k}{l_k} \quad . \quad (3.24)$$

This is a backprojection solution with a different weighting for each ray. Although equations (3.23) and (3.24) do not solve the linearized problem exactly, they approach the exact solution in equation (3.11) as the cell size shrinks to zero. Either equation could be used for tomography, but equation (3.23) is used for simplicity.

3.2.6 Synthetic Examples

Synthetic seismic refraction surveys are used to test the tomography procedure. Such a survey requires a large number of shots and receivers on the surface in order to record arrivals at a large range of offsets, azimuths, and positions. Real surveys of this type are rare, largely because of limitations due to cost, number of seismographs, and available interpretation techniques. One such survey is described by *Toomey et al.* [1990]. This marine survey was carried out by firing an airgun over a 2d grid, recorded by several ocean bottom seismographs. The objective was to define a possible magma chamber or zone of partial melt beneath the East Pacific Rise, an ocean spreading ridge. The tomography results described by *Toomey et al.* [1990] used the inversion technique of *Thurber* [1983] and are excellent but are underparameterized by the procedure used.

The synthetic survey of Figure 3.1 is designed to be similar to that of *Toomey et al.* [1990], with the shots and receivers reversed and the ocean water layer removed. Bathymetry could have been included by placing the shots and receivers at appropriate depths within the model, but for simplicity they are all placed at zero depth. A 1d velocity model for the oceanic crust is used as a background model (Figure 3.2). A low velocity anomaly is added to the background model as shown in Figures 3.2 and 3.3. This anomaly is designed to simulate an axial low velocity zone at the oceanic spreading ridge, with amplitude variation and spatial offsets along the axis of the ridge. The anomalous values are large (up to -1.5 km/s) and will obviously cause ray bending. This means that a linear inversion is insufficient and that iteration is required. The spatial sampling interval is 200 m, creating a velocity model that is $101 \times 101 \times 28$ grid points in size. Synthetic data for this model are computed using the

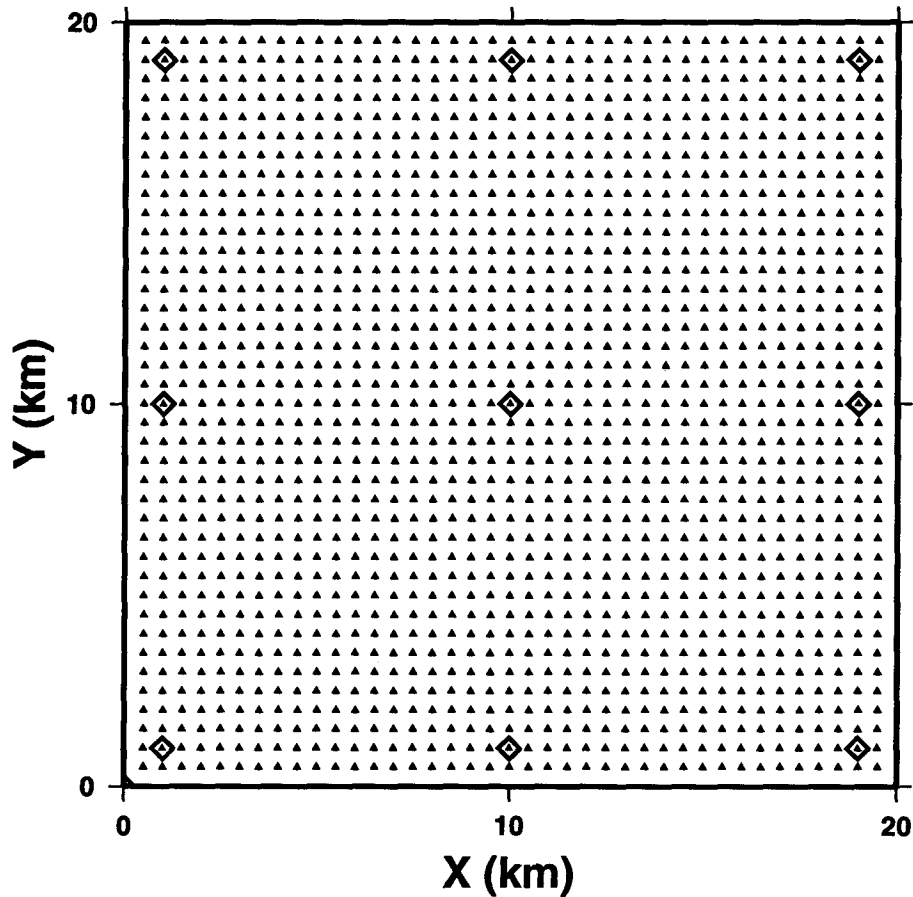


Figure 3.1 Map of synthetic seismic refraction survey designed to be similar to the geometry of the survey of *Toomey et al.* [1990]. Diamonds indicate shotpoints; triangles indicate receiver positions at 500 m intervals. Shots and receivers are located at the depth $Z = 0$.

finite difference travel time algorithm. Because this algorithm may encounter difficulties for shots on the boundaries of the model, two layers of grid values (400 m) are extrapolated above zero depth. The computed travel time data are shown in Figure 3.4.

The 1d background velocity structure is used as the starting velocity model. The inversion results are shown after 20 iterations in Figure 3.5. A $3 \times 3 \times 3$ -point moving average filter has been applied to the slowness perturbation model at each iteration. The behavior of the rms travel time residual is shown in Figure 3.6. The rms residual has stabilized after about six iterations. The velocity model after six iterations has the same structure as in Figure 3.5 but smaller magnitude. After 20 iterations, the anomalous structure is well defined but of smaller

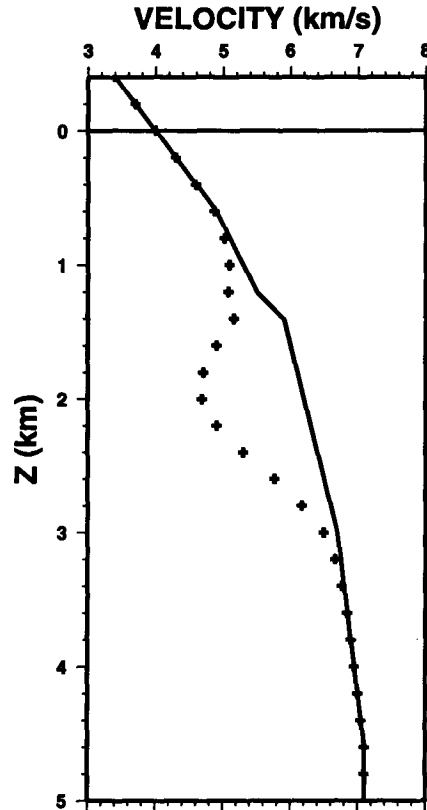


Figure 3.2 Vertical velocity profile through synthetic model. Solid line is the 1d ocean crust model used as a background model. A 3d low velocity anomaly is added to this background structure. Symbols indicate velocity values in a vertical profile through the centre of the anomaly at $X = 10$ km, $Y = 10$ km.

amplitude than the real anomaly. This result is common to most tomographic techniques and is due to two factors. A real survey consists of only a finite number of rays, each giving integrated information about the velocity. This means that, without the addition of outside constraints, the best image of the velocity structure is a spatially averaged version of the real structure. Peak anomalous values are thus underestimated. Only through the addition of extra nondata constraints, such as those that can result from underparameterization, can the peak values of anomalies be properly estimated or overestimated. There is no evidence in the data that these estimates are better. Without additional geological information, it is generally better to underestimate the amplitude of anomalies, thus providing information

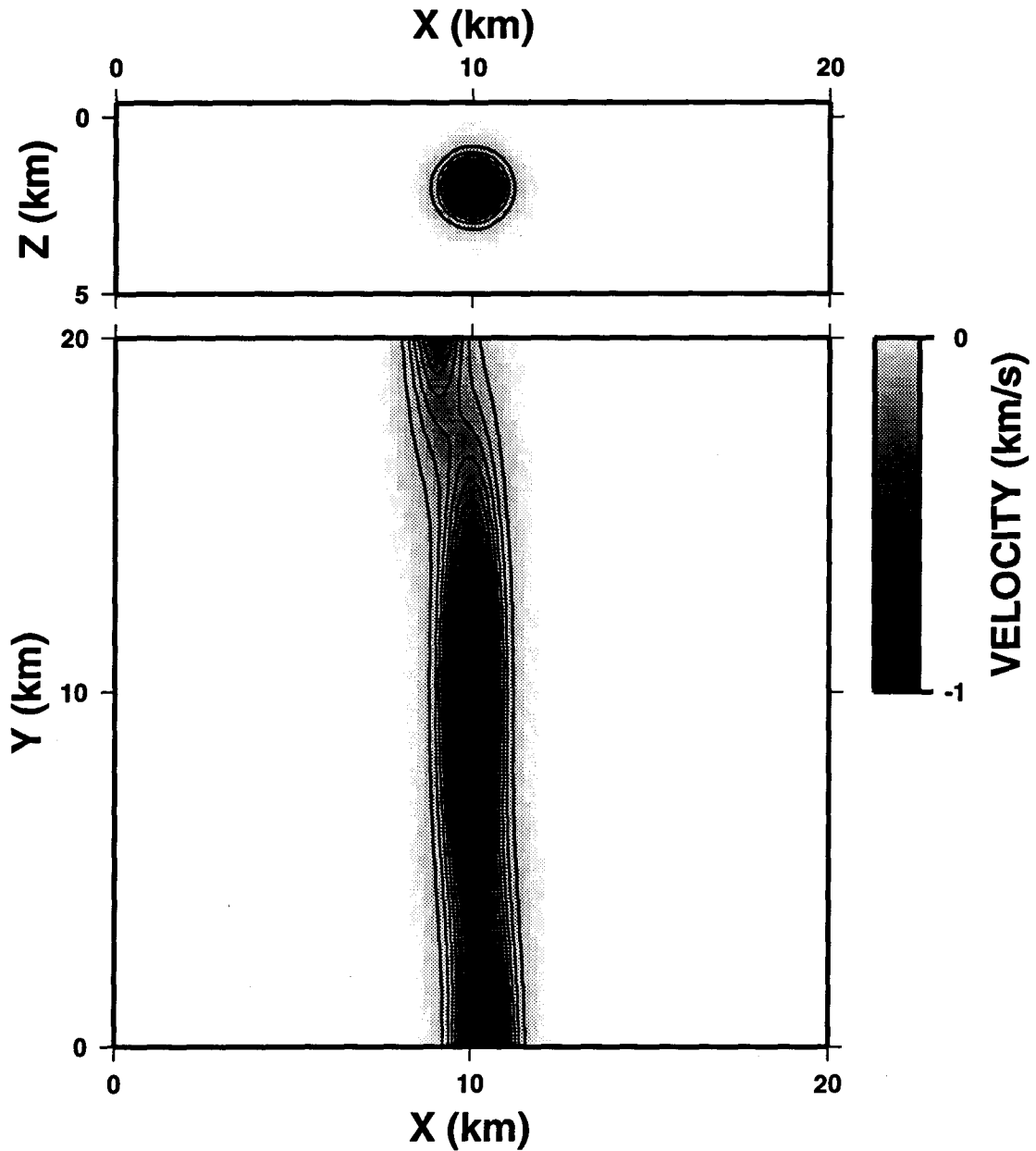


Figure 3.3 2d slices through the 3d synthetic velocity model. The anomaly is intended to simulate an axial low velocity zone at the ocean ridge. The 1d background velocity structure (solid line in Figure 3.2) is subtracted from the model values for plotting. The contour interval is 0.1 km/s, and the grey scale bar is shown. The bottom image is a horizontal slice at depth $Z = 2.0$ km. Above it is a vertical slice at $Y = 10.0$ km. Note that the vertical section crosses through three shotpoints (Figure 3.1).

about minimum structure. The second reason that the anomaly in Figure 3.5 is underestimated is that it is due to a low velocity zone. Rays diffract away from the centre of a low velocity zone, and therefore the peak value is very poorly sampled and is underestimated.

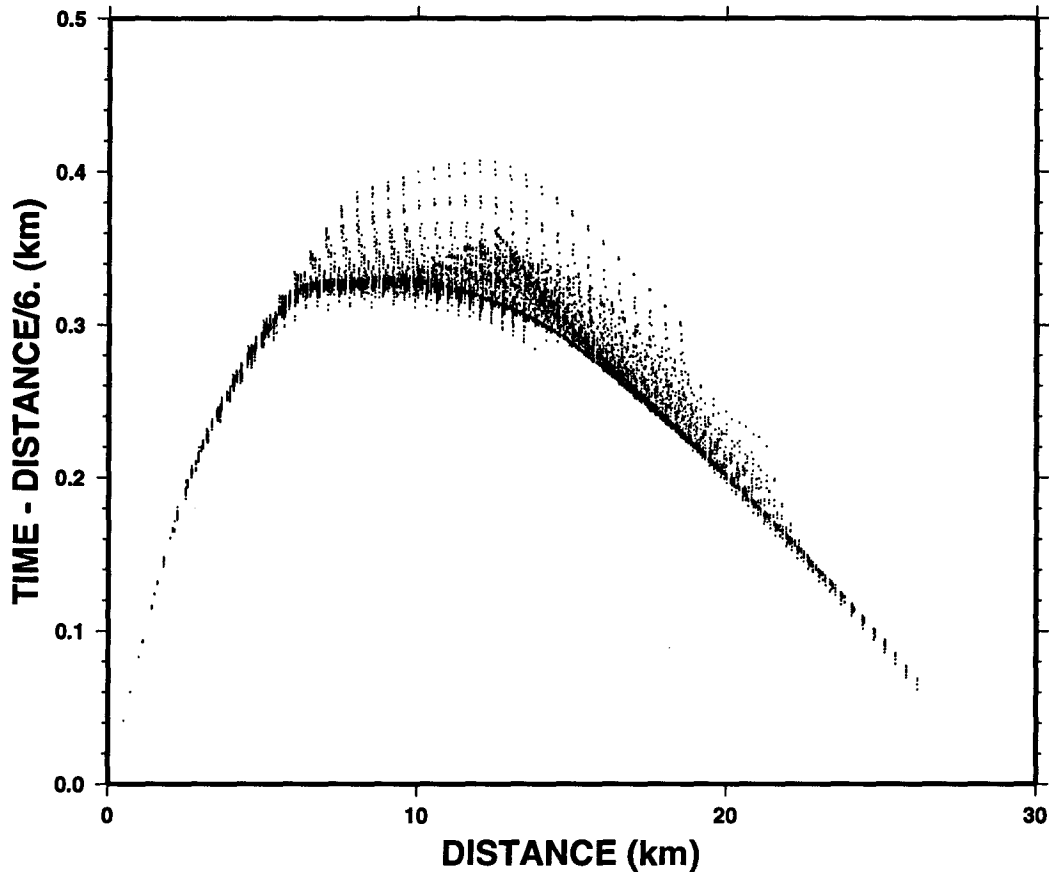


Figure 3.4 First arrival travel times for the low velocity anomaly model of Figure 3.3. The reducing velocity is 6.0 km/s. Note the scatter of first arrival times due to the velocity anomaly.

To determine the response of the technique to noisy data, synthetic data are computed for a model without the low velocity zone, and random Gaussian uncorrelated noise of standard deviation $\sigma = 0.010$ s is added to the data (Figure 3.7). This amount of noise is similar in magnitude to the travel time perturbations caused by the low velocity zone. The results of the inversion are shown in Figure 3.8. Except at the locations of the shots, the anomalies are small and have high spatial frequency. The rms residual stays approximately constant (Figure 3.6). This behavior clearly indicates the stability of the technique in the presence of noise.

The same level of noise is then added to the low velocity zone data of Figure 3.4, and these data (Figure 3.9) are inverted to obtain the results in Figure 3.10. The anomaly is

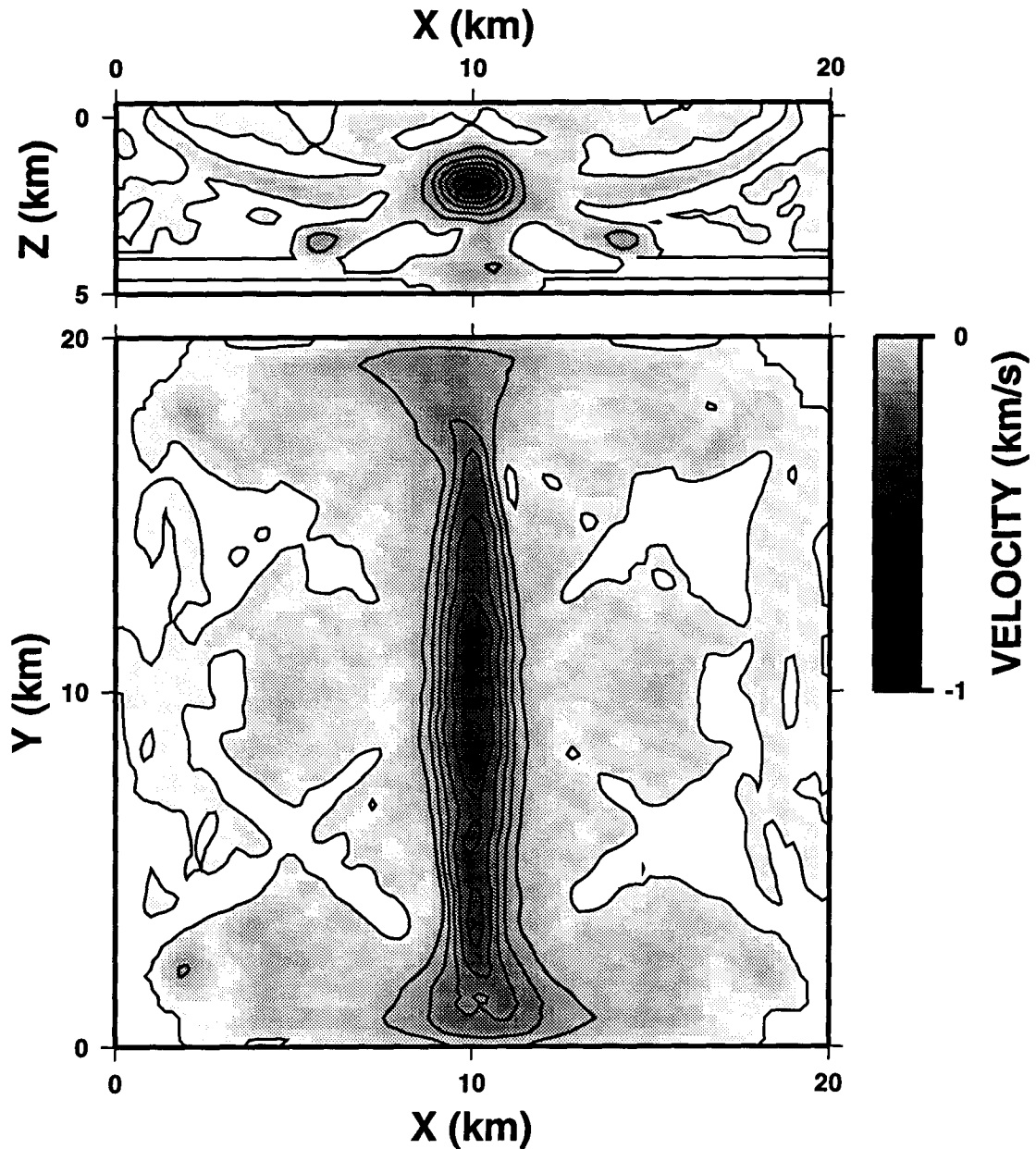


Figure 3.5 Tomography results after 20 iterations from the inversion of the Figure 3.4 travel time data (low velocity anomaly). The starting velocity model is the 1d background model (solid line in Figure 3.2). The images are plotted the same as for Figure 3.3. The low velocity anomaly is well determined.

determined almost as well as it was without noise (Figure 3.5), despite a signal-to-noise ratio near unity. Small background anomalies similar to those in Figure 3.8 are added to the image of the low velocity zone. The rms residual stabilizes rapidly to the level of the noise (Figure 3.6), but the model continues to converge toward the true model. This may indicate that the

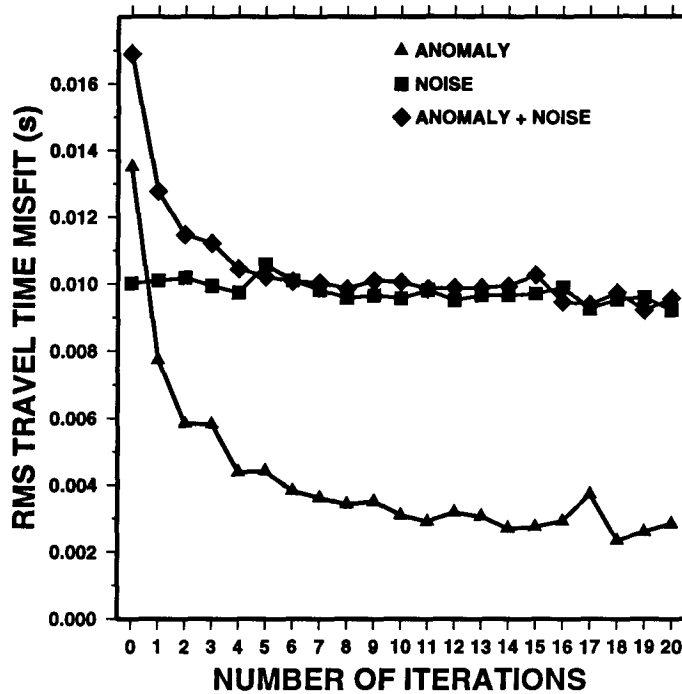


Figure 3.6 The rms travel time residuals plotted against iteration number. Triangles are for the inversion of the Figure 3.4 data (low velocity anomaly), squares are for the Figure 3.7 data ($\sigma = 0.010$ s noise), and diamonds are for the Figure 3.9 data (low velocity anomaly plus $\sigma = 0.010$ s noise).

rms residual is a poor indicator of when to stop iterating [Peterson and Davey 1991].

The resolution of this survey is indicated by the number of rays that penetrate each cell. For a cell far from the edges of the model, one or more rays per shotpoint penetrate each $200 \times 200 \times 200$ m cell (Figure 3.11) and the solution is well parameterized. For a similar data set using matrix inversion tomographic techniques, the model would have to be sampled at about 5 times the grid spacing, or 1 km, due to computational limitations [Toomey et al. 1990]. Since a grid cell of 1 km size is penetrated by at least 20 rays per shotpoint, a solution based on Toomey et al.'s [1990] cell size is underparameterized and cannot show the full level of model detail that the data can provide. A simple analysis of this sort for grid cells at various locations in the model can be used to determine the optimum sampling interval, where the preference would be to maximize the number of grid cells while minimizing the number that are poorly sampled.

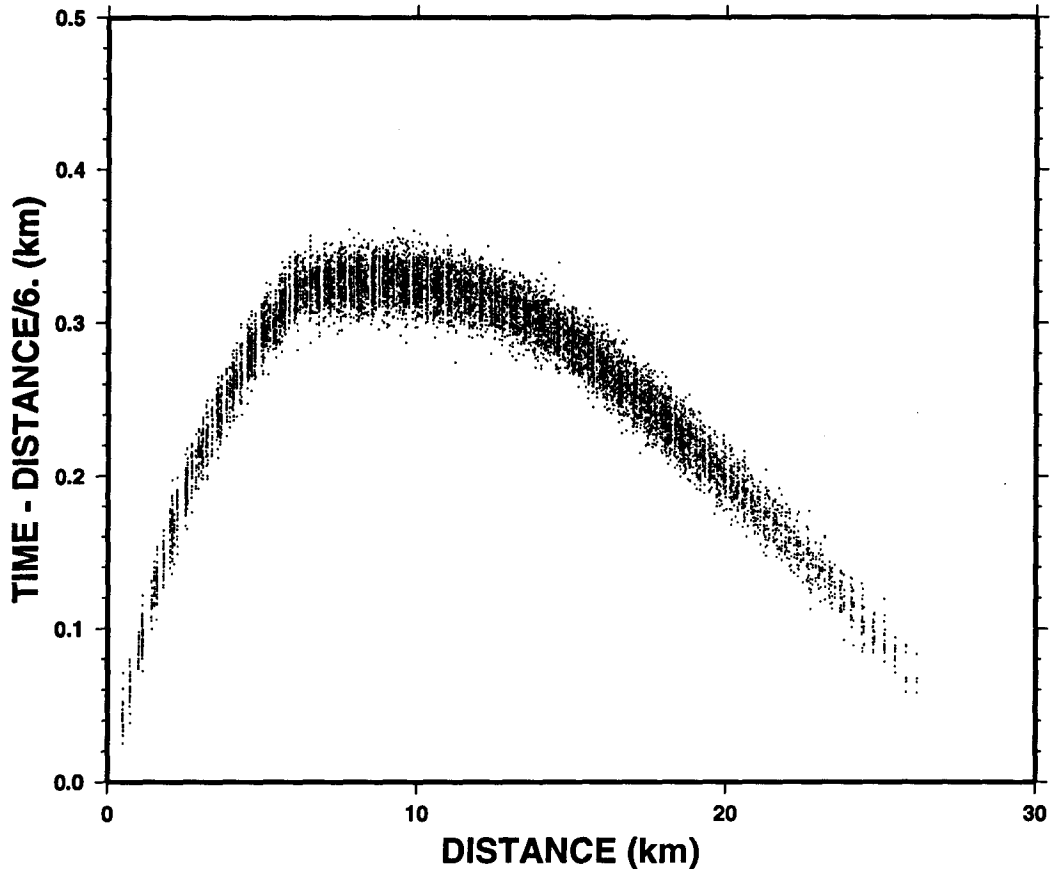


Figure 3.7 First arrival travel times for the 1d background velocity model (solid line in Figure 3.2). Random Gaussian noise of standard deviation $\sigma = 0.010$ s is added to the exact travel time data.

Computing the resolution kernel R , defined by equations (3.20) and (3.22), for a grid point at the centre of the anomaly produces the result shown in Figure 3.12. The resolution is defined for the linearized inversion problem and is computed using the 1d background velocity model (Figure 3.2). The analysis assumes that the raypaths in this model are correct and therefore that the model perturbations are small. As expected, the resolution kernel defines streaks along the rays in three dimensions. Since the upper plot in Figure 3.12 crosses through the grid point of interest and three shotpoints, some of the rays lie within the plane of this section. The inverse weighting of the ray length l_i in equations (3.20) and (3.22) emphasizes the effects of the closer shotpoints relative to those of the more distant shotpoints. The existence of many $R_i=0$ rays throughout the model volume assures that the resolution

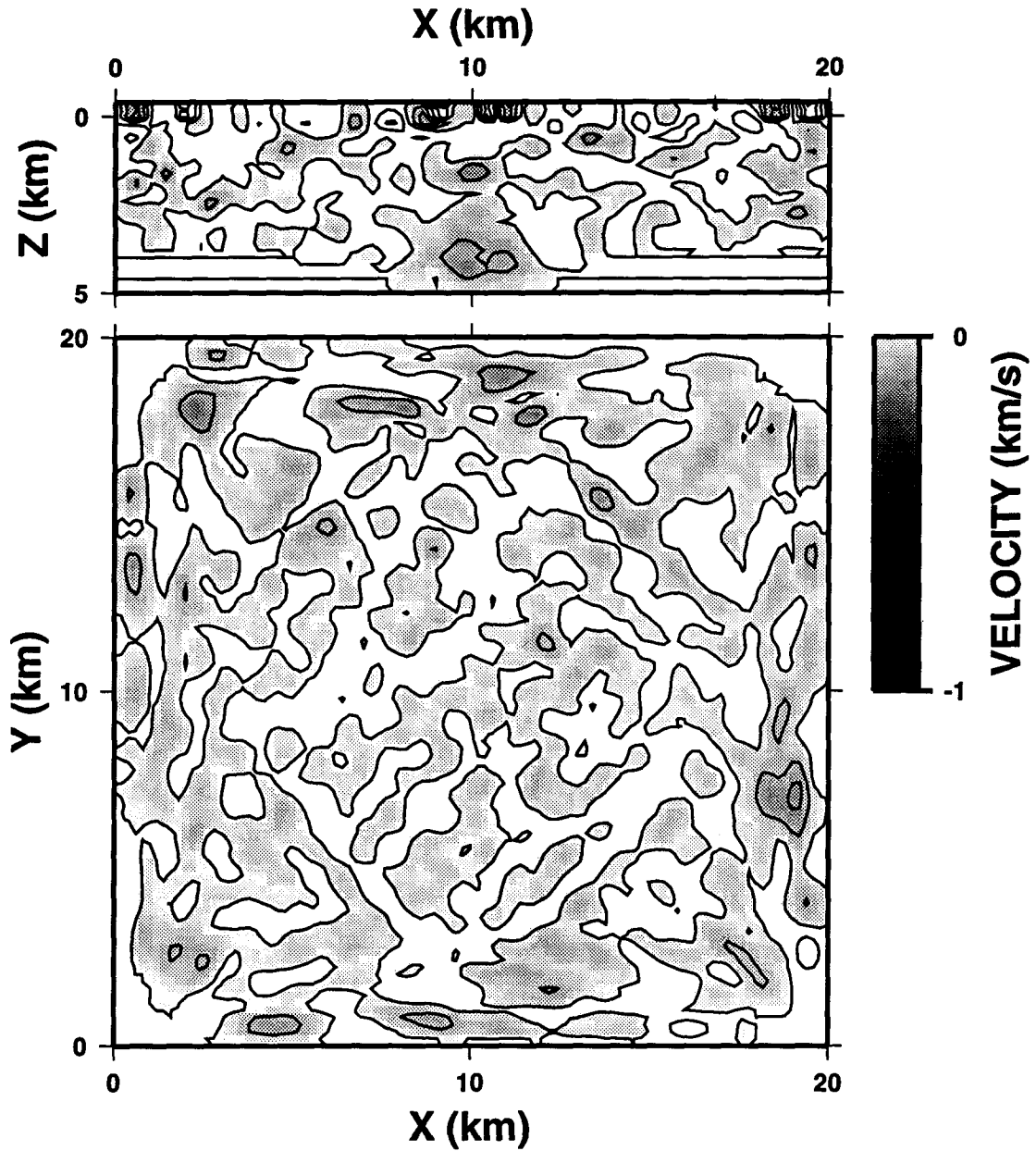


Figure 3.8 Tomography results after 20 iterations from the inversion of the Figure 3.7 travel time data ($\sigma = 0.010$ s noise). The images are plotted the same as for Figure 3.3. The anomalies are small except near the shotpoints in the vertical section.

function is largest at the point of interest. The results of resolution analyses for 3d refraction surveys are directly analogous to those in 2d refraction inversion [e.g., *White 1989a*].

3.2.7 Discussion

The synthetic examples clearly indicate that tomographic inversion is capable of

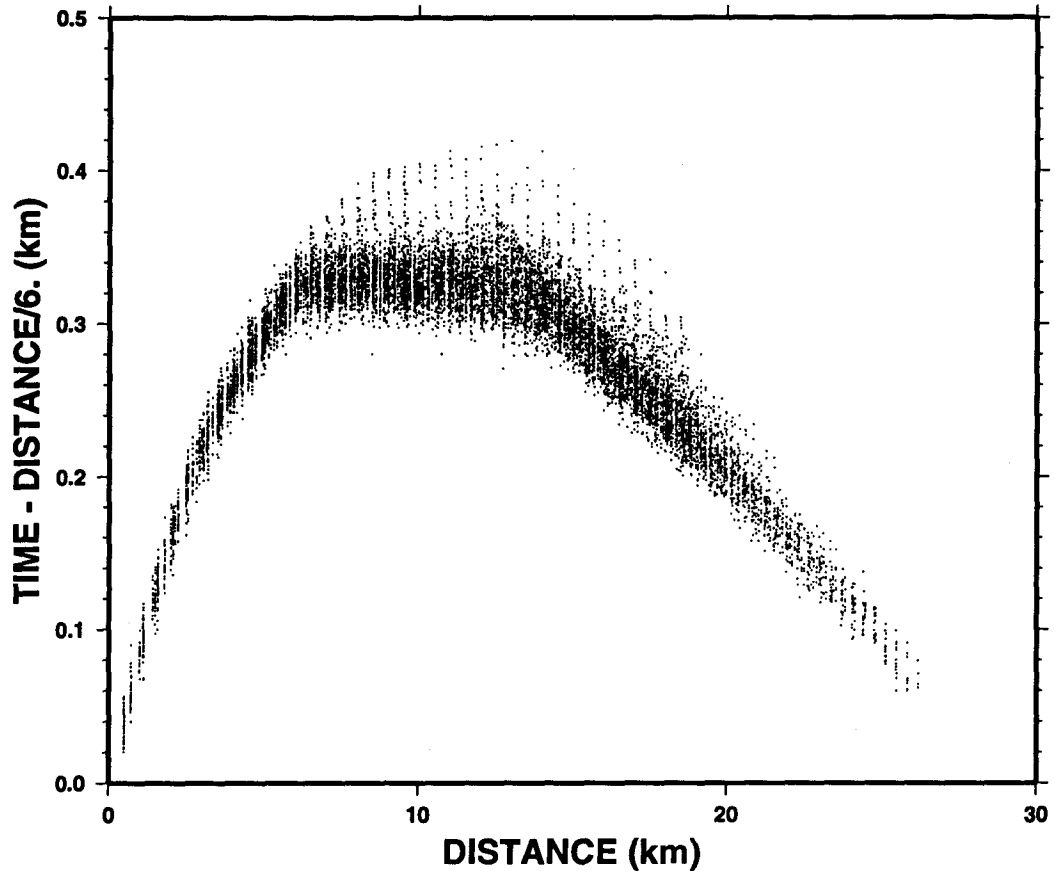


Figure 3.9 First arrival travel times for the low velocity anomaly model of Figure 3.3. Random Gaussian noise of standard deviation $\sigma = 0.010$ s is added to the exact travel time data. providing a highly resolved 3d model from a large number of travel time data. Similar tests were performed for other types of velocity models, including multiple high and low velocity anomalies, layered anomalies, and blocky anomalies. Within the resolution limitations due to the shot and receiver geometries, all of these tests produced good results.

Tests were also performed using a starting velocity model that was not equivalent to the background velocity structure. A time versus offset scatter plot of the picks, such as Figure 3.4, was used to quickly pick a single-valued first arrival curve, which was then converted to a 1d model of velocity versus depth. This type of simple starting model was always sufficient to produce good tomographic images, even for highly 3d velocity structures. The rate of convergence and final model fit were reduced, but the resulting images were always good.

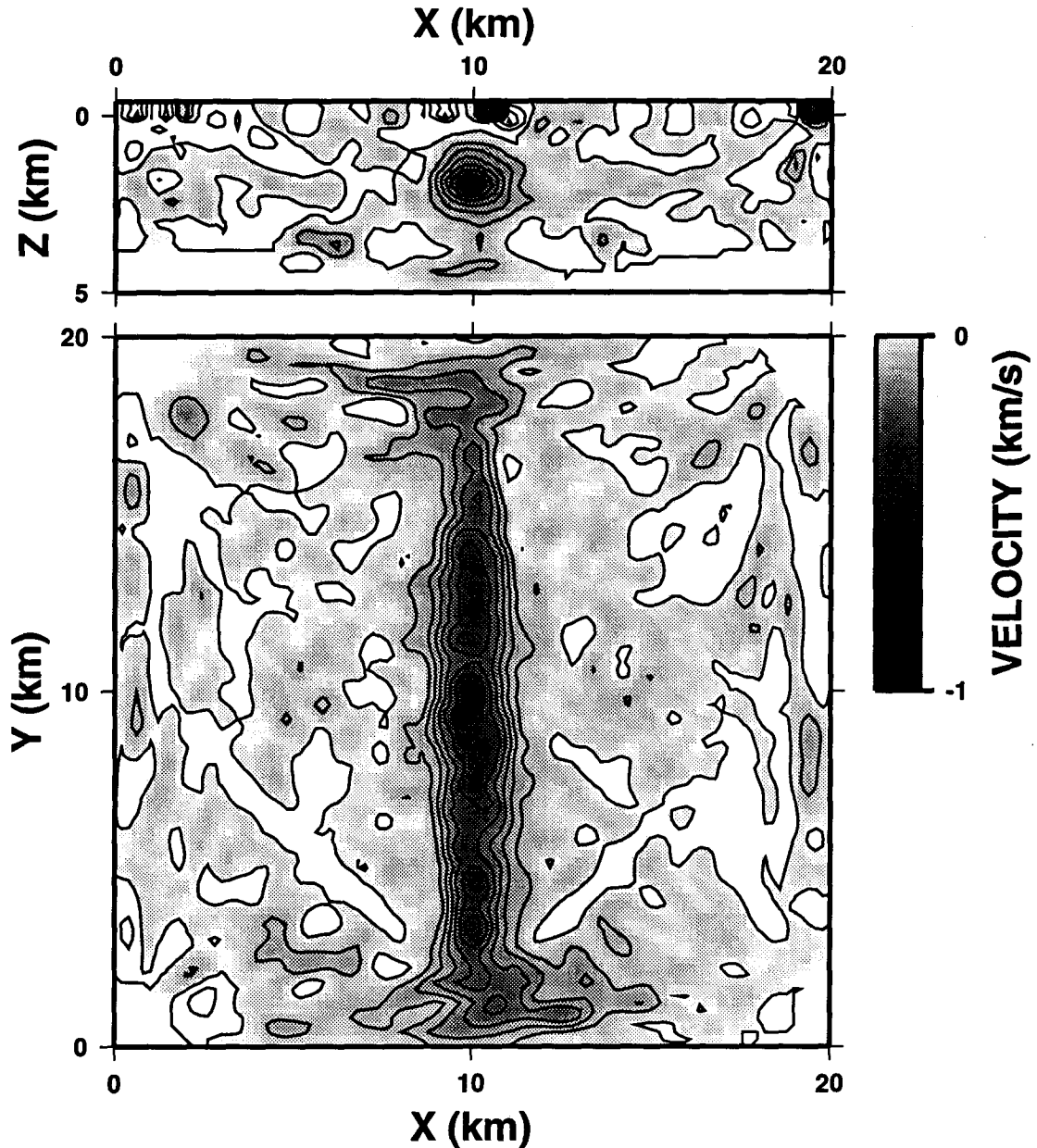


Figure 3.10 Tomography results after 20 iterations from the inversion of the Figure 3.9 travel time data (low velocity anomaly plus $\sigma = 0.010$ s noise). The images are plotted the same as for Figure 3.3. The low velocity anomaly is still well determined.

The computational expenses of 3d tomography are minimized by the choice of efficient forward and inverse modelling schemes. Forward modelling using a finite difference travel time algorithm is accurate and significantly reduces the computation time compared to 3d ray tracing. This allows the rays to be found at each iteration, thereby solving the full

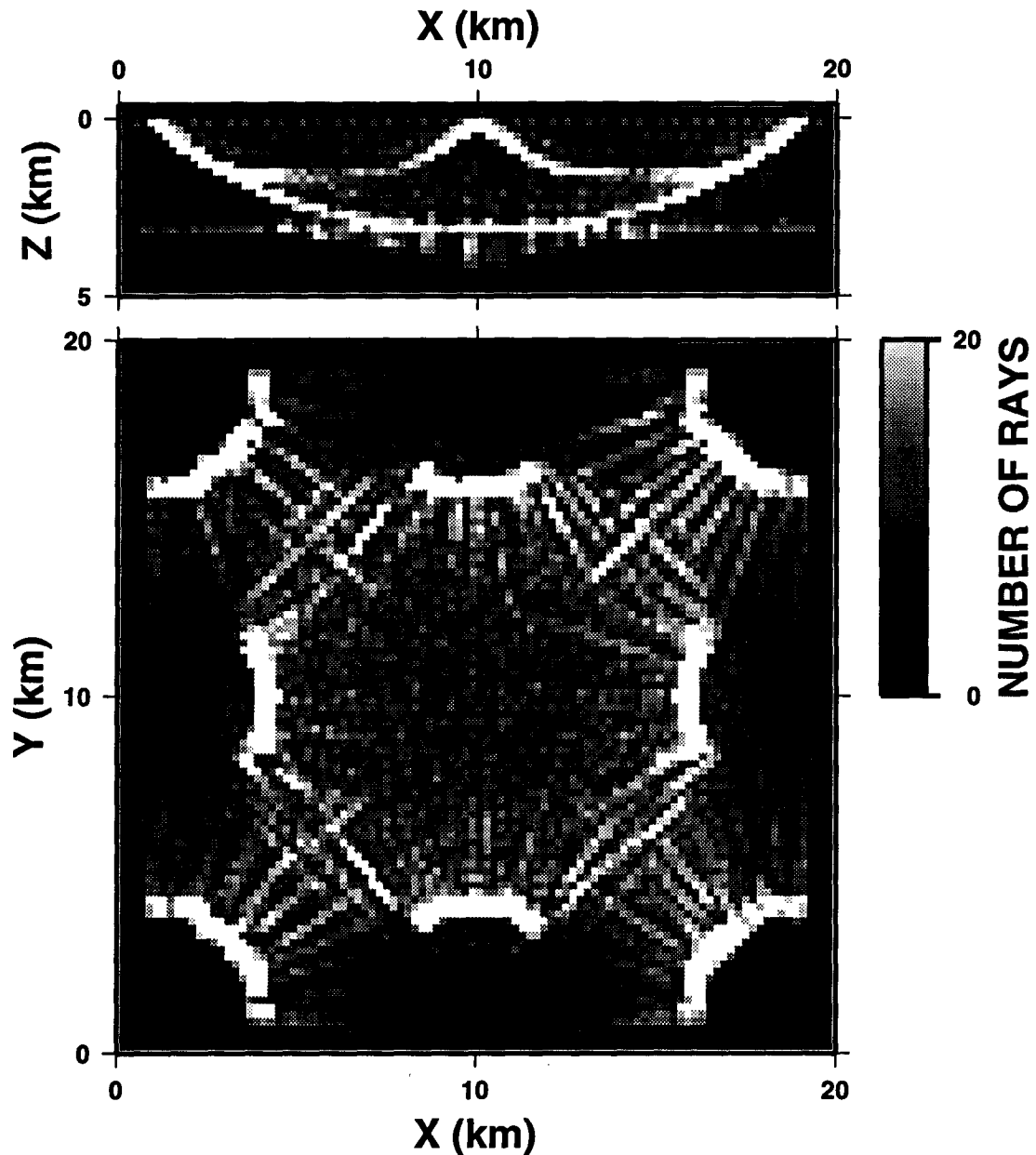


Figure 3.11 Number of rays intersecting each cell is shown by the grey scale. Rays are traced in three dimensions through the 1d background velocity model (solid line in Figure 3.2). The 2d slices are the same as those in Figure 3.3.

nonlinear problem. This is not only important for geological models containing significant velocity variations but also becomes more important as the spatial resolution is improved and relatively small changes in the rays' locations can be resolved. Simple backprojection provides an excellent approximation to the solution of the linearized inverse problem,

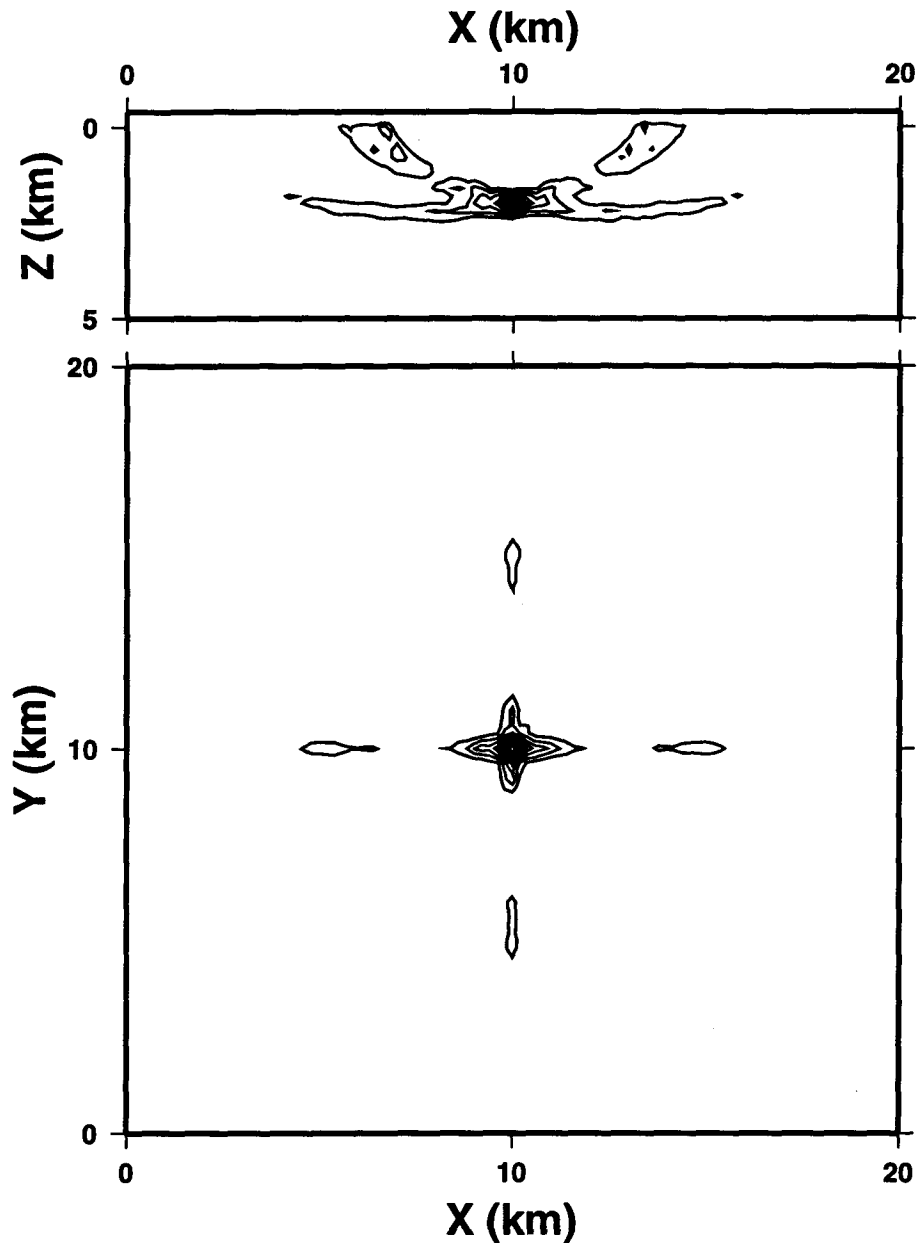


Figure 3.12 Resolution kernel R of equations (3.20) and (3.22) (equivalent to the point spread function) for a grid point at $X = 10.0$ km, $Y = 10.0$ km, $Z = 2.0$ km using the 1d background velocity model (solid line in Figure 3.2). The plot has been normalized so that the value at the point of interest is unity. The contour interval is 0.1. The 2d slices are the same as those in Figure 3.3. Note that the grid point lies on both slices.

particularly for finely sampled models. This reduces the memory storage requirements of the linearized inversion as compared to iterative backprojection or other matrix inversion techniques. Reducing both the computation time and memory requirements of the entire

tomography procedure allows the model to be sampled at a finer spatial resolution. In the synthetic examples, 13,680 travel times (nine shots and 1521 receivers) were inverted for a 3d model consisting of 285,628 grid points and containing large lateral velocity variations. The computation (CPU) time for a single iteration, forward modelling plus backprojection, was about 12 min on a Sun Sparcstation 2. The maximum memory space required was 10 bytes times the number of grid points, or 2.9 Mbytes.

Although discussed and demonstrated here for 3d refraction first arrivals, the tomographic inversion theory is completely general. The rays used in the inversion may be determined by any means, in two or three dimensions. Secondary arrivals may be used. As long as the rays' locations and travel times can be computed by some forward modelling routine, they can be used in the inversion.

The refraction survey geometry discussed here is just one application of 3d tomography. The tomography procedure can be used for local earthquake data (with known source locations) by simply placing the shots within the model. Teleseismic sources can be used if the travel times to all points on the bottom of the model can be found. Given the teleseismic travel times on the bottom face of the model volume, the finite difference algorithm can treat the face as a planar source and propagate times through the volume. In addition, the forward and inverse procedures can be applied to sources and/or receivers beneath the earth's surface in boreholes. This may lead to vertical seismic profiling (VSP) or cross-borehole 3d tomography.

3.2.8 Conclusions

A procedure has been described for the tomographic inversion of 3d travel time data.

Forward and inverse modelling algorithms were chosen to minimize computational costs. Continuous (zero pixel size) backprojection exactly solves the linearized inversion problem and produces the smallest model for the slowness perturbation. Finely sampled (noniterative) backprojection is a good approximation to the exact solution and is sufficient for iterative nonlinear tomography, eliminating the need to store and solve a large system of linear equations. First arrival travel times are forward modelled using a 3d finite difference algorithm that is considerably faster than 3d ray tracing. The computational speed of both the forward and inverse algorithms used in each iteration allows the procedure to correctly account for the rays' locations while producing a model that is densely sampled. The spatial resolution of the final interpretation is then determined from the survey geometry and is not limited by the tomography procedure.

A synthetic 3d seismic refraction survey designed to be similar to a published survey was used to demonstrate the capabilities of 3d seismic tomography. The examples show the successful inversion of a large number of travel time data to find a densely sampled 3d velocity structure with a large velocity contrast. The resolution of the synthetic survey and the stability of the procedure in the presence of data noise are shown.

3.3 Crustal Velocity Model

3.3.1 Introduction

The broadside refraction data provide a dense three-dimensional coverage of the crust beneath western Hecate Strait (Figure 1.3). In this section, these data are interpreted using the tomographic inversion techniques presented in the previous section to obtain the 3d velocity

structure of the upper (<12 km depth) crust. The resulting seismic velocity structures are interpreted in terms of geologic and tectonic models for the region.

3.3.2 Data

The data used in the tomographic inversion are the first arrival travel times, corresponding to raypaths that turn in the upper 12 km of the crust. These travel times are the same as the data used in Chapter 2 to interpret the structure of the QC Basin beneath the shot line. Large and rapid lateral variations in the thickness of the basin cause large relative variations in the first arrival travel times. Before the travel times are inverted for crustal structure, they are corrected for the structure of the sedimentary basin. Using the basin model of Figure 2.7 and the 1d sedimentary and crustal velocity models of Figure 2.6 to compute travel times, the positions of the shots are moved along the raypaths to the basement interface. The travel times are also corrected by the time difference between the ray at the surface and the ray at the basement. In this manner, the portion of the raypath that lies above the already modelled sedimentary basement is removed from the data and the principal reason for the fine model sampling near the shots is removed. The crust can then be modelled using only the coarse (1 km) velocity grid, allowing very rapid forward modelling.

After correction for the QC Basin structure, the shot positions vary rapidly in horizontal position and in depth. This makes it difficult to plot the data. For display purposes only, the data corrections are performed in a different manner. The trace start times are adjusted by the difference in computed travel times between models with and without the sedimentary basin. In this manner, a static shift in time replaces the sedimentary basin with rocks with the 1d crustal velocity structure (solid line in Figure 2.6). Figure 3.13 shows the refraction

data, after these static shifts, for shots along line 4 recorded at receiver sites 13 and 17. Most of the large rapid lateral variations in the first arrival travel times, due to changes in sedimentary thickness, are removed from the data (cf. Figure 1.4).

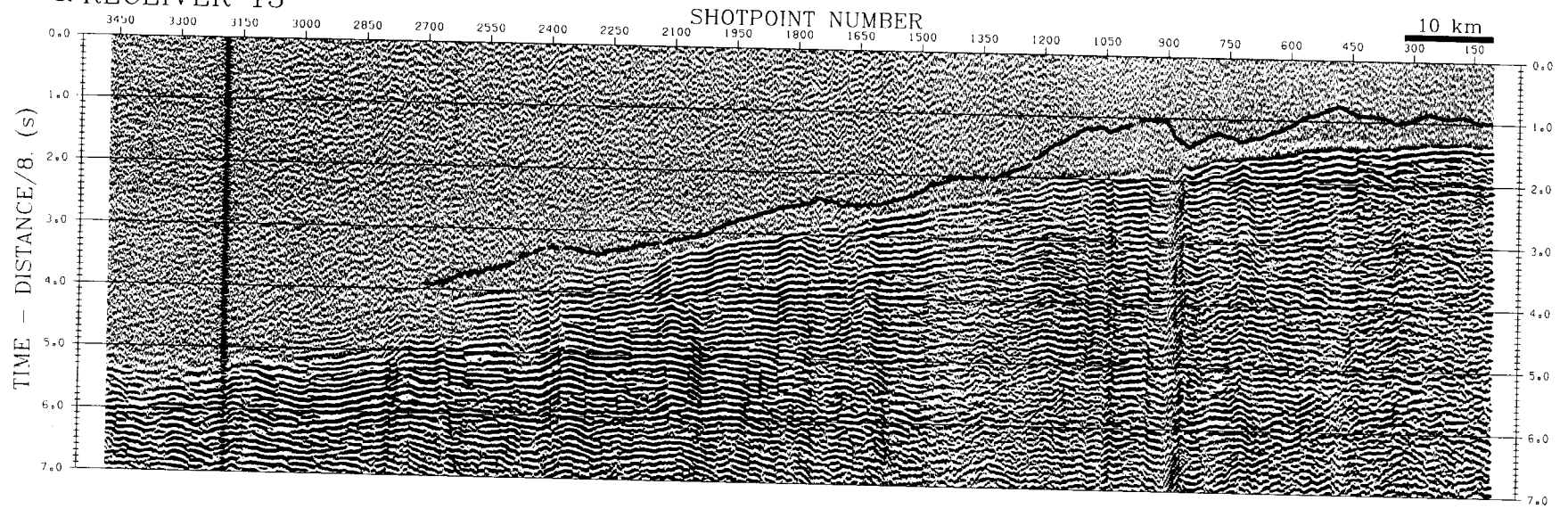
A total of 10081 travel time picks from all shot lines and receivers within the study area of Figure 1.2 are used in the inversion. The accuracy of the picks is excellent, typically within a quarter wavelength or about 25 ms (Topic 2.3.2). The correction for basin structure assumes that the 1d velocity structure of Figure 2.6 is correct. This assumption, possible errors in the sedimentary basin model, and possible systematic picking errors combine to increase the estimate of the errors for the travel time picks to about 50 ms.

3.3.3 Interpretation Method

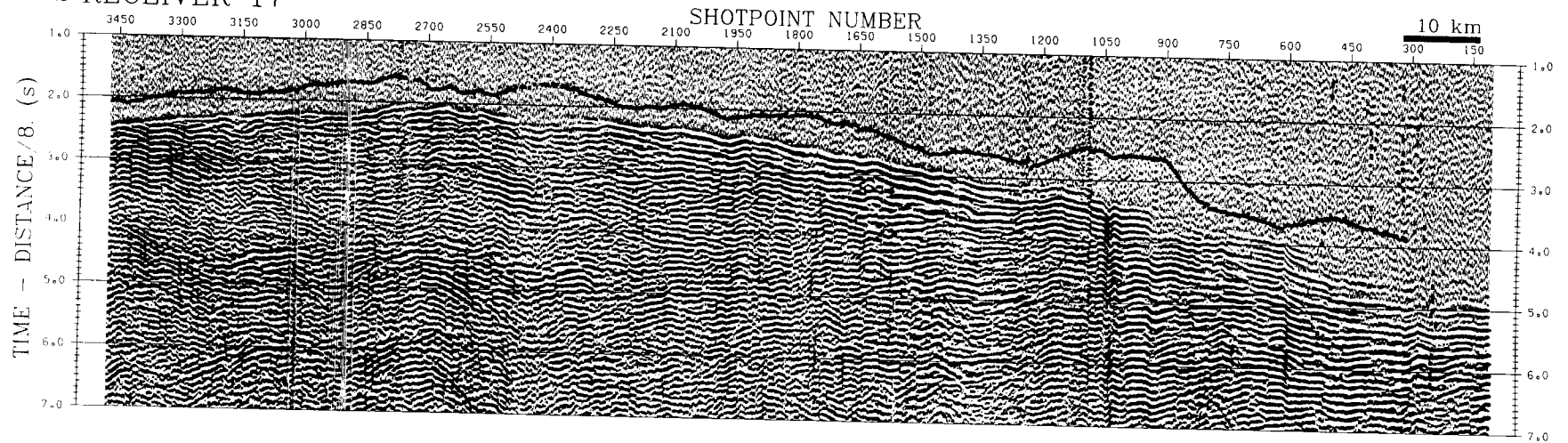
Using the tomography algorithm described in the previous section, the first arrival travel times, corrected as described above, are inverted to determine the 3d upper crustal structure. The crustal velocity model is sampled vertically and horizontally at a 1 km grid spacing. Taking advantage of the reciprocity of travel times, the receiver sites are treated as sources and times are computed throughout the 3d model. Travel times at the shotpoints are determined by tri-linear interpolation within the appropriate grid cell.

Figure 3.13 (next page) Broadside refraction data sections for line 4 recorded at (a) receiver 13 and (b) receiver 17. The traces are plotted against shotpoint number (distance along line 4; Figure 1.2) using a reducing velocity of 8.0 km/s. For receiver 13, shotpoint 101 is at a shot-receiver offset of 27 km and an azimuth of 258°, and shotpoint 3473 is at 151 km and 170°. For receiver 17, shotpoint 101 is at an offset of 132 km and an azimuth of 325°, and shotpoint 3473 is at 43 km and 214° (Figure 1.2). Traces are stacked at every third shotpoint (135 m along line 4) using a linear moveout of 8 km/s, bandpass filtered from 5 to 20 Hz, true amplitude scaled proportional to the shot-receiver offset, and static time shifted to replace the varying sediment thickness of the QC Basin with crustal velocities. The bold lines indicate the travel time picks for these sections before corrections for the basin (cf. Figure 1.4). For illustration purposes only, these lines are shifted 1 s earlier so that they are plotted before the first arrivals. Note that most of the rapid lateral variations in the travel times have been removed by the static corrections.

a RECEIVER 13



b RECEIVER 17



The broadside refraction data provide a dense 3d coverage of the model region, but the ray distribution is highly anisotropic. At a specific point in the 3d model, the rays are often travelling sub-parallel to one another (Figure 1.3). This is not ideal for a tomographic inversion. Isotropic ray coverage ensures that the true location of a velocity anomaly is properly determined, while anisotropic coverage causes the anomaly to be smeared along the dominant raypaths. In order to compensate for this problem, tomographic inversions were performed using several 1d starting models and spatial filters. The final model includes only those features that are well constrained by the data.

The 1d crustal velocity profile shown in Figure 2.6 (solid line) is used as a starting model in the 3d tomographic inversion. This profile represents the average crustal structure for the region and is determined by 1d and 3d analyses. Due to the combined effects of the shot-receiver offsets and the velocity structure, few rays reach their deepest penetration above 4 km depth. Therefore the near-surface velocities are constrained only to match the interval time through this region. A high velocity gradient exists from 4 to 7 km depth. Below 7 km depth, the average 1d velocity becomes nearly constant at 6.5 km/s. Although a very small velocity gradient is indicated in the model, a constant or even low velocity zone could be used. A low velocity zone, however, would require slightly higher velocities at the top of the zone. This region extends to at least 12 km depth as indicated by the lack of higher velocity phases appearing as first arrivals. The crustal velocity below 12 km depth is unconstrained by the first arrival travel times. Although the crust is well sampled in the depth range of 4 to 9 km, the 1d average crustal velocity profile does not produce a good match with the travel time data, indicating the presence of significant lateral variations.

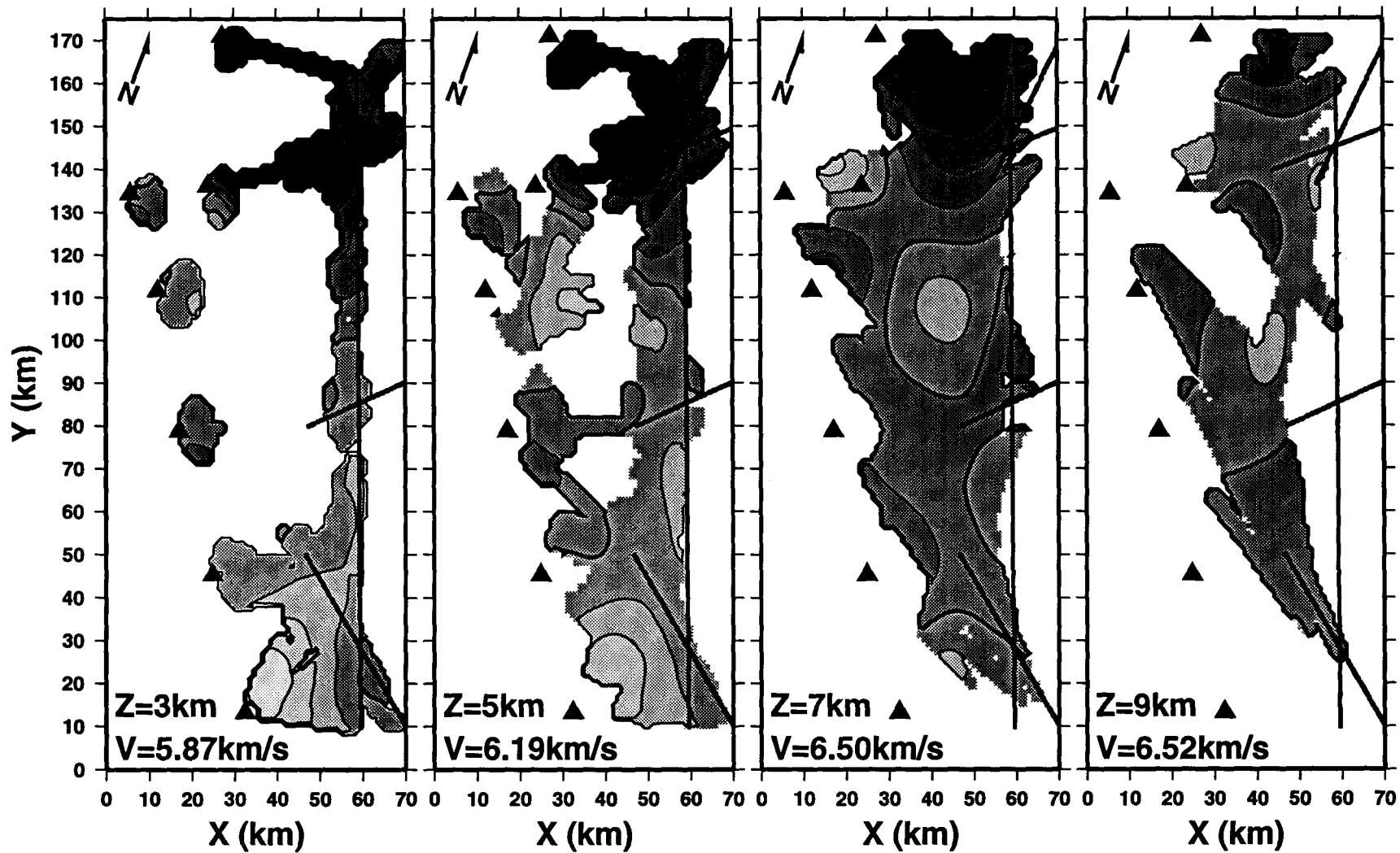
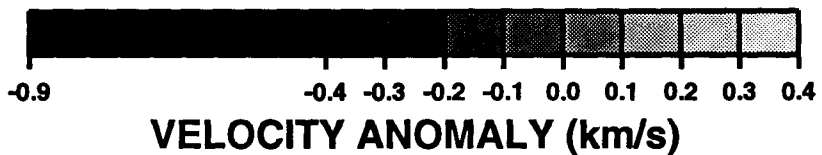
3d spatial filtering of the velocity model is performed at each iteration of the tomography procedure, both to stabilize the algorithm and to produce a model that contains only those large scale features that are considered to be well constrained by the data. Significant experimentation with the smoothing parameters is required due to the anisotropic ray coverage. The final parameters produce a model with only smooth, low spatial frequency anomalies and with a smooth extrapolation into regions of poor or no ray coverage. The size of the filters is chosen such that the final model produces a root-mean-square (rms) data misfit which indicates that the model matches the data within the data error estimates of 50 ms, without over-matching. Smoothing is performed using two different operators at each iteration. In the first smoothing operation, the value of the slowness (inverse velocity) perturbation at each grid point is computed from all rays that penetrate a 20 km by 20 km wide by 2 km deep box centred at the grid point. This ensures that regions of sparse or anisotropic ray coverage are smoothly interpolated or extrapolated from neighbouring rays. After computing the slowness model perturbation at each grid point, the gridded model is then smoothed using a 21 km by 21 km wide by 3 km deep moving average filter. This second filtering operation ensures that the model is smooth and that the model perturbation extrapolates smoothly to zero in regions of no ray coverage. The use of a small spatial sampling interval and large spatial averaging filters is preferable to using a coarse sampling interval. The use of a coarse sampling interval, or large grid cells, confines velocity anomalies to lie within the borders of pre-defined regions and can therefore produce artifacts in the model [Toomey and Foulger 1989].

3.3.4 Results

The final 3d crustal velocity model is shown in Figure 3.14. Although the model extends smoothly into regions of no ray coverage, only those grid points within one kilometre of a ray have been shown to illustrate which portions of the model are constrained. Significant lateral velocity variations are present. Most of the rays travel horizontally at depths between 5 and 9 km depth, so that the model is best constrained in this depth range. The best constrained portions of the model are those more than 10 km horizontally and 1 km vertically from the edge of ray coverage. Small anomalies that extrapolate to their largest value at the edge of coverage (for example the positive anomaly at $X = 20$ km, $Y = 140$ km, and 7 km depth in Figure 3.14) are indicative of real anomalies, but may be over-estimated in amplitude and may be misplaced due to smearing along the direction of dominant ray coverage.

In the horizontal slice through the 3d model at 3 km depth (Figure 3.14), the anomalies near each receiver represent averages of the perturbation required to model the near receiver structure. Since these anomalies are smeared vertically along the raypaths, the value of the anomaly is poorly constrained. Rays at the smallest shot-receiver offsets reach their deepest point at 3 to 5 km depth and indicate that, relative to the 1d average velocities of Figure 2.6, the shallow crustal velocities are significantly lower in the north and are higher in the south. Beneath 5 km depth, the best constrained features of the model are the high velocity zone

Figure 3.14 (next page) Selected 2d slices through the 3d velocity model for the study area of Figure 1.2. Each image is a horizontal slice through the model at the specified depth Z and is an image of the velocity perturbation relative to the specified starting velocity V at that depth (Figure 2.6). The contour interval is 0.1 km/s; the thick contour is zero. Regions with no ray coverage are shown as white, even though the actual velocity model smoothly extrapolates into these regions. The surface locations of the shot lines and receivers are shown for reference as in Figure 1.2.



centred at $Y = 110$ km, the low velocities north of $Y = 130$ km and above 7 km, and the small anomaly values (between -0.1 and 0.1 km/s) throughout much of the rest of the region.

The rms misfit of all first arrival travel times using the 1d starting velocity model is 201 ms. The travel time misfits for shots along line 4 are shown in Figure 3.15a. The rms misfit decreases rapidly during the first 5 iterations, then decreases more slowly during subsequent iterations. The velocity model in Figure 3.14 is the result of 20 iterations and produces an rms misfit of 42 ms. The final misfit is better than the estimate of 50 ms for the travel time errors, but not by enough to indicate that the data have been over-fitted. The final misfits for shots along line 4 are shown in Figure 3.15b.

Although a quantitative measure of the velocity resolution of the model is not produced by the inversion algorithm, a qualitative estimate of resolution is possible from results of the experimentation with different starting models and spatial smoothing operators. In the best constrained regions of the model, more than 10 km horizontally and 1 km vertically from the edges of ray coverage, random travel time errors limit accuracy of the model velocity values to about 0.05 km/s. Systematic sources of error include picking errors, errors in the sedimentary basin corrections and errors due to the anisotropic ray coverage near the edges of the constrained region. These can cause velocity errors as large as 0.2 km/s, but the portions of the model with good ray coverage are probably defined to within 0.1 km/s. Relative differences in velocity between neighbouring regions are probably better resolved. The spatial resolution of the model is constrained by the survey geometry and the smoothing filters. Even the best constrained velocity values must be considered as averages over a volume about 20 km in diameter and 2 km deep.

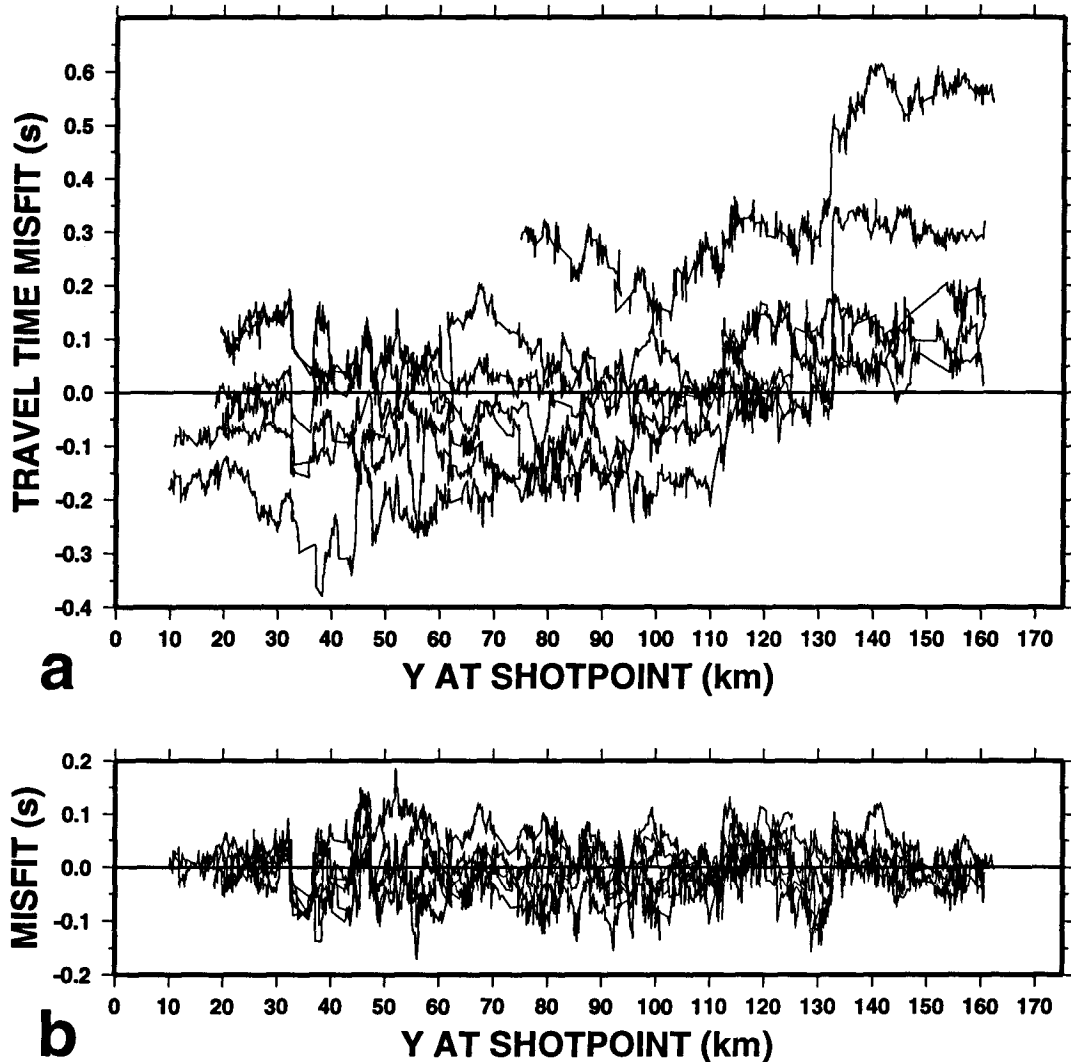


Figure 3.15 Travel time misfits for the line 4 refraction data plotted against the Y location at the shotpoint. Each line represents the misfits for one receiver. (a) The misfits calculated using the 1d starting model of Figure 2.6 (solid line). (b) The misfits computed using the final 3d velocity model (Figure 3.14).

3.3.5 Discussion

The 1d velocity profile (Figure 2.6) is consistent within the constrained depth range with the QC Islands ends of the 2d refraction interpretations of *Yuan et al.* [1992] and *Spence and Asudeh* [1993]. The high velocity gradient zone above 7 km depth is observed in a similar depth range on the 2d interpretations and has been interpreted by both sets of authors to correspond mainly with Tertiary volcanics. Because of the total thickness of

the velocity gradient zone as compared to stratigraphic thicknesses indicated by geological mapping [Lewis *et al.* 1991], it may also include Cretaceous sediments, which Haggart [1991] suggests are thin offshore, and possibly post-Karmutsen Jurassic and Triassic sediments and volcanics of the Wrangellia terrane. The thick zone of constant velocity in the mid-crust is also observed on the 2d interpretations and is attributed to rocks of the Wrangellian terrane and more specifically to the Karmutsen Formation. The thickness (at least 4 km) and homogeneity of the Karmutsen Formation [Sutherland Brown 1968] and observed velocities typical of basaltic composition support this interpretation. Significant lateral velocity variations from the 1d profile indicate large lateral variations in the existence and thickness of the various geological units.

The 3d velocity model (Figure 3.14) indicates that the shallow crustal velocities in the northern part of the study area are 0.3 to 0.8 km/s lower than the average 1d velocity profile. The sediments of the Tertiary QC Basin beneath the shot lines are modelled in Chapter 2 and are accounted for by the shot position and time corrections before the tomographic inversion. Receiver site 18 lies on a small volcanic plug within the QC Basin. A large amplitude low velocity anomaly shallower than 3 km depth near this receiver indicates the presence of the low velocity sediments. The Sandspit Fault bounds the western margin of the QC Basin and strikes northwest only about 5 km east of receiver site 17 (Figure 1.2) [Sutherland Brown 1968; Rohr and Dietrich 1992]. Although poorly constrained by the ray coverage, the shallowest velocity anomalies near this receiver indicate low velocities north and east of the receiver but not beneath it or to the south (Figure 3.14). This is consistent with the low velocities of the Tertiary basin to the east of the Sandspit Fault.

A large region with velocities much lower than the 1d profile exists north of about $Y = 130$ km, east of receiver 17 and above 6 to 7 km depth (Figure 3.14). Chapter 2 models the QC Basin beneath the shots in this region to be 2 to 4 km thick and the travel time data are corrected for the sediments based on this interpretation. Evidence from the reflection data and other sources is used in Chapter 2 to infer a thick sequence of interbedded Tertiary sediments and volcanics beneath the interpreted basement interface in this region. The low velocities observed in the crustal tomography model support this interpretation.

In the southern portion of the study region, the velocities above 5 km depth are higher than average (Figure 3.14). On the QC Islands, the age of the surface rocks increases to the south (Figure 1.2) [Sutherland Brown 1968; Lewis *et al.* 1991]. The higher velocities near the surface at the south end of the islands are probably due to the shallower depths of older rocks.

Velocities exceed 6.6 km/s at 7 km depth in the large anomaly centred at $Y = 110$ km (Figure 3.14). This suggests that the rocks have a more mafic composition than surrounding rocks. The extent of the anomaly is constrained on its northern, southern and western sides by good ray coverage, but the eastern margin of the anomaly may extend beyond line 4. High velocities are present from 5 to 9 km depth, the entire depth range constrained in this region (Figure 3.14), and may continue shallower and deeper. The high velocities could correspond to the deep root of an igneous intrusion. Three plutonic suites are exposed on the QC Islands, including the Tertiary Kano Plutonic Suite (KPS) and the Jurassic Burnaby Island Plutonic Suite (BIPS) along the east coast of the southern islands (Figure 1.2) [Anderson and Reichenbach 1991]. Both suites are variable in composition but are dominated by intermediate composition rocks. Strong positive magnetic anomalies are observed over

plutons of both the BIPS (e.g., near receiver site 14 and southeast of receiver site 17, Figure 3.16) and the KPS and associated volcanic rocks (e.g., between receiver sites 15 and 16, Figure 3.16). A strong magnetic signature is not expected for an offshore pluton because of the masking effect of the overlying sediments. The high velocity anomaly observed at depth is interpreted to be due to the deep root of a BIPS or KPS pluton. Based on the poor spatial correlation, it is possible that the interpreted pluton is part of or associated with the Cumshewa Head pluton southeast of receiver site 17 (Figures 3.16 and 1.2).

3.3.6 Conclusions

3d densely sampled broadside refraction data are used to determine the velocity structure of the crust beneath western Hecate Strait. The average 1d crustal velocity model contains a high velocity gradient to about 7 km depth. This gradient zone is assumed to include Tertiary volcanic rocks, Cretaceous sediments and possibly post-Karmutsen Wrangellian sediments and volcanics. From 7 km to at least 12 km depth, the velocity is approximately constant at 6.5 km/s. This zone is interpreted to be Wrangellian rocks, dominated by the Karmutsen Formation.

The 3d velocity model for the upper crust derived by tomographic inversion contains significant lateral variations. Low velocities in the upper crust east of the central QC Islands are consistent with the interpretation of Chapter 2 of a thick sequence of interbedded sedimentary and volcanic rocks within the deepest part of the QC Basin in this region. High velocities at shallow depths east of the southern QC Islands are probably due to older rocks at shallower depths as mapped onshore. A large high velocity anomaly with velocities of 6.7 km/s at 7 km depth may be due to the deep root of a mafic igneous intrusion.

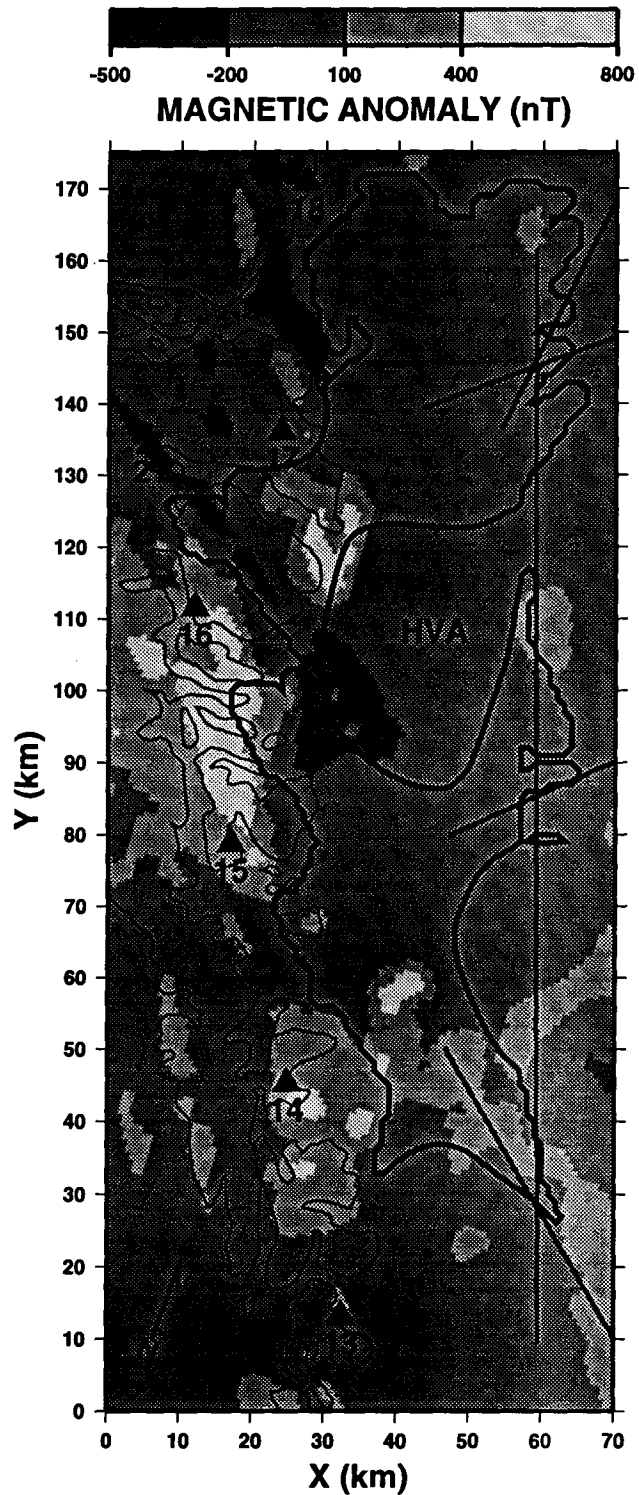


Figure 3.16 Map of magnetic intensity anomaly within the study area gridded at 812.8 m (data from the Geological Survey of Canada Geophysical Data Centre). The shot lines and receiver locations are shown as in Figure 1.2. The large positive magnetic anomalies on land all correlate with mapped igneous rocks (cf. Figure 1.2). The bold line indicates the zero velocity anomaly contour at 7 km depth (Figure 3.14). The central high velocity anomaly (HVA) at depth may be due to an offshore pluton which has no magnetic signature due to the thick overlying sediments of the QC Basin.

4 MODELLING THE MOHO

4.1 Introduction

Wide angle reflections from the Moho are evident in the broadside refraction data as coherent, high amplitude secondary arrivals (Figure 1.4, Appendix A). These data provide constraints on the depth of the Moho. However, the finite difference algorithm of Section 1.4 calculates only first arrival travel times. In this chapter, the algorithm is extended to allow the computation of reflection times. Using this extension, the travel times of the Moho reflection arrivals are interpreted to determine crustal thickness beneath the east coast of the QC Islands. Implications of the results for crustal tectonics are discussed.

4.2 Finite Difference Reflection Travel Times

The finite difference travel time algorithm (Section 1.4) calculates only first arrival travel times and therefore an extension of this method is developed to compute reflection travel times. *Podvin and Lecomte* [1991] and *Matsuoka and Ezaka* [1992] use an imaging condition based on Fermat's principle to compute reflected travel times using 2d finite difference algorithms. A disadvantage of their technique is that it requires that travel times be computed from sources at every shotpoint and at every receiver. A method is developed that requires sources only at every shotpoint (or at every receiver point using travel time reciprocity). This requires considerably less computation time for surveys with a small number of shots and many receivers or vice versa.

The algorithm is extended in Sections 1.4 and 2.2 so that either a planar source or a previously computed travel time field can be read and computations can start at the planar

source or at an arbitrary wall of the 3d travel time field. During the computation of the time at each grid node, the previously computed time at the node is replaced only if the newly computed time is earlier. This test is already an integral part of *Vidale's* [1990] algorithm as it ensures that only the first arrival is computed. To begin the procedure, first arrival travel times are computed from the point source to the reflecting boundary. Velocities below the reflector are defined to be equal to or less than velocities above in order to prevent waves transmitted through the interface from arriving as first arrivals at the reflecting boundary. The computed times at the reflecting boundary are thus the times of the incident down-going wave. Travel times to all grid nodes above the reflector are then replaced with large dummy values. The sampled travel time field is used as input to the finite difference algorithm and computations are started on the bottom face of the model volume. In this manner, the incident travel times on the reflecting boundary are used as a source to propagate the reflected wave upwards through the model. The depth to the reflector can vary by defining the boundary as a function of horizontal position. The spatial sampling interval for the velocity model and travel time calculations is chosen to be small enough that travel time errors associated with the 3d discretization of the depth-varying reflecting boundary are small. Figure 4.1 illustrates the computation technique by showing contoured transmitted and reflected travel times on 2d slices through a 3d sampled travel time field. For illustration purposes, a single ray has been found by following the sampled travel time field from a point at the surface backward along the negative travel time gradient to the reflector and then to the source.

4.3 Moho Depth

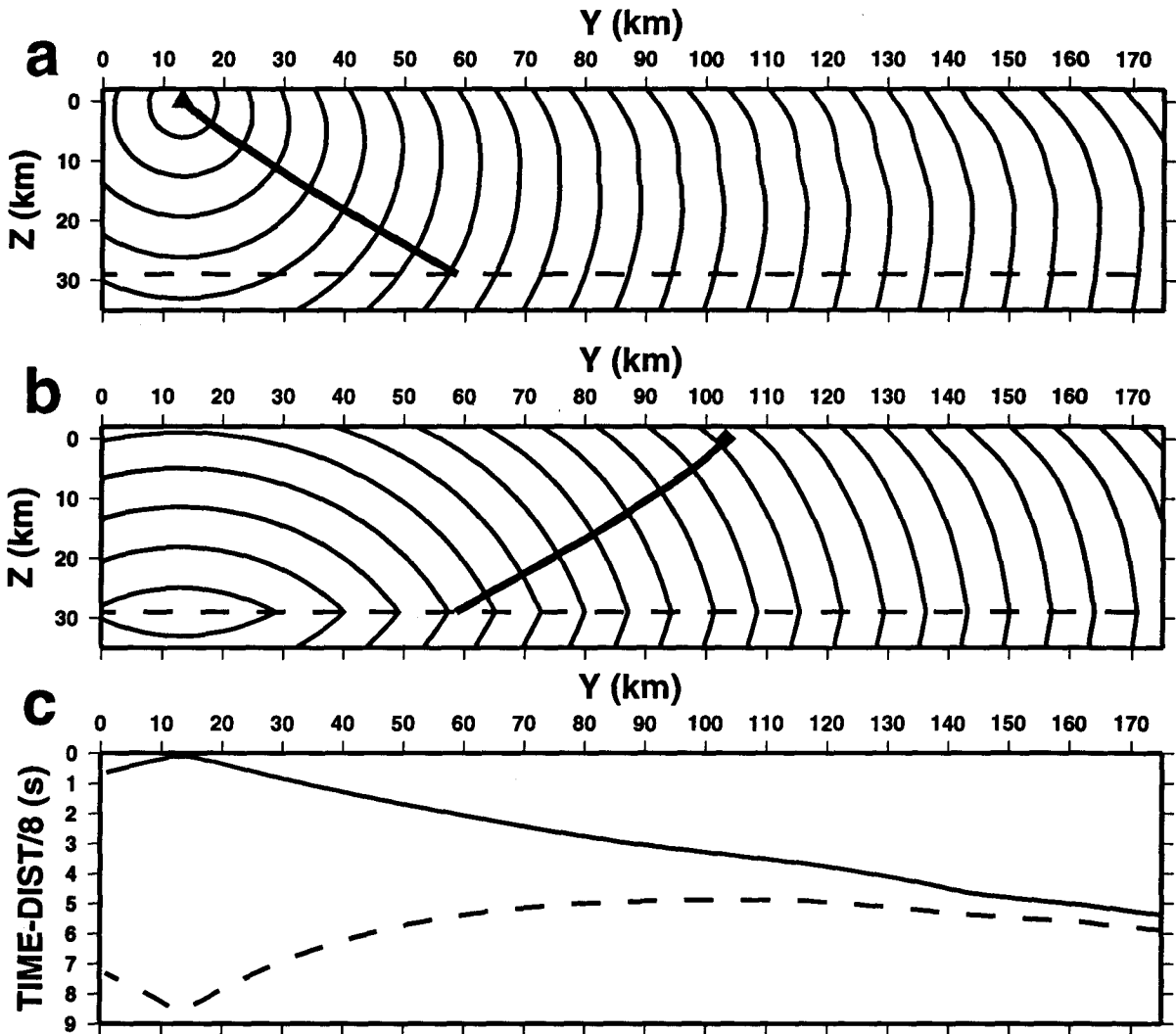


Figure 4.1 Cross-sections through a 3d sampled travel time field. The sections are in the Y-Z plane through the source (triangle) at receiver site 13. Travel times are computed at a 1 km grid spacing and contoured at 1 s intervals. The 3d velocity model of Figure 3.14 is used in the upper crust to a depth of 12 km, a velocity of 6.85 km/s is used in the lower crust and deeper and the Moho is placed at 29 km depth (dashed line). (a) Travel times for the down-going wave. Travel times above the Moho are then replaced with large dummy values and the travel time field is used to initiate computations at the base of the model. The source for this subsequent computation is thus the incident wave (time-varying) at the reflector surface. (b) Travel times for the wave reflected at the Moho. A single ray is shown, found by following the negative travel time gradient through the sampled travel time field backward from a point at the surface (diamond) to the reflector in (b) and then to the source in (a). (c) Travel times at zero depth along the cross sections, reduced by 8 km/s, taken from the crustal arrival in (a) (solid line) and the reflected arrival in (b) (dashed line).

4.3.1 Data

The plotting parameters used in Figure 1.4, Appendix A, and Figure 3.13 to illustrate

the broadside seismic refraction first arrivals do not provide a good image of the secondary arrivals. The data for refraction line 4 recorded at receiver sites 13 and 18 (the longest offset sections) are shown in Figure 4.2 using more appropriate plotting parameters. For plotting purposes only, the same static shifts used for Figure 3.13 are also used in Figure 4.2. Note that these static shifts use the first arrival raypath and will not necessarily correct other raypaths properly. A large amplitude reflection interpreted to be from the Moho is evident in Figure 4.2 at 5 to 6 s. The arrivals are observed at offsets greater than 70 km and the largest amplitudes are at offsets of about 90 km, consistent with observations of the critical reflection by *Yuan et al.* [1992] and *Spence and Asudeh* [1993].

The travel times for the Moho reflection arrivals are picked at a 2.5 km spacing along the shot lines, resulting in 224 travel time data. Reverberations or ringing from earlier arrivals and focussing and defocussing caused by the QC Basin structure make the identification of the arrival times difficult in many of the receiver gathers. Where the first cycle of the arrival has been picked properly, it is accurate to about 25 ms; however, mispicks of one or occasionally two cycles are possible and create errors of 100 or 200 ms. The travel times are corrected for the structure of the QC Basin in a manner similar to that used for the first arrivals, but the reflection raypaths rather than the refraction raypaths are used to move the shots in 3d position and in time to the basement interface.

Figure 4.2 (next page) Broadside refraction data sections for line 4 recorded at (a) receiver 13 and (b) receiver 18, the sections with the longest shot-receiver offsets. For receiver 13, shotpoint 101 is at a shot-receiver offset of 27 km and an azimuth of 258°, and shotpoint 3473 is at 151 km and 170°. For receiver 18, shotpoint 101 is at a shot-receiver offset of 165 km and an azimuth of 329°, and shotpoint 3473 is at 33 km and 266°. The processing and plotting is the same as Figure 3.13 except that traces are stacked at every eleventh shotpoint (495 m along line 4) and the overall plot amplitude is smaller. Energy reflected off the Moho at wide angles is visible between 5 and 6 s (between the diamonds).

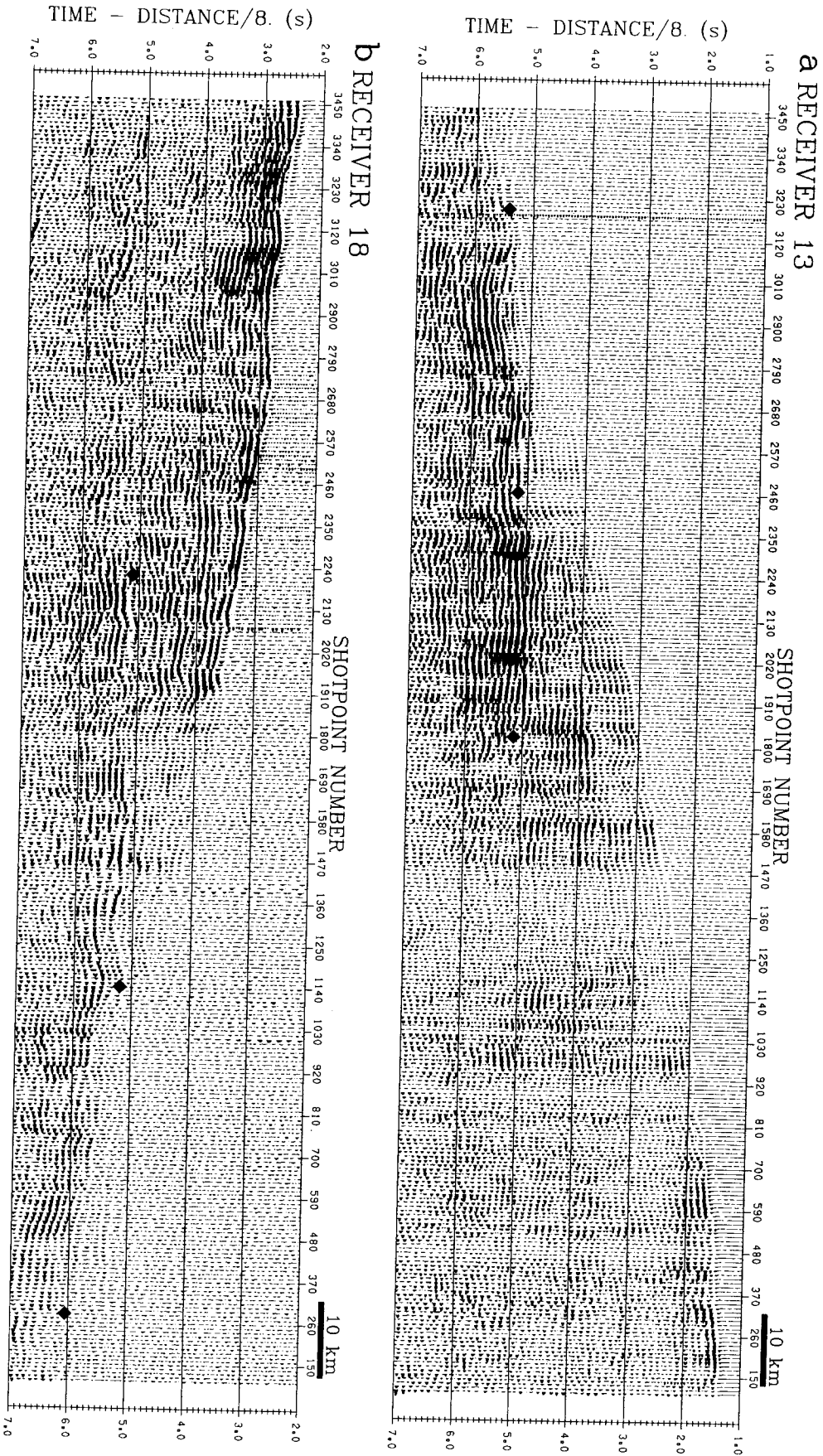


Figure 4.3 shows the shot-receiver midpoints for the Moho picks, indicating that the depth to Moho is constrained from the eastern coast to about 20 km east of the QC Islands. Thus, the broadside Moho reflection data constrain crustal thickness at positions southwest of the 2d constraints of *Spence and Asudeh* [1993] and northwest of the constraints of *Yuan et al.* [1992].

4.3.2 Interpretation Method

A horizontal reflecting boundary is sufficient for the modelling of the Moho reflection data because, as described later, the data do not resolve any Moho topography in this region. The velocity model is sampled at a 1 km grid spacing and Moho reflection travel times are computed using the technique discussed in the previous section. The 3d velocity model (Figure 3.14) is used in the upper crust above 12 km depth. Due to the lack of observed refracted arrivals from the middle and lower crust, the velocities below about 12 km depth are poorly constrained. A suite of 1d velocity models is thus used from 12 km depth to the Moho (Figure 4.4, Table 4.1). The best Moho depth for each velocity model is determined by computing times for a range of depths until the travel time misfit is minimized. *Spence and Asudeh* [1993] and *Yuan et al.* [1992] provide constraints at lower crustal depths derived by modelling the times and amplitudes of wide angle reflections from a mid-crustal interface and the Moho. Additional models, including a 1d upper crust, from these references are used to compare with their Moho interpretations (Figure 4.4, Table 4.1).

4.3.3 Results

Table 4.1 summarizes the results of the modelling of the Moho wide angle reflection

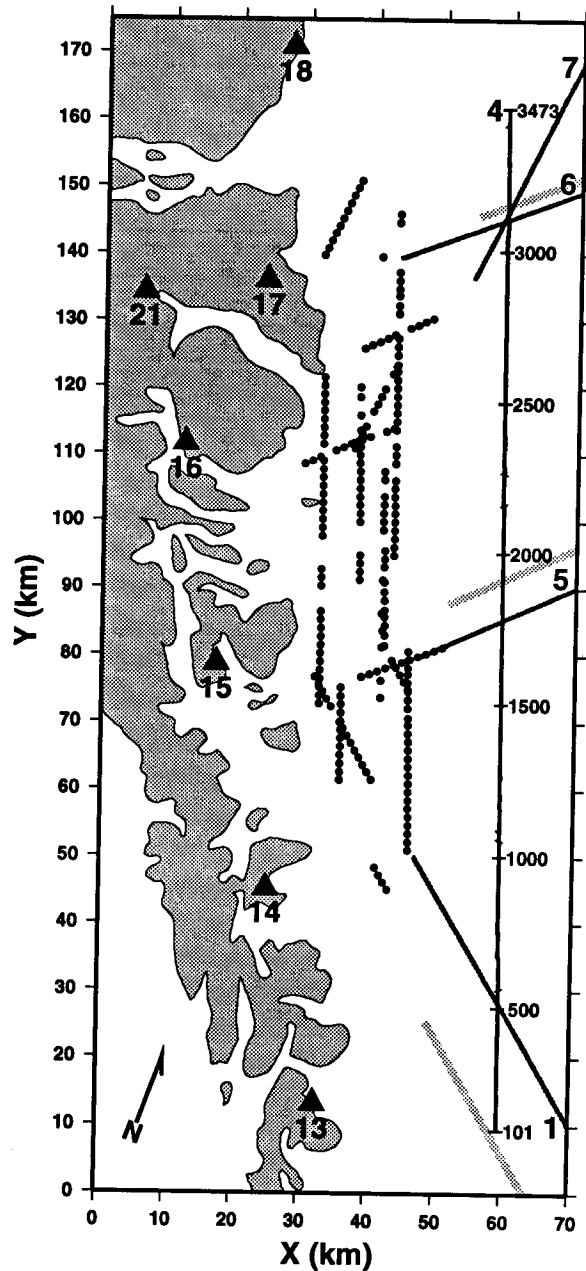


Figure 4.3 Map of the study area, with dots at the shot-receiver midpoints for the Moho reflection picks, indicating the region where the Moho depth is constrained (assuming a 1d velocity model). The grey lines indicate the locations where the models of *Yuan et al.* [1992] and *Spence and Asudeh* [1993] constrain the Moho depth, based on shot-receiver midpoints.

data. The Moho depth varies from 27 to 32 km for the suite of velocity models shown in Figure 4.4. The moveout, or variation with distance, of the travel times indicates that the velocity over the entire crustal interval is too high or too low for several of the velocity models. This places some constraints on velocities in the middle and lower crust and thus

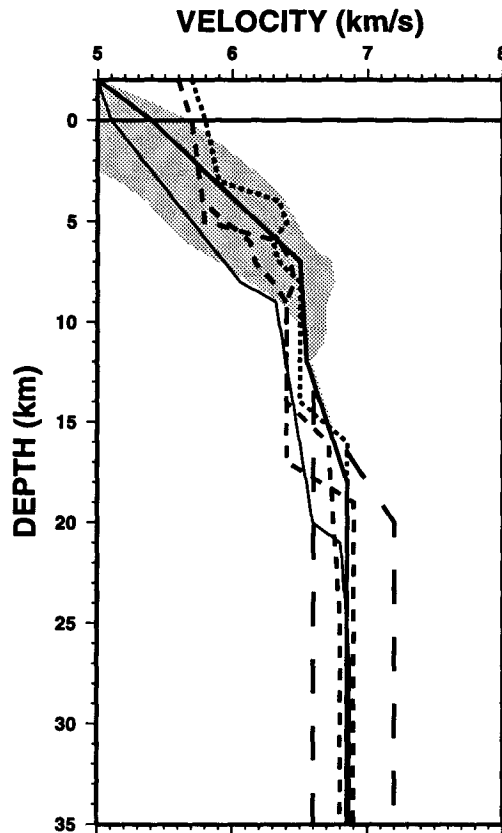


Figure 4.4 One-dimensional plot of the velocity models in Table 4.1 that are used to model the Moho reflection data. The heavy solid line is the “best” velocity model for the lower crust (model A). The grey shading shows the range of lateral velocity variations in the 3d model (Figure 3.14) used in the upper crust in models A, B, and C. The long dashed lines are the “slow” (B) and “fast” (C) lower crustal models, considered as extremes. The dotted line is the 1d model taken from the western end of the model for line 1 (D) from *Yuan et al.* [1992]. The short dashed lines are the 1d models taken from the western ends of the models for line 5 (E) and 6 (F) from *Spence and Asudeh* [1993]. The thin solid line is the 1d model from the 1983 survey (G) of *Mackie et al.* [1989] taken beneath western Hecate Strait at their model distance of 200 km.

on the preferred Moho depth.

Travel time misfits for model A of Table 4.1 are shown in Figures 4.5a and 4.5c. The significant scatter in the misfits produces an error estimate of 1 km on the best Moho depths in Table 4.1. The misfits are due to picking errors, errors on the QC Basin static corrections, and small-spatial-scale errors in the crustal velocity models. The misfits for model A show no correlation with shot-receiver offset (Figure 4.5a), indicating that the crustal interval velocity is good. In comparison, similar plots for models B (Figure 4.5b) and C show several hundred

Table 4.1 Moho modelling.

	Upper crust velocity model	Lower crust velocity model	Best Moho depth	Constraints from moveout on crustal interval velocity
A	3d: broadside refraction model (Figure 3.14)	"best": 6.85 km/s	29 km	good
B	"	"slow": 6.6 km/s	27 km	much too slow
C	"	"fast": 7.2 km/s	32 km	much too fast
D	1d: line 1 model (Yuan et al. 1992)	6.85 km/s	30 km	good
E	1d: line 5 model (Spence and Asudeh 1993)	6.9 km/s	28 km	too slow
F	1d: line 6 model (Spence and Asudeh 1993)	6.8 km/s	28 km	too slow
G	1d: 1983 survey (Mackie et al. 1989)	6.8 km/s	25 km	much too slow

milliseconds of differential moveout, indicating that the interval velocities are much too low and high respectively. Using moveout to constrain the velocities, the best depth to the Moho is about 29 km. No systematic trends are observed in plots of misfit versus position of the shot-receiver midpoint (e.g., Figure 4.5c). This indicates that, within the resolution of the model, there are no large-spatial-scale lateral variations in the Moho depth or in the lower crustal velocity.

Models D, E, and F of Table 4.1 and Figure 4.4 are used to facilitate comparisons of the Moho depth with the results of *Yuan et al.* [1992] to the southeast and *Spence and Asudeh* [1993] to the northeast (Figure 4.3). A 1d model for the entire crust derived from the appropriate ends of the 2d inline refraction interpretations (Figure 4.4) is used to ensure a fair comparison. For line 1, *Yuan et al.* [1992] derived a Moho depth of 27 km, indicating

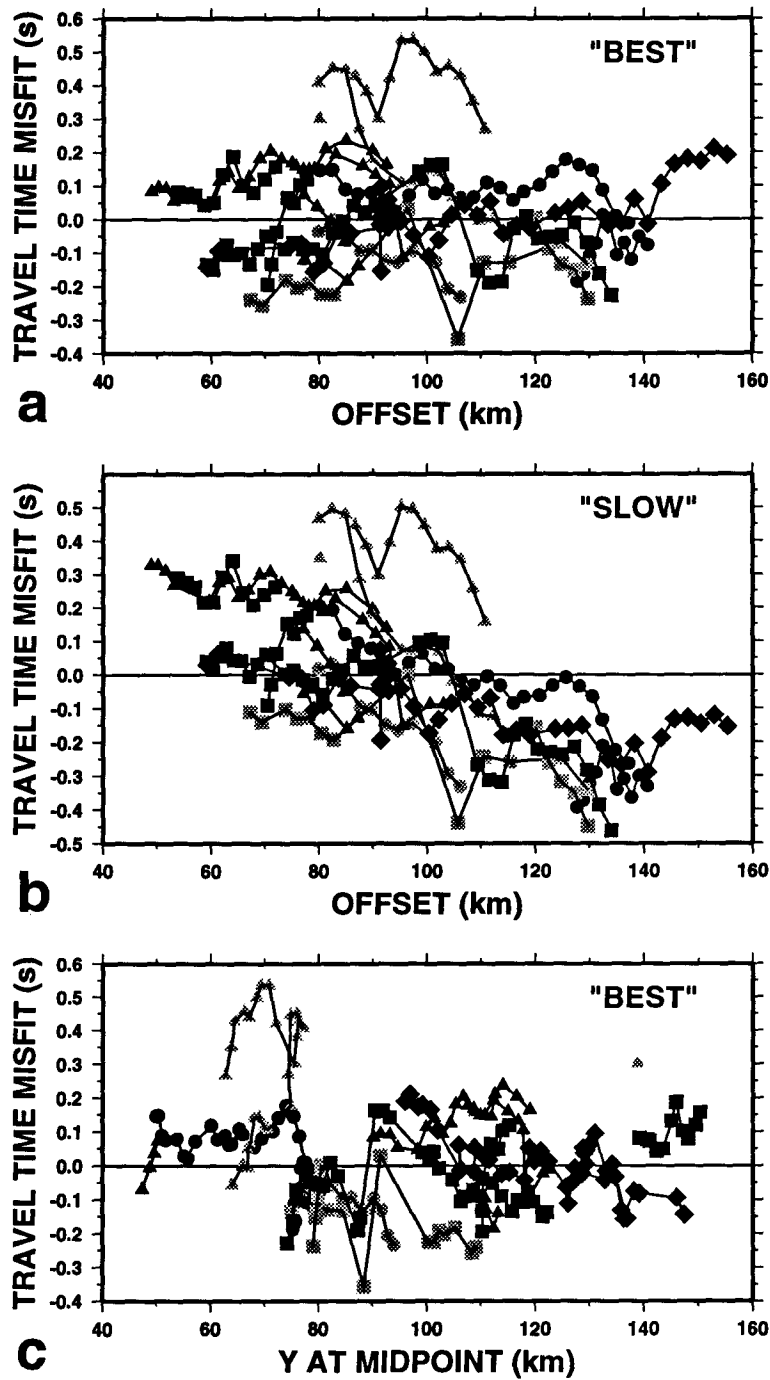


Figure 4.5 Travel time misfits for the Moho reflection data. Each symbol represents the misfits for one receiver, and data from the same shot line are connected. (a) The misfits from velocity model A (Table 4.1, Figure 4.4) plotted against shot-receiver offset. The horizontal trend with offset indicates that the crustal interval velocity is good. (b) The misfits from velocity model B (Table 4.1, Figure 4.4) plotted against shot-receiver offset. The significant non-horizontal trend with offset indicates that the crustal interval velocity is much too slow. (c) The misfits from velocity model A (Table 4.1, Figure 4.4) plotted against the Y coordinate at the shot-receiver midpoint. The horizontal trend indicates that, within resolution, the Moho is horizontal within the region of constraints.

that the Moho is about 3 km shallower than model D (Table 4.1). This is consistent with the suggestion of *Yuan et al.* [1992] that the Moho deepens to the north of their line 1 constraints. Model E (Table 4.1) indicates that the Moho is about 1 km deeper than the 27 km interpretation of *Spence and Asudeh* [1993] along line 5. Although the difference is about the size of the estimated error bounds, the trend to a deeper Moho is consistent with the dip they observed and does not allow a shallower Moho west of their constraints. The Moho depth for model F (Table 4.1) is the same as that of *Spence and Asudeh* [1993] for line 6. Interestingly, the moveout for models E and F indicates that the crustal interval velocity is too low. The only significant velocity difference between these models and model A is within the midcrust between depths of about 8 and 14 km (Figure 4.4). The 3d model places good constraints on the velocities in the upper portion of this region, and thus the slightly higher velocities, as supported by the moveout observations, are preferred. However, since the velocity differences are probably within error margins on the 2d and 3d models, no major lateral differences in mid-crustal velocities are implied. If the mid-crustal velocities of *Spence and Asudeh* [1993] were increased from 6.4 to 6.5 km/s, their Moho depths under lines 5 and 6 would increase by about 1 km.

4.3.4 Discussion

The Moho reflection data in this study indicate that the Moho under the eastern coast of the QC Islands is as deep or deeper than under central Hecate Strait and is deeper than in northern QC Sound. The preferred depth is 29 km. This result contrasts with that of *Mackie et al.* [1989] who use data from a 1983 survey to derive a Moho which dips steadily to the east from 21 km depth beneath the west coast of the QC Islands to over 30 km beneath the

mainland. *Spence and Asudeh* [1993] reinterpret the 1983 data using their line 6 refraction model velocities and conclude that the Moho is approximately flat beneath Hecate Strait and extending to beneath the eastern QC Islands, compatible with the results of this chapter. The difference between the two results is due to higher crustal velocities constrained by the newer data but unknown at the time of the interpretation of *Mackie et al.* [1989]. Model G of Table 4.1 uses the low crustal velocities from *Mackie et al.* [1989] (Figure 4.4), and derives a Moho depth of 25 km, similar to their result beneath the east coast of the QC Islands, and a moveout observation indicating that the velocities are much too low. The low velocities used by *Mackie et al.* [1989] are directly responsible for the dip on their unreversed 2d model of the Moho, requiring the Moho to become shallower to the west, away from their common receiver gathers.

Although the 3d data are compatible with the Moho depths beneath Hecate Strait and the eastern QC Islands being the same, they suggest that the Moho may be deeper beneath the islands. Since the Tertiary QC Basin in Hecate Strait contains up to 6 km of sediments (Chapter 2) [*Shouldice* 1971; *Rohr and Dietrich* 1992], the crust (defined as pre-Tertiary rocks) is at least several kilometres thicker under the QC Islands. *Rohr and Dietrich* [1992] and *Hyndman and Hamilton* [1993] document evidence that the QC Basin is an extensional basin, although consensus has not been reached on the mode of extension [for additional models, see *Thompson et al.* 1991; *Lyatsky* 1991]. Crustal thinning under QC Sound and Hecate Strait has been observed by *Yuan et al.* [1992] and *Spence and Asudeh* [1993] and has been interpreted as the result of crustal extension associated with the formation of the QC Basin. The results of this study suggest that the crust under the QC Islands has not

been extended as much as under the basin, implying that Tertiary lower crustal thinning was greatest beneath the upper crustal extension. *Rohr and Dietrich* [1992] suggest that the islands acted as a relatively strong crustal unit that was capable of transmitting compressional stresses in the late stages of basin formation from the plate margin to the weaker crust under Hecate Strait. This idea is compatible with the localization of extension under the basin and not under the islands. It also may be responsible for the different structural deformation patterns observed in geological mapping onshore and geophysical mapping offshore [e.g., *Lewis et al.* 1991; *Thompson et al.* 1991; *Rohr and Dietrich* 1992].

The crust beneath the QC Islands may also have become thicker as a result of the compression that has existed for the last 4 Ma at the predominantly strike-slip plate margin [*Hyndman and Hamilton* 1993]. *Yorath and Hyndman* [1983], *Mackie et al.* [1989], and *Hyndman and Hamilton* [1993] suggest that the compression has been taken up by oblique subduction of the oceanic crust beneath the QC Islands. An alternative model takes up the compression by deformation of the crust [e.g., *Mackie et al.* 1989]. *Yorath and Hyndman* [1983] and *Hyndman and Hamilton* [1993] propose evidence supporting uplift and eastward tilting of the QC Islands, although geological mapping onshore argues against this model [e.g., *Lewis et al.* 1991]. *Rohr and Dietrich* [1992] provide evidence that Pliocene and later compression formed inversion structures within the QC Basin. Although evidence of significant crustal shortening has not been observed at the surface, shortening of the lower crust cannot be ruled out. Subduction also cannot be ruled out based on present evidence. The dip on a possible subducting slab is constrained by the well-defined depth at the plate boundary [*Dehler and Clowes* 1988; *Mackie et al.* 1989] and the requirement to be deeper

than the continental Moho beneath this study. Moho depth models of *Spence and Asudeh* [1993], strongly supported by this study, require that the subducted oceanic crust dip greater than 10° and possibly as much as 20° . This is significantly steeper than the dip proposed by *Mackie et al.* [1989], but is similar to dips of subducting young oceanic crust of 9° beneath southern QC Sound [*Yuan et al.* 1992] and 11° to 17° beneath western Vancouver Island [*Hyndman et al.* 1990; *Cassidy and Ellis* 1993].

4.3.5 Conclusions

Three-dimensional broadside refraction data are used to determine the Moho depth beneath western Hecate Strait. The Moho under the east coast of the QC Islands is as deep as or deeper than under central Hecate Strait, and is deeper than under QC Sound. The preferred depth is 29 km. The crust is therefore thicker under the islands than under the basin. This is interpreted to be due to the localization of Tertiary extension beneath the surface expression of the QC Basin and/or to crustal thickening adjacent to the plate margin associated with Pliocene to recent compression.

5 SUMMARY AND CONCLUSIONS

5.1 Three-Dimensional Seismology

The increasing number and availability of modern seismographs and advances in interpretation techniques and computer power are beginning to allow the determination of 3d structure from truly 3d crustal seismology. These advances parallel the enthusiastic and successful adoption of 3d reflection seismology in the petroleum industry during the 1980's [e.g., *Nestvold* 1992]. Although the use in the past of a grid of 2d interpretations has provided 3d information, the modelling of seismic energy that has travelled in the third dimension provides true information about the 3d structure of the earth without interpolation. The application of 3d seismology to the study of the earth's crust is just beginning.

5.1.1 Data Acquisition

The 1988 QC survey has shown that useful information can be acquired at relatively low cost by deploying refraction seismographs in a broadside geometry during a multichannel reflection survey. Several surveys in recent years have collected such data [e.g., *GLIMPCE Seismic Refraction Working Group* 1989; *BABEL Working Group* 1990; *Brocher et al.* 1991], with considerable success in recording energy from an airgun array at distances of up to several hundred kilometres. Within Canada, successful results from this study led to the inclusion of an onshore recording component of an offshore airgun and ocean bottom seismograph refraction survey in Newfoundland [*Isbell* 1991]. The successful recording and interpretation of the broadside refraction data in this study were used in the planning of the onshore recording of broadside data during an offshore multichannel reflection survey in

Labrador (K. Loudon, personal communication, 1992). As a piggyback experiment during a multichannel reflection survey, the acquisition of inline and broadside data for refractions and wide angle reflections is a very cost effective way to obtain densely sampled information about the velocity structure of the crust. The budget to obtain such data is only a few percent of the cost of the reflection survey, and is thus encouraged for future surveys, both offshore and on land.

During surveys on land, it may be possible to include the acquisition of refraction data at a few dozen sites in the reflection contract by using telemetered instruments and recording the refraction data in the recording truck with the reflection data. Technical difficulties for the telemetry may exist due to the desired large offsets between the recording truck and the receivers. This could be successful with vibrator data by performing the cross-correlation in the field at the same time as it is carried out for the reflection data.

The goal of such a piggyback survey is to record data at a continuous range of shot-receiver offsets from zero to 50 or 100 km. Such data primarily provide information about the velocity structure of the upper crust. This information is highly complementary to the reflection data and is probably the best tie with geology mapped at the surface, thus simultaneously addressing the scientific interests of both the geologist and the reflection seismologist. The advantage of recording offline 3d data is that, in most regions, the geology changes rapidly, even along nominal strike, and the true 3d subsurface orientation of faults and other structures near the surface can be determined.

The geometry of the QC survey is barely sufficient to perform 3d tomography (Chapter 3). The 3d ray coverage forms a trough with good azimuthal coverage in a very limited

depth range (5–9 km). This is due to the small number of receivers and their location at approximately the same offset from the main shot line. A more complete design for this experiment would involve a second row of receivers along the west coast of the QC Islands to obtain data at different offsets, and a row of ocean bottom seismographs along line 4 to obtain detailed 2d data (the latter was part of the initial survey plan but, due to problems in the field, this part of the survey was unsuccessful). Shot lines crossing the main line also significantly improve the coverage, especially for structure near the shots. For example, the structure of the QC Basin near Fault 3 is much better resolved by the cross line 5 than the structure near Fault 4 without a cross line (Figures 2.7 and 2.9), partly because the faults are subparallel to the shot line.

Survey simulation before the field work can indicate the minimum coverage required to obtain information about the 3d velocity structure. For most surveys, this requires one or two dozen refraction sites per hundred kilometres of shot line. The standard one or two broadside shots used during a traditional crustal refraction survey provide only a tiny amount of 3d information, such as the depth to a single reflector under the (probably poor) assumption that the offline velocity remains constant. Considering the cost of explosives in such a survey, the money for these shots would provide a lot more information by recording another well-resolved 2d line. Taking advantage of the numerous free shots during a reflection survey or recording many shots of an airgun source (e.g., the survey of *Toomey et al.* [1990] described in Topic 3.2.6) is a much more cost effective way of recording enough 3d data to perform a tomographic inversion. An additional advantage of a piggyback survey is that the common sources for both reflection and refraction allow a better integrated interpretation of the two

data sets.

5.1.2 Interpretation Techniques

Trial-and-error forward modelling in three dimensions is not practical if realistically complex models are desired. Inversion algorithms have been presented that allow the interpretation of a large volume of 3d data. The tomographic inversion algorithm of Section 3.2 determines 3d velocity structure and is applicable not only to refraction data, but to any 3d seismic data including multiple cross-borehole seismology, local earthquakes, or teleseismic data. The interface inversion algorithm of Section 2.2 determines the 3d structure of an interface across which there is a velocity contrast. This algorithm uses waves that are non-critically refracted at the interface and assumes that the overlying and underlying velocity structures are known. The combination of interface inversion and tomography has allowed the interpretation of the densely sampled 3d QC broadside refraction first arrivals.

The development of procedures in this study has been driven by the need to interpret a 3d data set. The emphasis is on practical techniques capable of inverting a large data set within a reasonable computation time. Two aspects of the tomography and interface inversion algorithms produce this practicality: the forward modelling procedure used to compute accurate travel times through a model, and the inversion parameterization that allows densely sampled models without solving a huge system of linear equations. The finite difference travel time algorithm [Vidale 1990] provides large savings in computation time as compared to 3d two-point ray tracing. Improvements and extensions to the algorithm allow the incorporation of large sharp velocity contrasts (Section 1.4), regridding of the model in regions where better resolution is required (Subtopic 2.2.2.1), and the computation of

reflection travel times (Section 4.2). The speed of the finite difference computation of travel times is essential for the nonlinear iterative inversion for arbitrarily large velocity variations in the tomography algorithm and for large depth variations in the interface inversion algorithm.

The inversion parameterizations in both the tomography and interface inversion procedures are unusual. Both take advantage of the facts that the linearization of the seismic travel time problem uses a fixed ray location and that these rays have no volume of overlap. This means that the kernel functions used to create the data are linearly independent and the solution of a large system of linear equations can be avoided with an appropriate choice of parameterization. The inversion parameterization does not have to be the same as the parameterizations used for visualization or for further forward modelling, and has thus been chosen to minimize the computational costs of the inversion. Although the assumptions of the linearization and parameterization are approximations, they are sufficient for iterative nonlinear inversion. Thus the inversion algorithms reduce the traditional solution of a large system of linear equations to a simple analytic expression followed by an interpolation or gridding step required for further forward modelling. The computational speed advantages of this approach, combined with the speed of the forward modelling algorithm, allow both the interface in the interface inversion and the velocity model in the tomography to be densely sampled. The spatial resolution of the resulting models is thus determined by the ray geometry and not by the inversion algorithm.

5.1.2.1 Future Work

The finite difference travel time algorithm of *Vidale* [1988, 1990] defines the velocity model by specifying values at the uniformly spaced set of grid nodes. The finite difference

operators are centred on the volume between nodes and propagate times through this volume, and thus they use the average velocity computed from the appropriate neighbouring nodes. It is physically more reasonable to define the model using constant velocities within each grid cell, eliminating the need to interpolate velocities between the nodes. Travel times would still be computed at the nodes. This model is more physically intuitive since the velocity is known at all points in the model, and is completely consistent with the finite difference operators which represent local plane waves. Constant velocity cells are also consistent with the straight ray assumption used when finding rays. An additional advantage of constant velocity cells is that the location of interfaces is exactly defined to be along the cell boundaries, rather than vaguely situated somewhere between nodes. The finite difference travel time algorithm can be altered so that the velocity model is defined in this way, without causing any changes in the physics or methodology. Similarly, changes can be made to the inversion algorithms to represent the tomographic velocity and the interface in a consistent manner.

Now that reflection travel times can be computed by the finite difference algorithm (Section 4.2), reflected travel times can be included in the tomographic inversion for velocity structure by assuming that the depth of the reflector is known. Reflected rays can be incorporated into the algorithm in a straight-forward manner, although the actual finding of the ray must be split into two segments (Figure 4.1). In addition, reflection travel times can be used to determine the depth to a reflecting interface, assuming a known velocity model, in a similar manner to the refracting interface inversion algorithm (Section 2.2). The joint inversion for velocity and interface depth can be performed in an iterative manner. Analogous to equation 2.1, the partial derivative relating the depth of the interface to the

reflection travel time is

$$\frac{\delta t}{\delta z} = \frac{2 \cos \theta}{v} \cos \alpha \quad , \quad (5.1)$$

where the nomenclature is the same as in equation 2.1 except that θ and v are defined only above the interface [e.g., *Williamson 1990; Stork 1992*]. All of the variables on the right can be obtained from the model and the ray. Thus, a joint inversion of reflection, refraction and head wave travel times to determine the depth to a single interface can be implemented.

Once the velocity model has been determined, the raypaths can be used for amplitude tomography [e.g., *White 1989b*]. *Vidale and Houston [1990]* present a method to compute amplitudes using the finite difference travel time algorithm. The inversion for attenuation, or Q , structure is a linear inversion following the determination of the velocity model and the ray geometries. This inversion can be easily performed using the finite difference algorithm and parameterization.

5.2 The Queen Charlotte Basin and Underlying Crust

The broadside refraction data recorded on the QC Islands have been interpreted to determine the 3d structure of the QC Basin and underlying crust beneath western Hecate Strait. Relative lateral variations on the first arrival travel times were inverted to obtain a map of the thickness of the QC Basin (Figure 2.7). The 3d structure of the basement is defined beneath and offline from the shot lines. The basin thickness varies rapidly between ~ 200 m and ~ 6 km in a sequence of fault-bounded subbasins. After the QC Basin structure near the shot lines was determined, the first arrival travel times were inverted using tomography to obtain the 3d crustal velocity structure (Figure 3.14). Significant lateral velocity variations are mapped. Wide angle reflections were used to determine a Moho depth of 29 km beneath

the eastern coast of the QC Islands. Within the resolution of about 1 km, the Moho is flat in the 80 km long constrained region.

Hyndman and Hamilton [1993], Rohr and Dietrich [1992], and Spence and Asudeh [1993] present evidence for extension in Hecate Strait, contrary to previous models of a flexural origin for this part of the basin [*Yorath and Hyndman 1983*]. Evidence for extension includes the complex sequence of subbasins observed by *Rohr and Dietrich [1992]* in the reflection data which is also observed in the basement model determined using the broadside refraction data. Several faults that produce vertical topography on the basement are observed in the refraction model (Figure 2.7). The true strike of these faults is determined by the 3d constraints and the structure across them can be used to constrain models for the tectonic evolution of the basin. Recently proposed models that incorporate extension orthogonal to the plate margin [*Thompson et al. 1991; Hyndman and Hamilton 1993*] would be expected to form large simple basin structures. The observed subbasins are only tens of kilometres in size and have significant topography with bounding faults at various orientations. This evidence suggests a more complex model for the formation of the basin. The predictable basin geometry suggested by simple en echelon rifting models [*Hyndman and Hamilton 1993; Souther and Jessop 1991*] is not observed in the basin thickness maps [*Rohr and Dietrich 1992*] (Figure 2.7). *Rohr and Dietrich [1992]* use a simple analysis of a shear stress system to predict the orientation and motion of faulting in a model of distributed strike-slip shear extension. Two of the faults mapped by the broadside refraction data strike northwest (Figure 2.7), consistent with predicted dextral strike-slip faults. The basement topography observed across these faults is consistent with dextral strike-slip motion. The two other major

mapped faults strike north-northeast, consistent with predicted extensional faults. Structures observed in the refraction model and in the reflection data suggest that both of these faults bound simple extensional half-grabens. Although the basement topography across the faults cannot uniquely constrain the sense of motion, the observed topography and orientations are consistent with the predictions of the model of distributed strike-slip shear extension. The complexity of the observed topography in the region of three of the faults would be difficult to explain with simple extensional stress systems or with purely vertical fault motions.

Evidence of crustal thinning beneath the QC basin has been presented by *Yuan et al.* [1992] and *Spence and Asudeh* [1993]. Moho depths derived from wide angle reflections recorded in the broadside refraction data indicate that the Moho is deeper than previously believed beneath the east coast of the QC Islands. Analysis of the data suggests that the interval velocity for the crust is slightly higher than that used by *Spence and Asudeh* [1993] and results in depth values about 1 km deeper than they reported. Although this reduces the quantitative value of crustal thinning in Hecate Strait, their conclusion of significant thinning is still supported. Considering the thickness of the QC Basin, the crust is much thinner under Hecate Strait than under the QC Islands, probably indicating that crustal thinning during Tertiary extension was greatest beneath the surface extent of the basin. This is consistent with the idea proposed by *Rohr and Dietrich* [1992] that the crust beneath the islands acted as a relatively rigid block capable of transmitting stresses from the plate margin inland to the weaker crust beneath the basin, and may explain some of the differences in structural styles observed in the seismic data offshore and in geological mapping on land. Alternatively, thicker crust under the QC Islands may have been caused by recent compression at the plate

boundary. Although there is little evidence near the surface of significant crustal shortening since basin formation, thickening of the lower crust or subduction cannot be ruled out. If subduction occurs, the Moho depth data constrain the slab to dip at least 10° to the northeast.

Seismic velocities provide information about the crustal rocks underlying the basin. The 1d average model for the crust indicates that the velocities increase rapidly until about 7 km depth. This depth interval probably includes Tertiary volcanic rocks, Cretaceous sediments, and possibly Wrangellian sediments and volcanics that overlie the Karmutsen Formation. The velocity remains approximately constant at 6.5 km/s from 7 km to at least 12 km depth and is interpreted to be due to Wrangellian Karmutsen Formation rocks. Moho reflection travel times constrain the interval velocity of the crust and are modelled using lower crustal velocities of 6.8 to 6.9 km/s. Lateral velocity variations determined by 3d tomography indicate variations in the existence, depth, and thickness of the various geological units. The basement interface model and the velocities derived from the tomographic inversion, combined with the reflection data, provide evidence for a thick sequence of interbedded sedimentary and volcanic rocks in the deepest part of the Tertiary basin east of the central QC Islands to a depth of about 6 km. The shallow crustal velocities are highest adjacent to the southern QC Islands. Since the age of surface rocks mapped onshore increases to the south, this trend is probably responsible for the higher velocities near the surface in this region. A large high velocity anomaly in the centre of the study area contains velocities that exceed 6.6 km/s at 7 km depth. The anomaly extends over the entire depth range that is constrained by the data, but is well constrained laterally. This anomaly is interpreted to be due to the deep root of an igneous intrusion, based on the high velocities and on Jurassic

and Tertiary plutonic suites mapped on the QC Islands.

5.3 Summary

Three-dimensional seismic refraction data recorded in the Queen Charlotte Islands during a multichannel reflection survey have been interpreted to determine the geology and tectonic evolution of the QC Basin and underlying crust beneath western Hecate Strait. Inversion procedures capable of modelling a large, densely sampled set of travel times were developed to derive detailed 3d velocity and structure models. These models have placed constraints on the style of extensional tectonics responsible for the formation of the QC Basin and have aided in the identification of underlying lithologies.

REFERENCES

- Aki, K., A. Christoffersson, and E.S. Husebye, 1977. Determination of the three-dimensional seismic structure of the lithosphere. *J. Geophys. Res.*, **82**, 277–296.
- Anderson, R.G., and I. Reichenbach, 1991. U-Pb and K-Ar framework for Middle to Late Jurassic (172–≥158 Ma) and Tertiary (46–27 Ma) plutons in Queen Charlotte Islands, British Columbia. *In* G.J. Woodsworth (editor), *Evolution and Hydrocarbon Potential of the Queen Charlotte Basin, British Columbia*, Geol. Surv. Can. Paper 90–10, 59–87.
- BABEL Working Group, 1990. Evidence for early Proterozoic plate tectonics from seismic reflection profiles in the Baltic Shield. *Nature*, **348**, 34–38.
- Bamford, D., 1976. MOZAIK time-term analysis. *Geophys. J. R. Astron. Soc.*, **44**, 433–446.
- Berry, M.J., and G.F. West, 1966. An interpretation of the first-arrival data of the Lake Superior Experiment by the time-term method. *Bull. Seismol. Soc. Am.*, **56**, 141–171.
- Bird, D.N., 1982. A linear programming approach to time-term analysis. *Bull. Seismol. Soc. Am.*, **72**, 2171–2180.
- Bregman, N.D., R.C. Bailey, and C.H. Chapman, 1989. Crosshole seismic tomography. *Geophysics*, **54**, 200–215.
- Brocher, T.M., S.L. Klemperer, U.S. ten Brink, and W.S. Holbrook, 1991. Wide-angle seismic profiling of San Francisco Bay area faults: Preliminary results from BASIX (abstract). *Eos Trans. Amer. Geophys. Union*, **72**, Fall Meeting Suppl., 446.
- Cassidy, J.F., and R.M. Ellis, 1993. S-wave velocity structure of the northern Cascadia subduction zone. *J. Geophys. Res.*, in press.
- Chou, C.W., and J.R. Booker, 1979. A Backus-Gilbert approach to inversion of travel-time data for three-dimensional velocity structure. *Geophys. J. R. Astron. Soc.*, **59**, 325–344.
- Clowes, R.M., and E. Gens-Lenartowicz, 1985. Upper crustal structure of southern Queen Charlotte Basin from sonobuoy refraction studies. *Can. J. Earth Sci.*, **22**, 1696–1710.
- Dehler, S.A., and R.M. Clowes, 1988. The Queen Charlotte Islands refraction project Part I: The Queen Charlotte Fault Zone. *Can. J. Earth Sci.*, **25**, 1857–1870.
- Dines, K.A., and R.J. Lytle, 1979. Computerized geophysical tomography. *Proc. IEEE*, **67**, 1065–1073.
- Forsyth, D.A., M.J. Berry, and R.M. Ellis, 1974. A refraction survey across the Canadian Cordillera at 54°N. *Can. J. Earth Sci.*, **11**, 533–548.

- Gardner, L.W., 1939. An areal plan of mapping subsurface structure by refraction shooting. *Geophysics*, **4**, 247–259.
- GLIMPCE Seismic Refraction Working Group, 1989. GLIMPCE seismic experiments. *Eos Trans. Amer. Geophys. Union*, **70**, 841&852–853.
- Haggart, J.W., 1991. A synthesis of Cretaceous stratigraphy, Queen Charlotte Islands, British Columbia. *In* G.J. Woodsworth (editor), *Evolution and Hydrocarbon Potential of the Queen Charlotte Basin, British Columbia*, Geol. Surv. Can. Paper 90–10, 253–277.
- Harris, J.M., S. Lazaratos, and R. Michelena, 1990. Tomographic string inversion (abstract). *Soc. Expl. Geophys. Meeting Expanded Abstracts*, 82–85.
- Hawley, B.W., G. Zandt, and R.B. Smith, 1981. Simultaneous inversion for hypocenters and lateral velocity variations: An iterative solution with a layered model. *J. Geophys. Res.*, **86**, 7073–7086.
- Hickson, C.J., 1991. The Masset Formation on Graham Island, Queen Charlotte Islands, British Columbia. *In* G.J. Woodsworth (editor), *Evolution and Hydrocarbon Potential of the Queen Charlotte Basin, British Columbia*, Geol. Surv. Can. Paper 90–10, 305–324.
- Higgs, R., 1991. Sedimentology, basin-fill architecture and petroleum geology of the Tertiary Queen Charlotte Basin, British Columbia. *In* G.J. Woodsworth (editor), *Evolution and Hydrocarbon Potential of the Queen Charlotte Basin, British Columbia*, Geol. Surv. Can. Paper 90–10, 337–371.
- Humphreys, E., and R.W. Clayton, 1988. Adaptation of back projection tomography to seismic travel time problems. *J. Geophys. Res.*, **93**, 1073–1085.
- Humphreys, E., R.W. Clayton, and B.H. Hager, 1984. A tomographic image of mantle structure beneath southern California. *Geophys. Res. Lett.*, **11**, 625–627.
- Hyndman, R.D., and T.S. Hamilton, 1991. Cenozoic relative plate motions along the northeastern Pacific margin and their association with Queen Charlotte area tectonics and volcanism. *In* G.J. Woodsworth (editor), *Evolution and Hydrocarbon Potential of the Queen Charlotte Basin, British Columbia*, Geol. Surv. Can. Paper 90–10, 107–126.
- Hyndman, R.D., and T.S. Hamilton, 1993. Queen Charlotte area Cenozoic tectonics and volcanism and their association with relative plate motions along the northeastern Pacific margin. *J. Geophys. Res.*, in press.
- Hyndman, R.D., C.J. Yorath, R.M. Clowes, and E.E. Davis, 1990. The northern Cascadia subduction zone at Vancouver Island: Seismic structure and tectonic history. *Can. J. Earth Sci.*, **27**, 313–329.
- Isbell, W.B., 1991. Lithoprobe East 1991 — Summary report of land-based refraction Part I: Field work and data collection. Unpublished report, University of British Columbia, Department of Geophysics and Astronomy, Vancouver, 19 pp.

- Ivansson, S., 1985. A study of methods for tomographic velocity estimation in the presence of low-velocity zones. *Geophysics*, **50**, 969–988.
- Johnson, S.H., R.W. Couch, M. Gemperle, and E.R. Banks, 1972. Seismic refraction measurements in southeast Alaska and western British Columbia. *Can. J. Earth Sci.*, **9**, 1756–1765.
- Kanasewich, E.R., and S.K.L. Chiu, 1985. Least-squares inversion of spatial seismic refraction data. *Bull. Seismol. Soc. Am.*, **75**, 865–880.
- Lewis, P.D., J.W. Haggart, R.G. Anderson, C.J. Hickson, R.I. Thompson, J.R. Dietrich, and K.M.M. Rohr, 1991. Triassic to Neogene geologic evolution of the Queen Charlotte region. *Can. J. Earth Sci.*, **28**, 854–869.
- Lyatsky, H.V., 1991. Regional geophysical constraints on crustal structure and geologic evolution of the Insular Belt, British Columbia. *In* G.J. Woodsworth (editor), *Evolution and Hydrocarbon Potential of the Queen Charlotte Basin, British Columbia*, Geol. Surv. Can. Paper 90–10, 97–106.
- Mackie, D.J., R.M. Clowes, S.A. Dehler, R.M. Ellis, and P. Morel-à-l’Huissier, 1989. The Queen Charlotte Islands refraction project Part II: Structural model for transition from Pacific plate to North American plate. *Can. J. Earth Sci.*, **26**, 1713–1725.
- Matsuoka, T., and T. Ezaka, 1992. Ray tracing using reciprocity. *Geophysics*, **57**, 326–333.
- McMechan, G.A., 1983. Seismic tomography in boreholes. *Geophys. J. R. Astron. Soc.*, **74**, 601–612.
- Menke, W., 1984. The resolving power of cross-borehole tomography. *Geophys. Res. Lett.*, **11**, 105–108.
- Michelena, R.J., and J.M. Harris, 1991. Tomographic traveltimes inversion using natural pixels. *Geophysics*, **56**, 635–644.
- Nakanishi, I., 1985. Three-dimensional structure beneath the Hokkaido-Tohoku region as derived from a tomographic inversion of P-arrival times. *J. Phys. Earth*, **33**, 241–256.
- NAT Study Group, 1985. North Atlantic Transect: A wide-aperture, two-ship multichannel seismic investigation of the oceanic crust. *J. Geophys. Res.*, **90**, 10321–10341.
- Nestvold, E.O., 1992. 3-D seismic: Is the promise fulfilled? *Geophysics: The Leading Edge of Exploration*, **11**, 12–19.
- Peterson, J.E., Jr., and A. Davey, 1991. Crossvalidation method for crosswell seismic tomography. *Geophysics*, **56**, 385–389.
- Peterson, J.E., B.N.P. Paulsson, and T.V. McEvelly, 1985. Applications of algebraic reconstruction techniques to crosshole seismic data. *Geophysics*, **50**, 1566–1580.

- Pike, C.J., 1986. A seismic refraction study of the Hecate sub-basin, British Columbia. M.Sc. thesis, University of British Columbia, Department of Geophysics and Astronomy, Vancouver, 133 pp.
- Podvin, P., and I. Lecomte, 1991. Finite difference computation of traveltimes in very contrasted velocity models: A massively parallel approach and its associated tools. *Geophys. J. Int.*, **105**, 271–284.
- Purdy, G.M., 1982. The correction for the travel time effects of seafloor topography in the interpretation of marine seismic data. *J. Geophys. Res.*, **87**, 8389–8396.
- Qin, F., Y. Luo, K.B. Olsen, W. Cai, and G.T. Schuster, 1992. Finite-difference solution of the eikonal equation along expanding wavefronts. *Geophysics*, **57**, 478–487.
- Raitt, R.W., G.G. Shor, Jr., T.J.G. Francis, and G.B. Morris, 1969. Anisotropy of the Pacific upper mantle. *J. Geophys. Res.*, **74**, 3095–3109.
- Reid, I.D., and C.E. Keen, 1990. Deep crustal structure beneath a rifted basin: Results from seismic refraction measurements across the Jeanne d'Arc Basin, offshore eastern Canada. *Can. J. Earth Sci.*, **27**, 1462–1471.
- Rohr, K.M.M., and J.R. Dietrich, 1990. Deep seismic survey of Queen Charlotte Basin. *Geol. Surv. Can. Open File 2258*, 7 pp.
- Rohr, K.M.M., and J.R. Dietrich, 1991. Deep seismic reflection survey of the Queen Charlotte Basin, British Columbia. In G.J. Woodsworth (editor), *Evolution and Hydrocarbon Potential of the Queen Charlotte Basin, British Columbia*, *Geol. Surv. Can. Paper 90-10*, 127–133.
- Rohr, K.M.M., and J.R. Dietrich, 1992. Strike-slip tectonics and development of the Tertiary Queen Charlotte Basin, offshore western Canada: Evidence from seismic reflection data. *Basin Res.*, **4**, 1–19.
- Scales, J.A., 1987. Tomographic inversion via the conjugate gradient method. *Geophysics*, **52**, 179–185.
- Scheidegger, A.E., and P.L. Willmore, 1957. The use of a least squares method for the interpretation of data from seismic surveys. *Geophysics*, **22**, 9–22.
- Schneider, W.A., Jr., K.A. Ranzinger, A.H. Balch, and C. Kruse, 1992. A dynamic programming approach to first arrival traveltimes computation in media with arbitrarily distributed velocities. *Geophysics*, **57**, 39–50.
- Shor, G.G., Jr., 1962. Seismic refraction studies off the coast of Alaska: 1956–1957. *Bull. Seismol. Soc. Am.*, **52**, 37–57.
- Shouldice, D.H., 1971. Geology of the western Canadian continental shelf. *Bull. Can. Petrol. Geol.*, **19**, 405–436.

- Souther, J.G., and A.M. Jessop, 1991. Dyke swarms in the Queen Charlotte Islands, British Columbia, and implications for hydrocarbon exploration. *In* G.J. Woodsworth (editor), *Evolution and Hydrocarbon Potential of the Queen Charlotte Basin, British Columbia*, Geol. Surv. Can. Paper 90-10, 465-487.
- Spence, G.D., and I. Asudeh, 1993. Seismic velocity structure of the Queen Charlotte Basin beneath Hecate Strait. *Can. J. Earth Sci.*, in press.
- Spence, G.D., J.A. Hole, I. Asudeh, R.M. Ellis, R.M. Clowes, T. Yuan, and K.M.M. Rohr, 1991. A seismic refraction study in the Queen Charlotte Basin, British Columbia. *In* G.J. Woodsworth (editor), *Evolution and Hydrocarbon Potential of the Queen Charlotte Basin, British Columbia*, Geol. Surv. Can. Paper 90-10, 135-149.
- Spence, G.D., T. Yuan, J.A. Hole, I. Asudeh, R.M. Ellis, R.M. Clowes, K.M.M. Rohr, and R.D. Hyndman, 1992. Queen Charlotte Basin Refraction Experiment, 1988. Geol. Surv. Can. Open File 2544, 51 pp.
- Stacey, R.A., 1975. Structure of the Queen Charlotte Basin. *In* C.J. Yorath, E.R. Parker, and D.J. Glass (editors), *Canada's Continental Margins and Offshore Petroleum Exploration*, Can. Soc. Petrol. Geol., Memoir 4, 723-741.
- Stork, C., 1992. Reflection tomography in the postmigrated domain. *Geophysics*, **57**, 680-692.
- Sutherland Brown, A., 1968. Geology of the Queen Charlotte Islands, British Columbia. British Columbia Dept. Mines and Petrol. Res., Bull. 54, 246 pp.
- Sweeney, J.F., and D.A. Seemann, 1991. Crustal density structure of Queen Charlotte Islands and Hecate Strait, British Columbia. *In* G.J. Woodsworth (editor), *Evolution and Hydrocarbon Potential of the Queen Charlotte Basin, British Columbia*, Geol. Surv. Can. Paper 90-10, 89-96.
- Tarantola, A., and A. Nercessian, 1984. Three-dimensional inversion without blocks. *Geophys. J. R. Astron. Soc.*, **76**, 299-306.
- Thompson, R.I., J.W. Haggart, and P.D. Lewis, 1991. Late Triassic through early Tertiary evolution of the Queen Charlotte Basin, British Columbia, with a perspective on hydrocarbon potential. *In* G.J. Woodsworth (editor), *Evolution and Hydrocarbon Potential of the Queen Charlotte Basin, British Columbia*, Geol. Surv. Can. Paper 90-10, 3-29.
- Thomson, C.J., and D. Gubbins, 1982. Three-dimensional lithospheric modelling at NORSAR: Linearity of the method and amplitude variations from the anomalies. *Geophys. J. R. Astron. Soc.*, **71**, 1-36.
- Thurber, C.H., 1983. Earthquake locations and three-dimensional crustal structure in the Coyote Lake area, central California. *J. Geophys. Res.*, **88**, 8226-8236.
- Toomey, D.R., and G.R. Foulger, 1989. Tomographic inversion of local earthquake data from the Hengill-Grensdalur central volcano complex, Iceland. *J. Geophys. Res.*, **94**, 17497-17510.

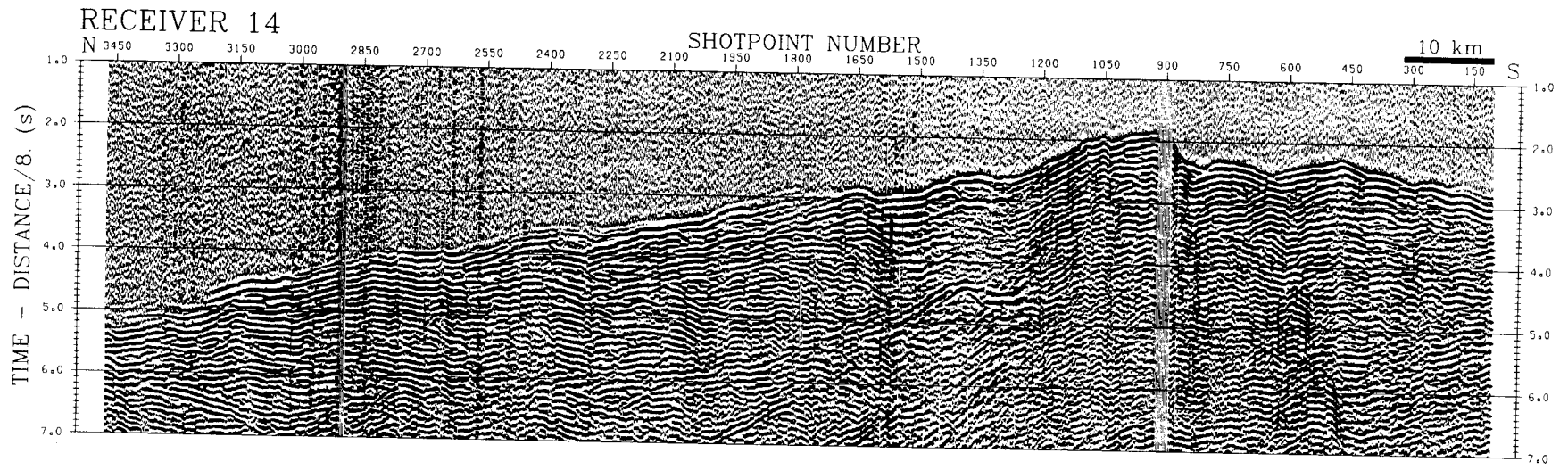
- Toomey, D.R., G.M. Purdy, S.C. Solomon, and W.S.D. Wilcock, 1990. The three-dimensional seismic velocity structure of the East Pacific Rise near latitude 9°30'N. *Nature*, **347**, 639–645.
- Van Trier, J., and W.W. Symes, 1991. Upwind finite-difference calculation of traveltimes. *Geophysics*, **56**, 812–821.
- Vidale, J.E., 1988. Finite-difference calculation of travel times. *Bull. Seismol. Soc. Am.*, **78**, 2062–2076.
- Vidale, J.E., 1990. Finite-difference calculation of traveltimes in three dimensions. *Geophysics*, **55**, 521–526.
- Vidale, J.E., and H. Houston, 1990. Rapid calculation of seismic amplitudes. *Geophysics*, **55**, 1504–1507.
- Weatherby, B.B., 1940. The history and development of seismic prospecting. *Geophysics*, **5**, 215–230.
- White, D.J., 1989*a*. Two-dimensional seismic refraction tomography. *Geophys. J.*, **97**, 223–245.
- White, D.J., 1989*b*. Shallow crustal structure beneath the Juan de Fuca Ridge from 2D seismic refraction tomography. Ph.D. thesis, University of British Columbia, Department of Geophysics and Astronomy, Vancouver, 177 pp.
- White, J.M., 1990. Evidence of Paleogene sedimentation on Graham Island, Queen Charlotte Islands, west coast, Canada. *Can. J. Earth Sci.*, **27**, 533–538.
- Williamson, P.R., 1990. Tomographic inversion in reflection seismology. *Geophys. J. Int.*, **100**, 255–274.
- Woodsworth, G.J. (editor), 1991. Evolution and Hydrocarbon Potential of the Queen Charlotte Basin, British Columbia. *Geol. Surv. Can. Paper 90–10*, 569 pp.
- Wong, J., P. Hurley, and G.F. West, 1983. Crosshole seismology and seismic imaging in crystalline rocks. *Geophys. Res. Lett.*, **10**, 686–689.
- Yorath, C.J., and R.L. Chase, 1981. Tectonic history of the Queen Charlotte Islands and adjacent areas — a model. *Can. J. Earth Sci.*, **18**, 1717–1739.
- Yorath, C.J., and R.D. Hyndman, 1983. Subsidence and thermal history of Queen Charlotte Basin. *Can. J. Earth Sci.*, **20**, 135–159.
- Yuan, T., G.D. Spence, and R.D. Hyndman, 1992. Structure beneath Queen Charlotte Sound from seismic refraction and gravity interpretations. *Can. J. Earth Sci.*, **29**, 1509–1529.

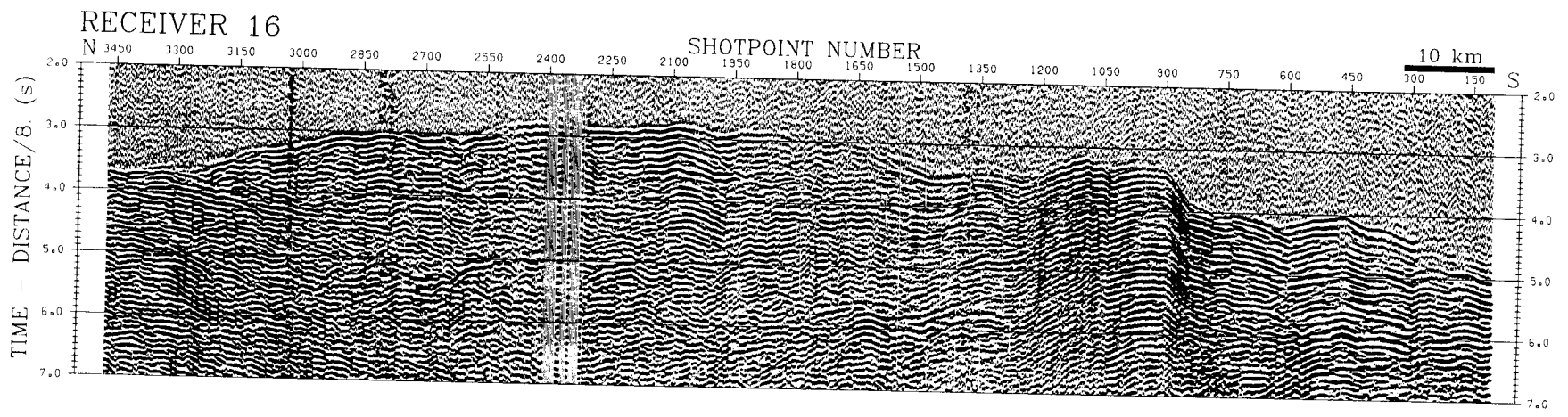
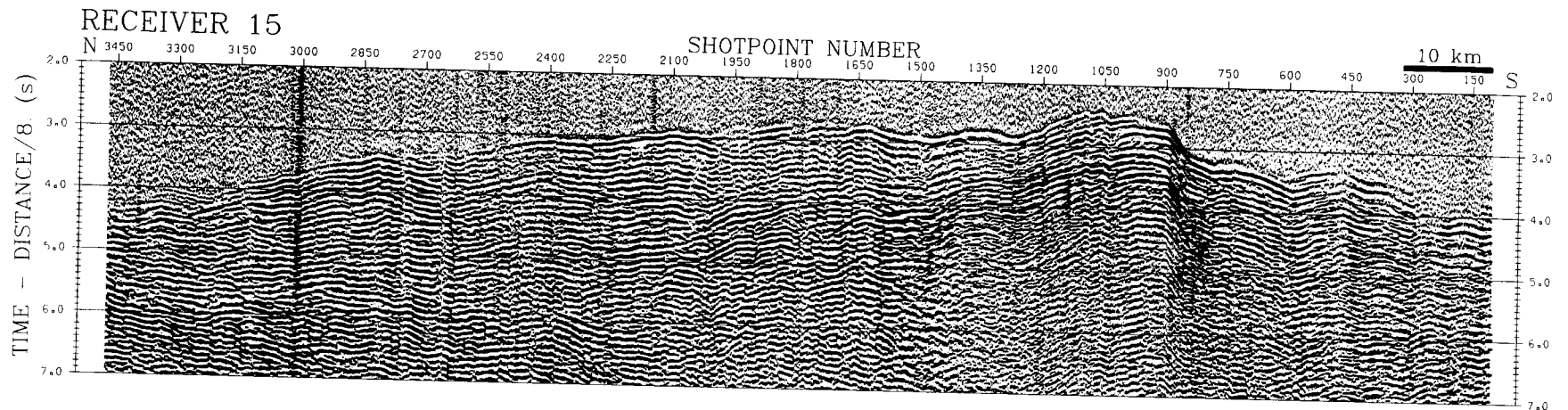
APPENDIX A

Table A.1 Line 4 geometry.

Receiver Number	Shotpoint 101 Offset (km)	Azimuth (degrees)	Shotpoint 3473 Offset (km)	Azimuth (degrees)
13	27	258	151	170
14	50	296	121	176
15	81	309	93	187
16	113	315	69	203
17	132	325	43	214
18	165	329	33	266
21	136	317	60	222

Figure A.1 (next three pages) Broadside refraction data sections for shot line 4 from the 1988 QC seismic survey. The data are plotted in the same manner as in Figure 1.4, which shows the sections for receivers 13 and 17. Shot-receiver offset and azimuth are given in Table A.1.





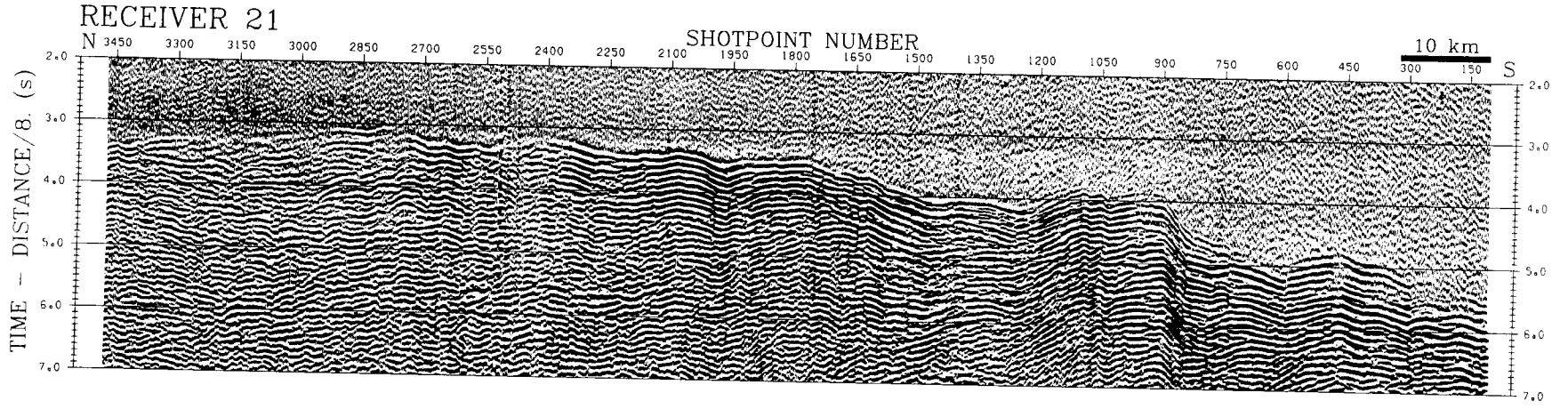
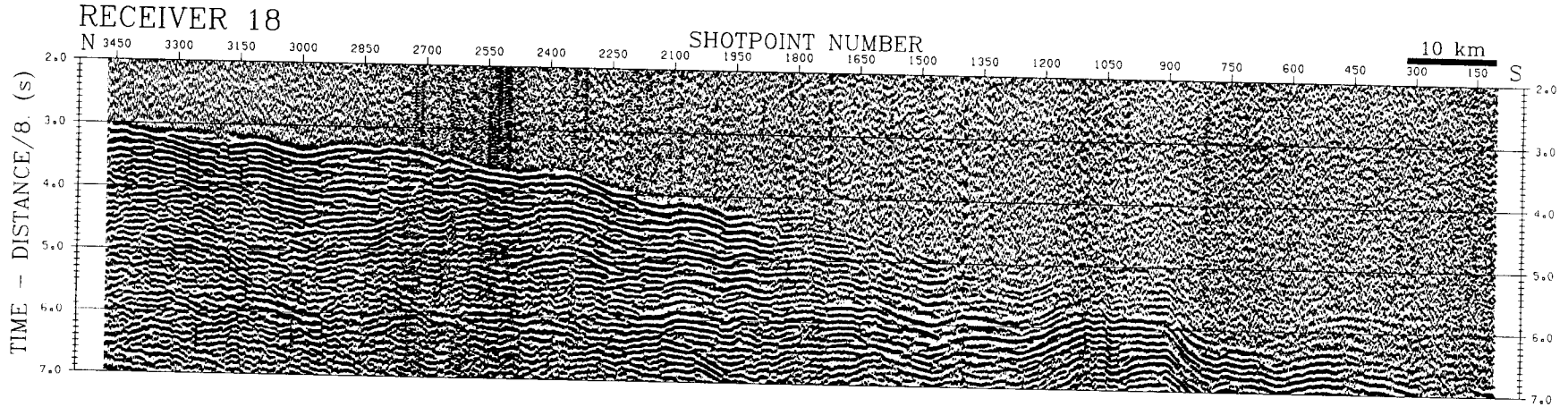


Table A.2 Line 1 geometry.

Receiver Number	Shotpoint 4284 Offset (km)	Azimuth (degrees)	Shotpoint 5304 Offset (km)	Azimuth (degrees)
13	38	255	39	181
14	57	288	22	238
15	87	303	41	294
16	117	311	71	311
17	134	320	89	325

Figure A.2 (next page) Broadside refraction data sections for shot line 1 from the 1988 QC seismic survey. Only those shots within the study area of Figure 1.2 are shown. The data are plotted in the same manner as in Figure 1.4. Shot-receiver offset and azimuth are given in Table A.2.

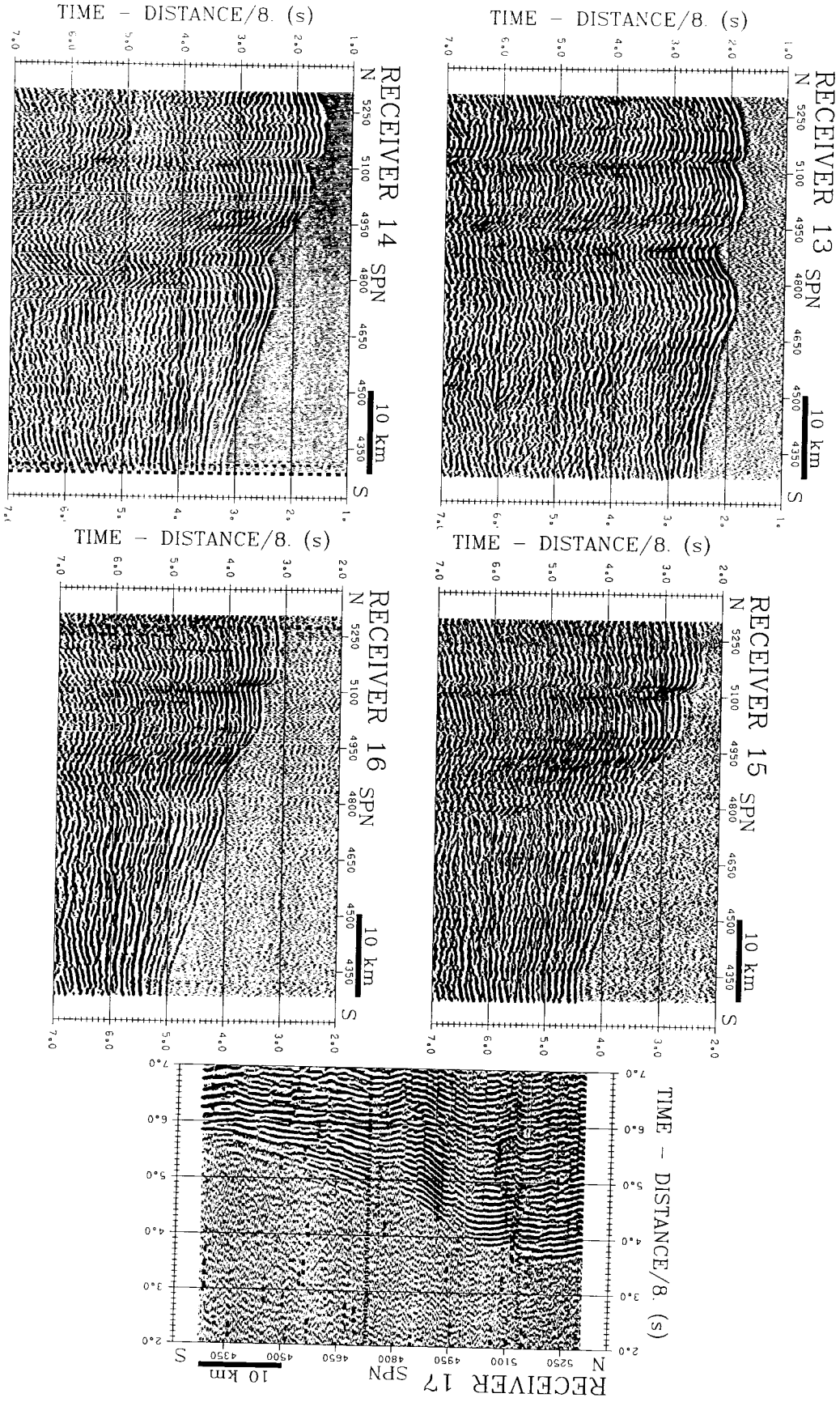


Table A.3 Line 5 geometry.

Receiver Number	Shotpoint 101 Offset (km)	Azimuth (degrees)	Shotpoint 656 Offset (km)	Azimuth (degrees)
13	68	172	86	186
15	30	248	54	238
18	93	328	91	312
21	68	303	78	285

Figure A.3 (next page) Broadside refraction data sections for shot line 5 from the 1988 QC seismic survey. Only those shots within the study area of Figure 1.2 are shown. The data are plotted in the same manner as in Figure 1.4. Shot-receiver offset and azimuth are given in Table A.3.

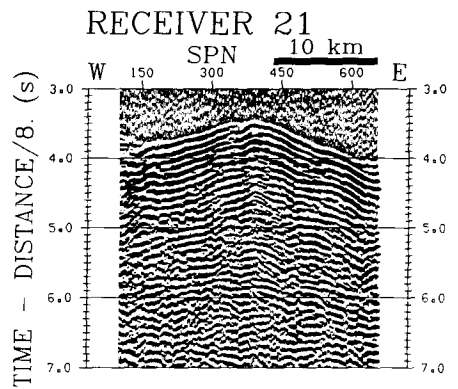
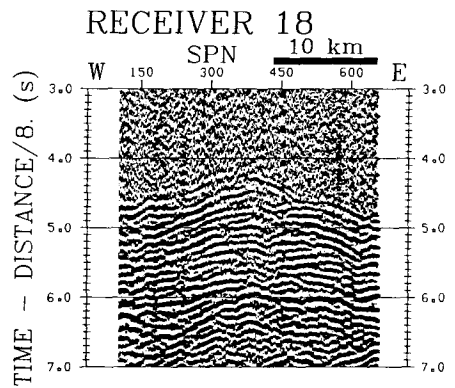
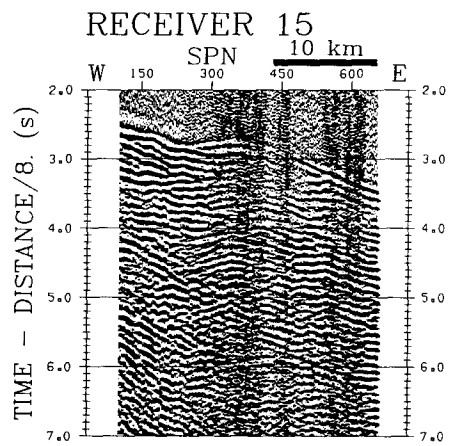
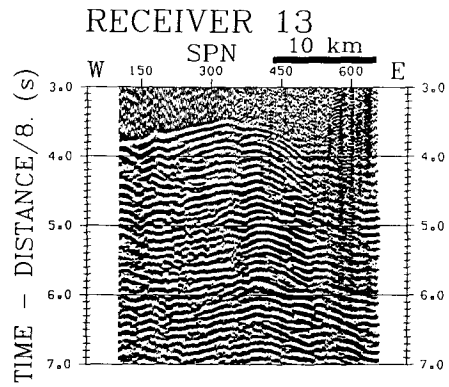


Table A.4 Line 6 geometry.

Receiver Number	Shotpoint 102 Offset (km)	Azimuth (degrees)	Shotpoint 727 Offset (km)	Azimuth (degrees)
13	127	165	141	175
15	66	183	88	197
17	20	240	48	234
18	35	312	48	277
21	38	242	66	237

Figure A.4 (next page) Broadside refraction data sections for shot line 6 from the 1988 QC seismic survey. Only those shots within the study area of Figure 1.2 are shown. The data are plotted in the same manner as in Figure 1.4. Shot-receiver offset and azimuth are given in Table A.4.

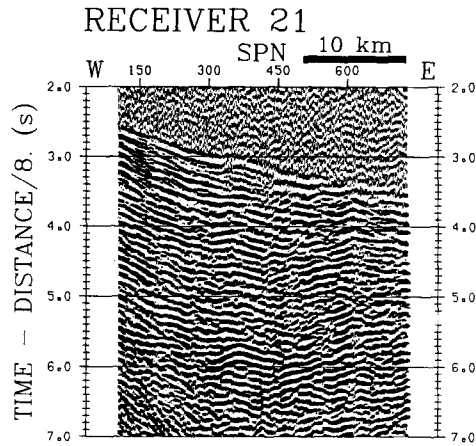
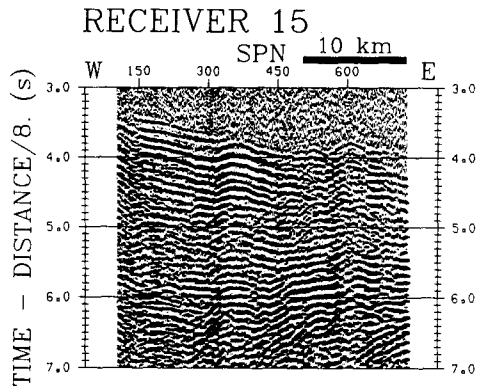
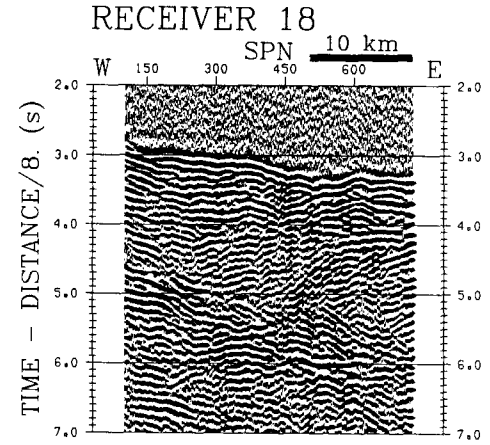
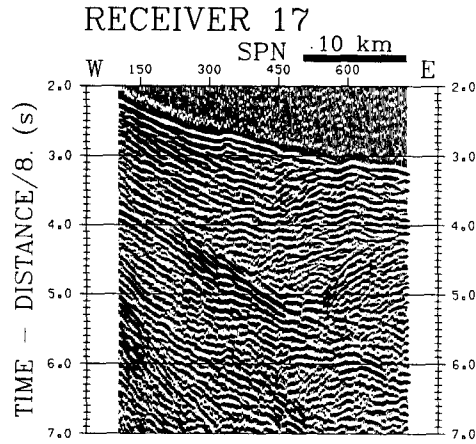
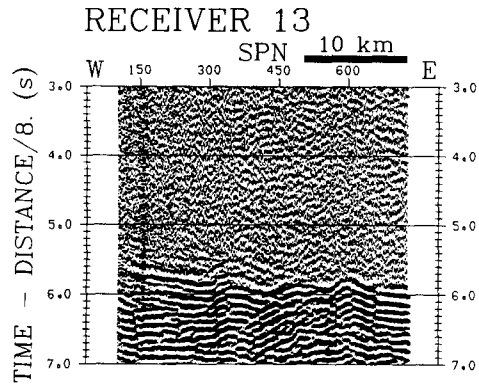


Table A.5 Line 7 geometry.

Receiver Number	Shotpoint 101 Offset (km)	Azimuth (degrees)	Shotpoint 890 Offset (km)	Azimuth (degrees)
15	69	192	104	190
16	49	219	81	205
17	30	249	56	215
18	44	302	43	253
21	49	247	73	222

Figure A.5 (next page) Broadside refraction data sections for shot line 7 from the 1988 QC seismic survey. Only those shots within the study area of Figure 1.2 are shown. The data are plotted in the same manner as in Figure 1.4. Shot-receiver offset and azimuth are given in Table A.5.

